Convection Administered Drug Delivery to the Brain

by

Grace Huynh

DISSERTATION

Submitted in partial satisfaction of the requirements for the degree of

DOCTOR OF PHILOSOPHY

in the

Joint Graduate Group in Bioengineering

in the

GRADUATE DIVISION

of the

UNIVERSITY OF CALIFORNIA, SAN FRANCISCO

AND

UNIVERSITY OF CALIFORNIA, BERKELEY

Acknowledgements (I)

The text of Chapter I is a reprint of the material as it appears in the *Journal of Controlled Release*. G.H. Huynh wrote the majority of the paper, with some sections written by F.C. Szoka. D.F. Deen assisted in the reading and revising of this paper.

Chapter II is a reprint of material as it appears in *Brain Research*. T. Ozawa assisted in the initial experiments involving implantation of the retro-convection enhanced delivery probe. D.F. Deen and F.C. Szoka assisted in the reading and revising of the paper. T. Tihan assisted in interpretation of the histopathology experiments.

The contribution of G.H. Huynh is comparable to that of a standard thesis.

Abstract

Brain tumor patients face a poor prognosis despite significant advances in tumor imaging, neurosurgery and radiation therapy. Potent chemotherapeutic drugs fail when used to treat brain tumors because biochemical and physiological barriers limit drug delivery into the brain.

A retro-convection enhanced delivery (R-CED) method has been developed to improve the entry of intravenously administered therapeutics within solid brain tumors. R-CED uses an osmotic gradient to withdraw brain interstitial fluid in a controlled manner via an implanted microdialysis catheter. The transmembrane osmotic gradient increased the local tissue specific gravity in normal brain and induced movement of small proteins and nanoparticulates from the blood into normal brain and an orthotopic 9L tumor. The magnitude of the R-CED effect decreased to control values within six hours and did not cause acute anatomical damage beyond that of probe insertion.

A one hour R-CED treatment applied immediately after intravenous injection of liposomal doxorubicin ten days after tumor implantation showed no therapeutic effect compared to animals treated with intravenous PBS alone. The result suggests that R-CED may be more efficacious by modifying the R-CED probe design, increasing the R-CED treatment time, and improving the chemotherapeutic type and dosing schedule.

A mathematical model has been developed to predict the size of the R-CED affected region while varying the interstitial and vascular hydraulic conductivity and the fluid removal rate. The model enables the prediction of non-spherical flow patterns during simultaneous R-CED and CED or dual-probe CED via two catheters, guiding probe placement to achieve drug patterning and enabling wide distribution of therapeutics

while sparing normal tissues. The alteration of solute flow was confirmed for dual-probe CED *in vitro,* but was difficult to visualize *in vivo,* where tissue inhomogeneities altered the flow from the idealized model prediction.

These studies demonstrate that R-CED is a viable and well-tolerated technique to enhance the distribution of systemically administered drugs in both the normal tissue-tumor margin as well as the central tumor core. They also highlight the opportunities to modify the R-CED design and enable future drug distribution and antitumor efficacy studies in larger tumors and possibly humans.

TABLE OF CONTENTS

PRELIMINARY PAGES:

List of Tables

List of Figures.

Chapter 1

CHAPTER I: Barriers to carrier mediated drug and gene delivery to brain tumors

I.1. Abstract and Introduction

I.1.1. Abstract

Brain tumor patients face a poor prognosis despite significant advances in tumor imaging, neurosurgery and radiation therapy. Potent chemotherapeutic drugs fail when used to treat brain tumors because biochemical and physiological barriers limit drug delivery into the brain. In the past decade a number of strategies have been introduced to increase drug delivery into the brain parenchyma. In particular, direct drug administration into the brain tumor has shown promising results in both animal models and clinical trials. This technique is well suited for the delivery of liposome and polymer drug carriers, which have the potential to provide a sustained level of drug and to reach cellular targets with improved specificity. We will discuss the current approaches that have been used to increase drug delivery into the brain parenchyma in the context of fluid and solute transport into, through and from the brain, with a focus on liposome and polymer drug carriers.

I.1.2. Introduction

An estimated 17,200 individuals in the United States are diagnosed with malignant CNS tumors per year [1]. Despite aggressive surgery, radiotherapy, and chemotherapy, the average one-year survival has increased little over the past three decades [1, 2]. This is related to the fact that brain tumors, upon diagnosis, are usually already 30 to 60 cm^3 in volume, approximately $3 - 6$ x 10^{10} cells. The tumor cell number

must be reduced to about 10^5 cells before the immune system can control it [3]. Though surgery and radiation therapy can reduce the tumor cell burden by 1000-fold, chemotherapy is not yet up to the task of a further two orders of magnitude reduction in tumor cell number [3]. Biochemical and delivery challenges slow the development of effective brain tumor drug therapies.

Current drug development to treat brain diseases is directed towards low molecular weight, lipid-soluble molecules that readily diffuse across the blood brain barrier (BBB) to reach diseased parenchymal tissue [4]. Although a number of low molecular weight molecules are helpful for the treatment of receptor or transporter-related diseases such as depression, low molecular weight drugs have had limited success for the treatment of Alzheimer's disease, Huntington's disorder, stroke or brain cancer. Macromolecular drugs may be particularly useful to treat these types of CNS diseases because they reach novel targets with a high specificity. However, the pursuit of macromolecular drugs to treat brain diseases is often abandoned because of difficulties delivering macromolecules to the parenchymal space of the brain.

A number of reviews have summarized the current challenges to brain drug delivery and technologies to improve the drug's access to the brain [5-9]. In this review, we will describe strategies to increase delivery into the brain parenchyma in the context of the barriers related to fluid and solute transport into, through and from the brain with a focus on liposome and polymer drug carriers.

I.2. Brain physiology and anatomy

The brain is an integral part of the central nervous system, acting as a major regulating and communicating organ to maintain the body's homeostasis in response to changes in both the external and internal environment. The primary cells of the brain include nerve cells (neurons) and supporting glial cells (glia); an adult human has approximately 100 billion neurons and 1 trillion glial cells [10]. The neurons and glial cells organize into specialized structures within the brain that can be characterized by both a unique architecture and function. Structures can be classified as either gray or white matter, areas of the brain dominated by cell bodies and axons respectively. Regions where the axons are aligned in the same direction are termed white matter tracts.

The three major subdivisions of the brain are the cerebrum, cerebellum, and the brain stem (Figure 1). The cerebrum is the largest section and is easily divided into the right and left hemispheres along the mid-sagittal plane. These hemispheres are made up of an outer layer of gray matter, the cerebral cortex, which is responsible for functions such as language and information processing. The cortex, made up of nearly 25 billion neurons, is highly convoluted, increasing the surface area to ~2300 cm^2. Cerebral cortex cells communicate with each other and with the spinal cord via the underlying cerebral white matter; communication between the two cerebral hemispheres primarily occurs via a major white matter tract called the corpus callosum. The cerebellum contains a similar gray and white matter organization but at a smaller scale, functioning primarily to control balance and coordinated movement. The brain stem, responsible for involuntary functions such as heart rate and breathing, connects the brain to the spinal cord. It

contains both gray and white matter regions but they are not organized into an inner and outer layer as in the cerebrum and cerebellum [10].
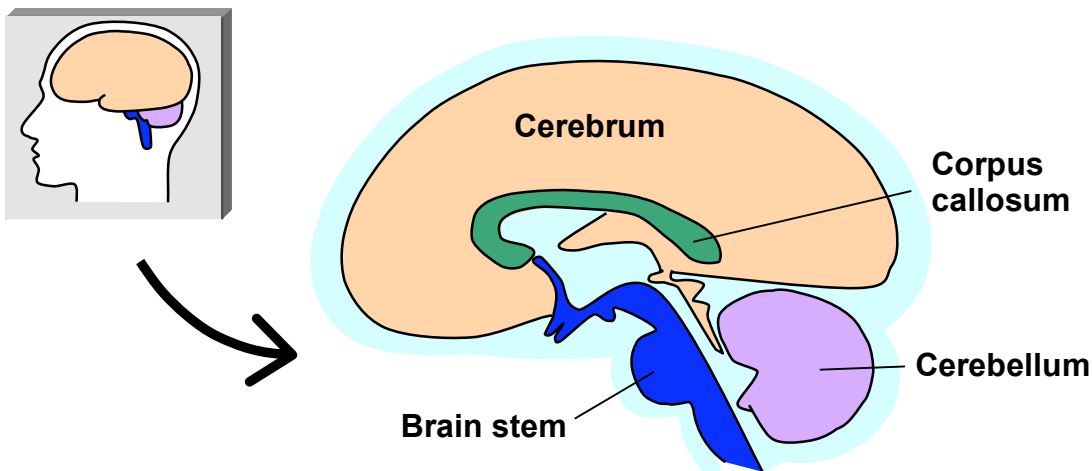
Figure 1. Brain section cut along the mid-sagittal plane, which divides the right and left sides of the brain. The major subdivisions of the brain are the cerebrum, cerebellum, and brain stem. The corpus callosum is the major white matter tract connecting the two hemispheres of the cerebrum.

The majority of brain tumors occur in the parenchymal space of the cerebrum [3]. However, more so than in any other tissue, getting drugs into the brain is much more difficult than getting drugs out of the brain. Brain tissue is protected externally by the skull, which constrains the volume and regulates intracranial tissue pressure [11]. Internally, the BBB greatly limits permeability and transport across the endothelial cell membranes of the blood vessels. Elimination of drugs from the brain is facilitated by mechanisms such as multidrug resistance transporters that actively extrude drug across the BBB [12] and a cerebrospinal fluid (CSF) turnover rate that is higher than the lymphatic drainage rate found in most peripheral tissues [13]. The production, flow, and drainage of the extracellular fluid (ECF) significantly affect the efficacy of brain drug delivery. To understand why the previous statement is true, we will describe the ECF flow pathway in further detail before addressing current brain drug delivery strategies.

I.2.1. Extracellular fluid (ECF)

In an adult human, the skull volume consists of blood (~170 mL), parenchyma (~880 mL), and ECF (~350 mL) [13]. The ECF in the brain is spatially segregated into the parenchymal interstitial fluid (ISF, ~225 ml) and the surrounding CSF (~125 ml). The volume of these compartments is tightly regulated such that the total volume remains constant ~1.4 L (Figure 2) [11]. In addition, the rate of flow through each of these compartments varies significantly; flow through the blood compartment, ~620 mL/min [14] is over three orders of magnitude higher than flow through the CSF compartment, ~0.35 mL/min [13]. For drug delivery purposes, it is necessary to consider the volume of these compartments, the flow through these compartments, and their function in normal brain.
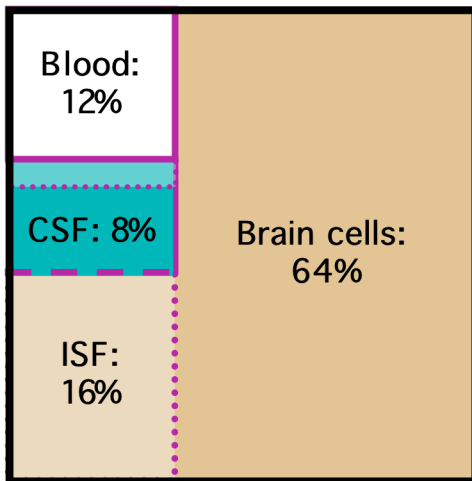
Figure 2. Brain volume is partitioned into four major compartments. The Monro-Kellie doctrine [11] dictates that changes in the volume of any one compartment requires corresponding changes in the other compartments such that the total volume remains constant. The skull (black line) confines the total volume of the parenchyma (tan), parenchymal ISF (lighter tan), blood (white), bulk CSF (blue), and ventricular CSF (light blue). All communication between the blood and other compartments is tightly regulated (solid purple line) while there is some communication between the CSF and ISF (dashed purple line). Compartments in direct contact with each other are separated by dotted purple lines.

The ECF cushions the brain during trauma, acts as a medium for cell to cell signal transmission, and is the carrier fluid for eliminating material from the parenchyma. As a result, production, composition, and clearance of the ECF are tightly regulated to maintain its composition and total volume.

ECF is spatially segregated into the parenchymal ISF and the surrounding CSF. Despite this spatial segregation, both fluids share a similar composition and maintain intimate chemical connectivity [15]. For example, tracers injected into one fluid can access both the subarachnoid space of the CSF and the parenchymal perivascular areas of the ISF. However, there is incomplete bulk mixing within the ECF compartment, as evidenced by tracers injected in the left cerebral ISF, which preferentially accumulate in the lymph nodes on the left side compared to the right side [16].

The composition of the ECF is not in equilibrium with the plasma; the concentration of Mg^{2+} and Cl^- are increased and the concentration of K^+, Ca^{2+} and amino acids are decreased (Figure 3). This is in contrast to the ECF found in peripheral tissues, which contains a similar ion concentration as plasma [13].

Solute concentrations in ECF relative to plasma
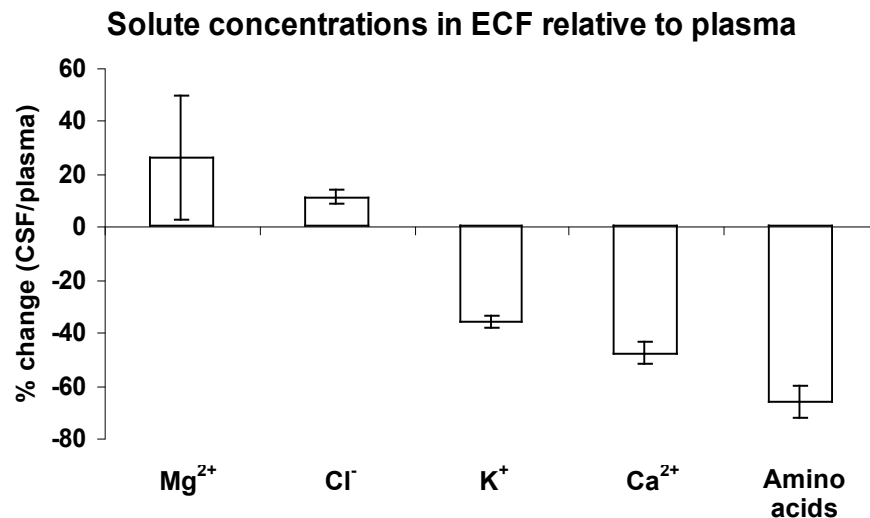
Figure 3. Solute concentrations in the CSF are significantly different compared to the plasma. Concentrations of Mg^{2+} and Cl^- are higher while levels of K^+, and Ca^{2+} and amino acids are reduced. Values are averaged for the CSF and plasma in human, dog and cat, which share similar CSF solute concentrations [13].

I.2.2. Cerebrospinal fluid (CSF)

Adult humans have approximately 110-150 ml of CSF; approximately 20% of the CSF is found in the ventricles within the brain and the remaining 80% of the CSF is found between the meninges, connective tissue layers that surround the brain. Of the three meningeal layers, the pia lies closest to the brain and adheres to the surface of the parenchyma; the overlying arachnoid and dura follow the contour of the skull (Figure 4). CSF within the meninges is primarily contained between the delicate pia and arachnoid, a region called the subarachnoid space. This space widens into sac-like cisterns at locations where there are grooves on the surface of the brain, housing the majority of the CSF [18].

Figure 4. The brain is enclosed within several layers. From innermost to outermost, these layers are the three meningeal layers (pia, arachnoid, and dura), the skull, muscle, and the skin. Of these layers, only the pia closely follows the contours of the brain surface [17].
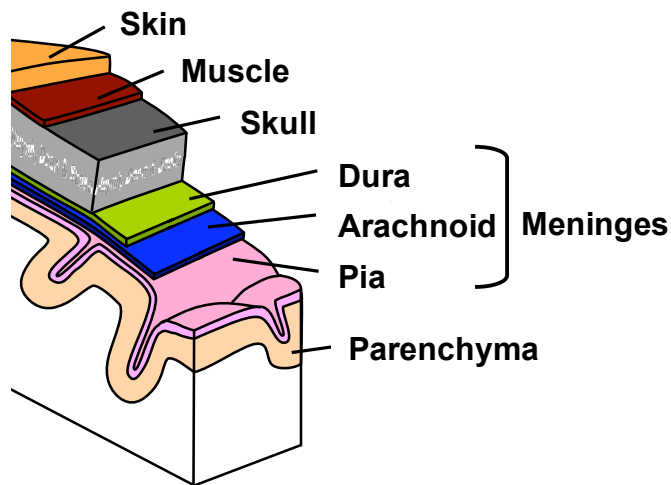
The source of the CSF is the blood that flows through the brain. It is secreted by the epithelial cells which line the lateral, 3rd and 4th ventricles. This epithelial layer, known as the choroid plexus, is organized into villi, which increases the surface area to approximately 200 cm^2. Each villus consists of a centrally located ~15 μm diameter

capillary surrounded by a single layer of cuboidal epithelial cells linked together by apical tight junctions (Figure 5A, 6) [19].
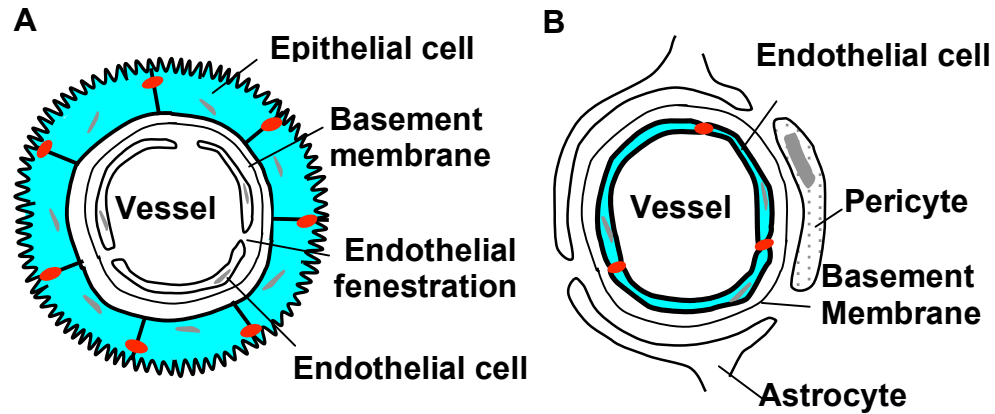
Figure 5. ECF is secreted at the choroid plexus epithelium (A) and the blood brain barrier (B). The secreting cells (blue) are joined by tight junctions (red). A. Villi (cross section shown) consist of a central capillary surrounded by epithelial cells, which are joined by apical tight junctions and secrete the CSF into the ventricles. B. Endothelial cells, joined by tight junctions, secrete ISF which flows across the basement membrane and between pericytes and astrocytes into the parenchyma.

The first step of CSF secretion is filtration of the plasma across endothelial fenestrations having diameters ranging from 60-350 nm [13]. The plasma filtrate cannot flow freely past the choroidal epithelial cells because these cells are joined by tight junctions; rather, the choroidal epithelial cells actively secrete the CSF. A hypertonic solution is generated by apical Na/K/ATPase, Na/K/2Cl co-transporter, HCO_3 and K channels.

This hypertonic solution is diluted by water flux through co-localized aquaporin-1 (AQP1) channels on the apical membrane of the choroidal epithelial cells. AQP1 channels have a very high single-unit water permeability of ~6 x 10^{-14} cm^3 /sec, sufficiently fast to ensure that channel permeability is not the limiting factor in the water secretion required to make the CSF isotonic with plasma [20, 21].
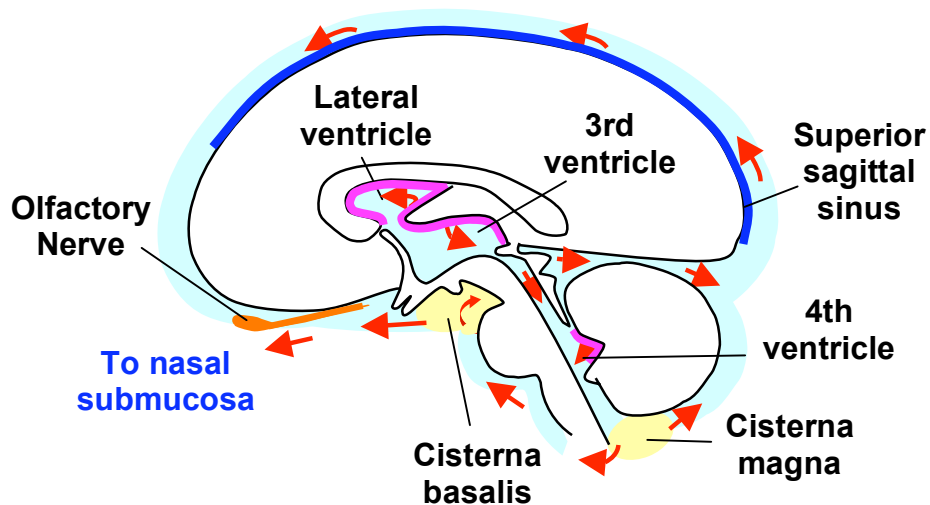
Figure 6. Cerebrospinal fluid (CSF) flow pattern in the brain. CSF is produced at the choroid plexus (pink); flow around the brain (red) is directed at two primary cisterns (yellow) and drains primarily through the superior sagittal sinus and through the nasal pathway (blue).

After the CSF is produced in the ventricles, it flows through the subarachnoid space; the flow direction is dictated by the parenchymal structures and by two major cisterns, the cisterna magna and the cisterna basalis (Figure 6). CSF produced in the lateral, third, and fourth ventricles flows down to the cisterna magna, which directs flow back and upwards around the cerebellum or forward around the brain stem to the cisterna basalis. From the cisterna basalis, CSF can flow forward and drain primarily through the anterior portion of the superior sagittal sinus. Alternatively, it can flow back between the cerebrum and cerebellum to join the fluid at the back of the brain that is moving upwards around the cerebellum from the cisterna magna. This fluid continues flowing upwards and forwards around the brain, primarily draining by the superior sagittal sinus. Fluid in the sinus ultimately drains to the venous system.

Sinuses are formed by separations in the thick and rigid dura. Drainage of CSF from the subarachnoid space into the sinus is controlled by valve-like protrusions of the subarachnoid space called arachnoid granulations (Figure 7). This flow is driven by both

a hydrostatic and colloid osmotic pressure gradient [13], which opens pores in the

granulation to allow passage of large proteins such as albumin.
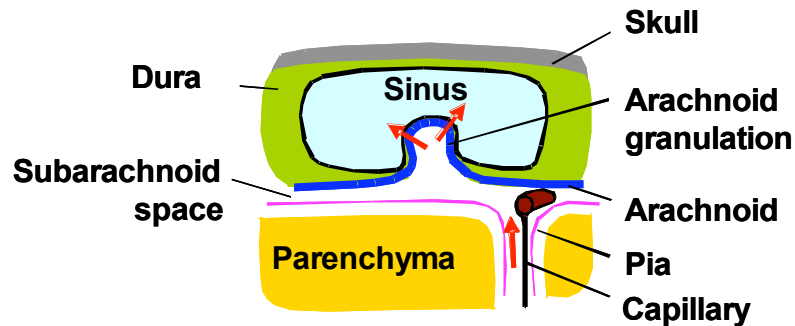
Figure 7. The sinuses are major pathways for ECF drainage from the brain. ISF drains (red arrows) from the parenchyma along perivascular pathways into the bulk CSF within the subarachnoid space before crossing arachnoid granulations to drain into the sinus. Sinuses are formed by separations in the dura and ultimately allow fluid to flow into the venous system.

Manipulation of the pressure gradient directly affects the flow across the

arachnoid granulation; increased CSF pressure or a lowered sinus pressure increases the

flow across the granulation into the sinus. However, flow backwards from the sinus into

the CSF is not allowed because the valves of the arachnoid granulation open in one way

only. It is thought that the granulations collapse when the pressure gradient is reversed

[22].

A controversial pathway of fluid drainage through the nasal mucosa may account

for up to 50% of the CSF drainage [23, 24]. This pathway stems from the cisterna basalis

and allows CSF flow along the olfactory nerves to the nasal submucosa (Figure 6), an

area rich in both blood vessels and afferent lymph pathways. The blood vessels in this

region are dense and fenestrated [25], allowing diffusion of tracer molecules such as

EDTA and inulin from the CSF to the blood. Additionally, a significant amount of water

passes into the blood, as evidenced by higher postnodal lymph protein concentrations compared to prenodal lymph protein concentrations [26].

The fenestrations of the nasal submucosa blood vessels are not large enough to allow passage of particulates or higher molecular weight proteins, so these CSF tracer molecules drain by traditional lymphatic pathways into the lymph nodes of the neck. Because this CSF drainage pathway does not involve the arachnoid granulations, it is thought to be more important in children, who have less fully developed arachnoid granulations. The role of this pathway in adult CSF drainage remains unclear [22, 27].

I.2.3. Interstitial fluid (ISF)

In the extracellular parenchymal space of an adult human, there is approximately 200-250 ml of ISF, accounting for approximately 15% of the parenchymal brain volume [15]. The source of ISF is the blood flowing through the capillaries. ISF is secreted at the capillary wall, which has a surface area of ~20 m^2 in an adult human [4]. Though the surface area of ISF secretion is approximately 1000 times greater than the surface area for CSF secretion, the rate of ISF secretion is approximately 1/10 of the CSF secretion rate, as measured in rats [16]. This lower ISF secretion rate corresponds to a lower ISF turnover rate, averaging approximately 10 hrs compared to the 2.5 hr turnover of the CSF [13].

Like CSF secretion, the ISF is not produced as a plasma filtrate at the BBB. The capillary endothelium in the parenchyma (Figure 5B) is surrounded by a basement membrane, which in turn is encircled by an interdigitating perivascular sheath of astrocytic glial cells. Of these structures that form the BBB, the capillary endothelium is

the primary regulator and generator of flow to the interstitial space. This modulatory function is partially maintained by signaling from the surrounding astrocytic glial sheath [22]. The tight junctions between the endothelial cells reduce the permeability across the capillary wall to a level where transport across the barrier can be described by models of transport across a cell membrane. Moreover, the hydraulic conductivity of the BBB is 2-3 orders of magnitude lower than that found for peripheral tissue capillaries and almost no pinocytosis occurs across the endothelium [28, 29].

The low hydraulic conductivity of the BBB is partially explained by the minimal expression of aquaporin water channels present in the endothelial cells; there is no AQP1 expression and only minimal levels of AQP4 are present. The low hydraulic conductivity across the BBB is exhibited macroscopically in measurements of the electrical resistance across the membrane, which averages 2-3 orders of magnitude greater than in peripheral capillaries [13].

Once ISF is produced, there is limited mixing of the ISF within the parenchymal compartment; bulk flow of the ISF is confined to the white matter and the perivascular space [30]. In the white matter, ISF can flow more freely; large tracers such as India ink (mean diameter ~250 nm) preferentially flow in the same direction as the fiber tracts [31].

Within the gray matter, bulk flow is primarily observed in the perivascular space, not directly through the parenchymal tissue. This distinction occurs because the perivascular space offers a much lower resistance to flow. Flow resistance is primarily defined by the width of the pathway; the perivascular space has an average width of 500 nm while the width of the extracellular clefts between adjacent parenchymal cells

averages only ~10-20 nm. In addition to the lower resistance to flow in the perivascular space, blood vessel pulsations have been shown to contribute to the movement of ISF through the parenchymal tissue [32].

Because bulk flow does not occur directly through the parenchymal tissue, clearance of the ISF occurs primarily by bulk flow along the perivascular space to the CSF in the subarachnoid space. This pathway is ideal for ISF drainage because the perivascular space extends along the entire cerebral vasculature (Figure 7). A limited level of ISF drainage occurs along the optic pathways and other cranial nerves, as traced by the movement of small molecule tracers. However, this is not a quantitatively important CSF drainage pathway [22, 33].

The rate of ISF clearance is comparable to the average rate of lymph flow for the whole body, estimated at 0.03 μl/g tissue/min [16, 31]. In addition to ISF drainage pathways, clearance of particulates from the extracellular space is also mediated by phagocytosing cells such as microglial cells that migrate throughout the entire nerve tissue and by macrophages that surround the larger arteries and veins; India ink particles [34] and liposomes [35] are removed by phagocytosis into perivascular and parenchymal macrophages [34].

I.2.4. Physiological & biochemical changes caused by brain tumors

The growth of brain tumors induces a number of changes in the fluid flow patterns of the brain. For example, the rapid growth of the tumor is often too fast for the development of appropriate fluid flow pathways into and away from the tumor space. The failure to properly develop these pathways may result in accumulation of fluid in the

tumor extracellular space. Because the brain is confined to the skull, the accumulation of fluid increases the interstitial pressure within the tumor space and in surrounding normal regions of the brain. Tumors that have grown to larger volumes may compress pain-sensitive intracranial structures such as blood vessels, sinuses, and cranial nerves, leading to headache. Further, cerebral blood flow may be reduced, which may lead to local regions of hypoxia and neuronal cell death [36]. Displacement of the neurons from their normal position relative to each other can also affect their ability to properly signal to each other, resulting in neurological symptoms such as seizures, sensory deficits, motor weakness, and changes in cognitive ability [37].

Accumulation of fluid in the tumor space is partly driven by increased fluid entry from the blood across the BBB [38]. Metastasizing tumors have both enlarged fenestrations and interendothelial gaps that can range in size from 5 nm to as large as 1 μm. The basement membrane in tumor vessels is also generally thinner than in normal cerebral blood vessels, further reducing the barriers to flow from the capillary lumen to the interstitial space [39, 40].

In addition to these physical changes, the endothelial cells within the tumor express high levels of the AQP1 and AQP4 water channels, which facilitate the movement of water from the blood into the parenchyma. Since normal brain endothelial cells have near zero expression of aquaporins, the high expression of aquaporins in tumor-associated endothelial cells is likely an effect of the up-regulation of growth factors within the tumor space. Further, the tumor cells have been found to have a 3-5 fold increased expression of AQP4, allowing for increased flow from the extracellular space into the cells [41]. Fluid flow into the cells decreases the clearance of ECF from

the brain and also contributes to a high intratumoral pressure [21, 42]. In addition, the presence of drug efflux transporters in the brain tumor endothelial cells, even at low levels, significantly impacts the distribution of drug within the tumor [12, 43].

The combination of reduced blood flow to tumors, drug efflux transporters and increased interstitial pressure all contribute to the reduced uptake of systemically administered drugs into the tumor.

I.3. Small Animal Models of Brain Tumors

The development of appropriate small animal models of brain tumors is integral to the development of chemotherapy studies. It is necessary to consider what animal and tumor type to use, how and where the tumor will be induced, and the appropriate dosing schedule to evaluate the treatment protocol [44].

Brain tumor models can be spontaneous or artificially implanted into the animal. Spontaneous models can be induced by repeated exposure to carcinogens or to sarcoma viruses. However, these models suffer from non-uniform growth rates and poor tumor take. As a result, this technique is not optimal for chemotherapy studies. However, this technique has been used successfully to isolate a number of brain tumor cell lines, such as the 9L gliosarcoma and the F98 glioma [44]. Tumor cell lines have also been isolated from human brain tumors at the time of surgical resection [45].

Implantation of tumor cell lines can be done orthotopically into the brain or subcutaneously in sites such as the flank. It has long been known that the environment imparts a strong influence on the growth of tumor cells and that orthotopically implanted tumors respond to treatment protocols differently than subcutaneous tumors. Recent gene

15

expression profiling of human brain tumor lines (U251, U87) grown in culture, in subcutaneous or in intracerebral (i.c.) sites in immunocompromised rats reinforces this point; expression profiles of the two lines were significantly different in culture but became similar in the i.c. site [45]. In the i.c. site the two lines expressed more genes that are associated with CNS expressed gene products.

The majority of experimental chemotherapy studies that use i.c. brain tumor models in small animals have been done in rats. The rat has a brain that is large enough for the reproducible implantation of tumors and a body size that makes it economically feasible to have a statistically significant treatment group [44]. In the case of a rapidly growing tumor such as the 9L Fischer rat derived line, systemic chemotherapy within five days after implantation leads to an increase in the survival time. However, waiting even a few days longer to treat the tumor dramatically decreases the response rate [58].

In addition to the day of treatment, the choice of an appropriate tumor model has significant implications for accurate evaluation of a treatment protocol. For example, boron neutron capture therapy is highly effective against the 9L rat tumor, yet has only a modest effect against the F98 rat tumor; the F98 line is highly resistant to radiation and other types of chemotherapy [46].

Even when using a tumor model that is responsive to the treatment protocol, it can be difficult to assess whether the observed effect is a direct result of the administered treatment. Many rat brain tumor models are immunogenic even in a syngeneic host [44]. The immunogenic response can be reduced by using immunocompromised animals, which are able to tolerate both rat brain tumor allografts and human brain tumor xenografts. Immunologic responses can also occur as a result of tissue injury. A number

of therapies that are administered via catheter directly into the tumor cause trauma and local inflammation, which alters the capillary permeability and the immunologic milieu of the tumor site. This may be a particular concern with the assessment of gene therapies in rodent models. Aspects of model selection and administration route have been discussed by Fross and coworkers [47].

Murine brain tumor models are used much less frequently in chemotherapy studies because of the small size of the animal; tumor implantation in the brain requires higher precision and the animal size makes dosing by routes other than the intravenous or intraperitoneal route exceptionally difficult. In spite of these issues, murine models have been used frequently for gene delivery studies. The introduction of transgenic models that mimic the ontology of human brain tumor development has provided a promising tool for studies related to the development and progression of brain tumors [48].

I.4. Drug delivery to the brain

Current strategies to deliver drugs to brain tumors include methods that exploit the following routes of administration: intravenous, intra-arterial, intraventricular, intrathecal, and intraparenchymal. These methods introduce drug in different spatial locations in the ISF/CSF fluid flow pathway; hence, they distribute the drug in different regions of the brain based on the volume of the compartment and the rate of the fluid production and drainage (Figure 8). The route of administration can profoundly influence the drug concentration in the tumor, the normal brain and systemic organs, dramatically modulating drug effectiveness and toxicity.
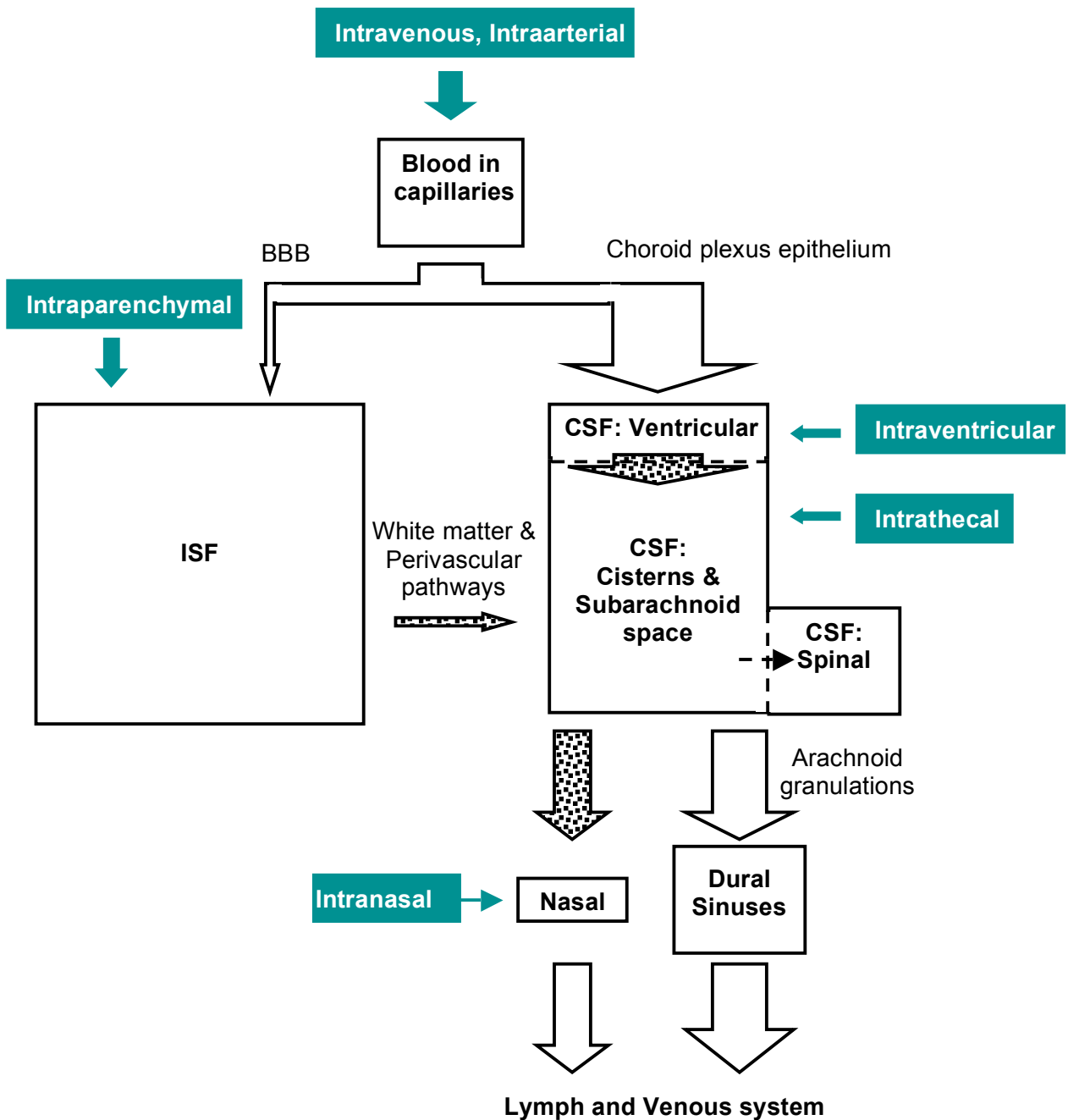
Figure 8. Different delivery methods introduce drug in different spatial locations in the ECF flow pathway. This results in drug localization in different regions of the brain based on the volume of the compartment and the rate of the fluid production and drainage. In this figure, the area of the various compartments correlates with their relative stationary volumes in human brains. Dotted arrows indicate flow pathways where diffusion may occur in the opposite direction. The width of dotted and unfilled arrows correlates with the relative flow rates. The width of the filled arrows leading from the routes of delivery correlates with the relative amounts that can be delivered using that route.

The efficiency of drug delivery to the parenchyma is significantly affected by the properties of the drug. Factors such as the half life of the drug in the plasma and CSF, the level of nonspecific binding to plasma proteins, the permeability of the compound across the BBB and into peripheral tissues, and the rate of metabolism or binding of the compound within the brain combine to influence drug concentration in the brain parenchyma.

Systemic delivery by the intravenous route is the most commonly used and allows for administration of the largest doses of drug into the body. However, drug exposure to peripheral organs is high and there is little accumulation of the drug in the brain because of the BBB and rapid clearance of material from the ECF. For example, temozolomide, following intravenous infusion into a monkey, is present in the brain at substantially lower levels compared to the plasma. Despite this drawback, the drug has shown a therapeutic effect in clinical trials and was recently approved by the FDA [49, 50].

To increase the dose in the brain and reduce the drug exposure to peripheral tissues, intraventricular or intrathecal administration can be used to provide the drug direct access to the CSF compartment. Though this technique is effective for the treatment of periventricular and meningeal tumors, the drug has limited penetration into the parenchymal space and is much less effective to get drug into parenchymal tumors. To increase drug accumulation in the parenchymal space, direct intraparenchymal administration may be required.

We will briefly describe both systemic and regional strategies to deliver drugs to the brain with a focus on delivery to brain tumors. Treatment for other types of CNS diseases often establishes different requirements for the drug delivery system; for

example, treatment immediately after a stroke must be quick and address both focal and diffuse damage, while treatment for a degenerative disease may focus on a particular region and require a prolonged treatment schedule [51].

I.4.1. Systemic delivery

To improve systemic drug delivery by direct injection into the blood, a number of strategies have been developed to increase the blood brain barrier permeability of small molecule drugs across the BBB. These methods, which have been extensively reviewed elsewhere [5, 8], include chemical modification of the drug, intra-arterial administration, and BBB disruption. For example, the BBB permeability of some chemotherapeutic drugs can be increased by chemical conjugation to groups that enhance binding to the BBB endothelium or increase the molecule's lipophilicity. However, these changes often alter the plasma kinetics and may reduce the molecule's toxicity to tumor cells. Intra-arterial administration avoids the need to alter the drug and allows the drug to access the brain vasculature before that of peripheral tissues, reducing the effects of first-pass metabolism in the liver. Intra-arterial administration of chemotherapeutics is often used in conjunction with BBB disruption mediators such as the bradykinin receptor agonist Cereport^{TM} [52] or hyperosmotic mannitol [53]. Because these molecules increase the BBB permeability throughout the entire brain, careful patient monitoring is required to reduce the risk of treatment related seizures and elevated intracranial pressure [54]. These strategies to improve systemic drug delivery have achieved some success in patients for the delivery of small molecule drugs. However, repeated administration is

often required due to the short plasma half life of most small molecules. To increase the elimination half life, the drug can be formulated into a polymer or lipid based carrier.

I.4.1.1. Particulate drug carriers

Particulate drug carriers range in size from less than 100 nm to approximately 300 nm. These carriers accumulate in the tumor due to the leaky vasculature and poorly developed lymphatic system in the tumor, a result better known as the enhanced penetration and retention effect [55]. Systemic administration of lipid based drug carriers are currently being investigated in a number of pre-clinical animal models and clinical trials in patients (Table 1 and 2). Current systems are primarily nontargeted but could be targeted using antibodies against receptors such as the transferrin receptor [82-84], low molecular weight peptides or carbohydrates [85]. Liposomes can also be used as a carrier for use in combination therapies such as with photodynamic [63-65] or thermosensitive systems [56, 60].

Table 1: Delivery of low molecular weight compounds to rat intracranial brain tumors using liposomes and lipid systems

Tumor	Treatment	Day of treatment	Delivery	General Conclusions	Study
virus induced glioma	Cisplatin, thermosensitive	10	IV	survival increased from 19 to 41.6 days	[56]
sarcoma	Doxorubicin	6 or 11	IV	survival increased 168%	[57]
sarcoma	Doxorubicin	6, 13, 20	IV	survival increased 189%	[57]
9L	Doxorubicin	7, 14, 21	IV	survival increased from 24.5 to 31.5 days	[58]
9L	Doxorubicin	11,18,25	IV	no significant effect	[58]
9L	Doxorubicin	7 14, 21	IV	intratumor hemmorage in 63-75% of rats	[59]
C6	Doxorubicin, thermosensitive		IV		[60]
C6, 9L	Fluorophore, microbubbles	15	IV	accumulation of fluorophore in tumor	[61]
9L	Paclitaxel, microbubbles	6-11, 14-19	IV	no significant effect	[62]
9L	Paclitaxel, microbubbles	6-11, 14-19, 22-27	IV	survival increased from 20 to 27 days	[62]
U87	Photofrin	14	IV	increased photodynamic tissue destruction	[63]
9L	Photofrin + enhancer	14	IV	increased tumor necrosis	[64]
9L	Photofrin	16	IV	increased photodynamic tissue destruction	[65]
melanoma metastasis	Empty, multilamellar	21	IA, IV	no accumulation in tumor	[66]
9L	cisplatin	tumor size 100 mg	IA	increased cisplatin accumulation in tumor	[67]
ENU induced tumor	cisplatin, ferritin		IA		[68]
L1210 mouse tumor	cytosine arabinoside	1	IC	100% cured	[69]
C6	7-beta-hydroxycholesteryl-3-oleate	0 or 3	IC	80% failed to develop tumor	[70]
	borocaptate		IC	enhanced BSH retention in cells	[71]
U87	Fluorophore + mannitol	tumor size 100 mg	CED	Mannitol, smaller size increases tissue penetration	[72]
C6, 9L-2	Gadolinium, fluorophore	10 or 16	CED	Development of MRI to monitor tumor growth	[73]

CED: Convection enhanced delivery
ENU: N-ethyl-N-nitrosourea
IA: Intraarterial
IC: Intracranial,
IV: Intravenous

Table 2. Clinical trials of liposomes carrying low molecular weight drugs for brain tumors

Tumor	Patients	Treatment	Delivery	Day of treatment	General Conclusions	Study
recurrent tumor	14	Daunorubicin	IV	once every 4 weeks	6/14 patients showed positive response	[74]
GBM	8	Daunorubicin	IV	24 hr before surgery	concentration similar in tumor mass and peripheral regions	[75]
Pediatric glioma	7	daunorubicin + free carboplatin & etoposide	IV	daunorubicin: day 1 & 2 carboplatin & etoposide: day 1	5/7 showed positive response with monthly treatment	[76]
GBM	15	doxorubicin + radiation	IV	Doxorubicin: 1, 21 Radiation: 1-12, 21-23	4/10 patients completely responded	[77]
Solid tumor	22	Doxorubicin	IV	once every 4 weeks	Phase I: dose limiting toxicity: 70 mg/m2	[78]
Glioma	40	doxorubicin + free tamoxifen	IV	PEG-dox: day 4 every 14 days Tamoxifen: day 1 every 4 days	Phase II: response (including stabilization) 40%	[79]
Glioma	8	111In labeled	IV	contrast only	tumor uptake: 1.1% max tumor:brain contrast 7:5	[80]
Glioma	3	Bleomycin	IT	twice weekly for up to 6 weeks	all patients deteriorated, no toxicity	[81]

GBM: glioblastoma
IT: intratumor
PEG: poly(ethylene glycol)

Drugs that have been formulated into liposomes or lipid carriers for brain tumor therapy include: 7-beta-hydroxycholesteryl-3-oleate [70], boro-captate [71], cis-platinum [56, 67, 68], cytosine arabinoside [69], doxorubicin [57-60, 77, 79], paclitaxel [62], and photofrin (Table 1) [63-65]. Formulating the drug into a liposome significantly increases drug accumulation within the brain and enhances animal survival. For example, in intracranial brain tumors of rats, liposomal doxorubicin significantly improved survival from 23.5 to 31.5 days compared to free doxorubicin, which had nearly no effect compared to animals receiving saline injections [58].

Further studies using this model suggest that doxorubicin triggers a cascade effect where the first dose of doxorubicin may increase the permeability of the vasculature, enabling greater access of the drug to the tumor. This is thought to be mediated by doxorubicin-induced killing of proliferating endothelial cells and a subsequent reduction in the levels of angiogenic growth factors such as VEGF [59]. As such, the cascade effect of doxorubicin would have the greatest effect for drugs formulated into carriers that have a long circulation time in the plasma. Although the preclinical studies using liposome-encapsulated drugs given via the intravenous or intra-arterial route have resulted in an increased survival time, in no instance were there long term survivors.

There have been fewer studies reported using polymer based particles to deliver drugs to the brain after intravenous administration (Table 3). Polymer particles in the range of 200 - 300 nm that are given systemically are primarily formulated by adsorbing the drug onto the particle surface [113, 116, 118]; these particles are phagocytosed into the cell where the drug is then released [113]. For example, solid poly (butyl cyanoacrylate) nanoparticles loaded with doxorubicin have been shown to increase the drug concentration in normal rat brain 60 fold higher than that achievable by free doxorubicin [119]. When these particles are used in the 101/8 rat glioblastoma model, over 20% of the animals achieved long term remission over 125 days with no indications of short term neurotoxicity [115]. This encouraging report must be contrasted with another study that formulated doxorubicin in PEGylated hexacyanoacrylate particles [114]. Although the maximum tolerated dose of doxorubicin that can be administered is higher when the drug is formulated into particles compared to the free drug, no improvement in antitumor efficacy was seen in this study using the 9L tumor model.

Table 3. Delivery of low molecular weight compounds to brain tumors using polymer depots and polymer particulates

Polymer	Treatment	Loading	Tumor	Day of treatment	General Conclusions	Study
wafers						
stearic acid: SA 1:1	BCNU, 70kD dextran	10%	no tumor		majority of drug within 1-2 mm of implant	[86]
CPP:SA	BCNU	0 - 32%	9L	7	surivival increased from 24 to 50 days	[87]
CPP:SA	BCNU, carboplatin or camptothecin + radiation	10-20% BCNU, 0.5-1% carboplatin, 10% camptothecin	EMT-6 mouse breast carcinoma	polymer: 5 radiation: 7-9	survival increased from 17 to >200 days for 20% BCNU survival increased to 41 days for 10% BCNU + radiation no advantage for carboplatin or captothecin polymer	[88]
CPP:SA	BCNU + ip O6-BG	3.85%	F98	5	survival increased from 23.5 days to 34 days	[89]
CPP:SA	camptothecin	20-50%	9L	5	50% camptothecin: survival increased to 69 days	[90]
polylactic acid	cisplatin	0.5 mg/m2	9L	7	survival increased from 24 to 51 days	[91]
stearic acid: SA 1:1	4-HC	0-50%	9L, F98	3 or 5	Survival increased from 14 days to 77 days for 20% taxol	[92]
EVAc	dexamethasone	7.5 mg	9L	5	improved control over peritumor edema	[93]
PLGA	etanidazole	1%	tumor cavity	resection	simulation only	[94]
PLGA, 10% PEG	etanidazole	1%	tumor cavity	resection	simulation only	[95]
CPP:SA	IUdR + radiation	10-50%	U251 in mice	5	survival increased to 80 days	[96]
stearic acid: SA 1:1	MTX & MTX-dextran	10%	9L	5	survival increased from 18.6 to 29.6 days	[97]
CPP:SA 1:1	minocycline + systemic BCNU	50%	9L	0 or 5	day 0: 100% long term survivors day 5: survival increased from 14 to 20 days	[98]
EVAc	Mitoxantrone	33%	9L	2	survival increased from 13.8 days to 33 days	[99]
EVAc	NGF	35%	no tumor		majority of drug within 2-3 mm of implant	[100]
CPP:SA	Paclitaxel	20-40%		5	20% taxol: survival increased from 19.5 to 61. 5 days	[101]
EVAc	Suramin	33%	9L	2	no survival advantage	[102]
collagen, injectable	vinblastine sulfate	0.2-2% mg / kg	KHT, mouse	5	60-75% long term survivors	[103]
implanted polymer particulates						
polyomido amino dendrimer + targeting	Boron compounds + iv BPA	960 B / dendrimer	F98	14	survival increased from 33 to 57 days	[104]
CPP:SA pellets	BrdU, PALA, radiation	15% BrdU, 5% PALA	C6	12	83% long term survivors	[105]
PLGA microspheres	carboplatin, BCNU	10% carboplatin, 15% BCNU	RG-2	10	survival increased from 20 to 36 days after debulking	[106]
PLGA microspheres	carboplatin	10% carboplatin	cortical	10	1/3 long-term survivors after debulking	[107]
PLGA: 45 um	5FU	22%	C6	12	survival increased from 19 to 30 days	[108]
PLGA: 35 um	5FU	13%	C6			[109]
silicone pellets	GCV + HSV-tk	20%	9L	5	75% long term survivors	[110]
silicone pellets	GCV + HSV-tk	20-30%	9L	5	75% long term survivors	[111]
PMMA pellets	MTX	1.4 mg / pellet		day 10	survival increased from 23 to 44 days	[112]
PLGA pellets	NGF	50%	no tumor		drug released in 1st week within 2-3 mm of implant	[100]
intravenous polymer particulates						
PBCA: 230 nm	dalargin peptide	1.35% adsorbed	no tumor	no tumor	analgesia over 90 min	[113]
PEG-hexadecylcyano acrylate 100-200 nm	doxorubicin	5-10%	9L	3	no improvement on efficacy	[114]
PBCA: 270 nm	doxorubicin	0.25%	101/8	2, 5, 8	20% long term survivors	[115]
PBCA: 290 nm	loperamide	1.80%	no tumor	no tumor	analgesia increased from 5 to 210 min	[116]
cetyl alcohol /polysorbate: <100nm	Paclitaxel	0.05-0.15%	brain perfusion	no tumor	2x more paclitaxel in brain compartment	[117]
PBCA: 230 nm	tubocurarine	0.12%	brain perfusion	no tumor	generated seizure patterns in EEG measurements	[118]

4-HC: 4-hydroperoxycyclophosphamide   * in rat unless otherwise noted
5-FU: 5-fluorouracil
BRDU: bromodeoxyuridine
CPP:SA: 20:80 bis(p-carboxyphenoxy)propane:sebacic acid
EVAc: 3:2 Elvax40P:vinyl acetate
GCV: ganciclovir
IUdR: iododeoxyuridine
MTX: methotrexate
NGF: nerve growth factor
O6-BG: O6-benzylguanine
PLGA: poly(lactide-co-glycolide)
PMMA: poly(methyl methacrylate)
PALA: N-(phosphonacetyl)-L-aspartic acid

I.4.1.2. Clinical trials in brain tumor patients of intravenously administered drug carriers

Based on these pre-clinical animal studies, systemic delivery of drug carriers based on lipids or polymers shows significant promise to increase the concentration of drug within the brain and improve treatment efficacy of small molecule drugs. The availability of two commercial anticancer liposome formulations DaunoXome™ (liposomal daunorubicin) and Doxil™ (liposomal doxorubicin) have enabled a number of human clinical trials (Table 2). Tumors resected 24 hours after dosing daunorubicin liposomes had a therapeutic drug concentration in the central tumor mass [75]. The response rate in these trials was in the 40% range, which was considered promising by the authors [74, 77, 79]. However patients in three of these trials received concurrent radiation or other chemotherapeutic agents, complicating analysis of the treatment efficacy. Additional trials are required to more clearly identify the advantage of intravenous liposome drug delivery in brain tumors.

I.4.2. Delivery into the CNS

It is possible to achieve much higher concentrations of drug in the brain by direct injection into the CSF or parenchymal space, substantially reducing the systemic drug concentrations. The distribution of the injected drug within the parenchyma and the CSF is defined by factors such as the site of puncture, rate of bulk CSF production, movement and clearance, and diffusion or transport of the drug across the CSF-brain boundary [125].

I.4.2.1. Intra-CSF

Drugs can be directly injected into the CSF intrathecally or intraventricularly. Though intrathecal administration into the cisterna magna is substantially less invasive than intraventricular administration, intrathecal delivery methods fail to result in drug accumulation in parenchymal structures deep within the brain [126]. Often, there is significant spreading of the drug along the spinal canal, as observed in the intrathecal injection of the anticancer drug etoposide into the cisterna magna of dogs [127]. Along the spinal cord, sites as far away as 20 cm had etoposide concentrations greater than the maximum etoposide concentration measured in the parenchymal space. The significant spinal exposure to the drug led to ataxia, a loss of muscle coordination, in the dogs. At doses that did not cause ataxia, the CSF concentration of etoposide was more than 100-fold below therapeutic levels achievable by high dose intravenous therapy. Thus, intrathecal anticancer drug delivery is more appropriate for treatment of disseminated meningeal and spinal disease, but not for treatment of large parenchymal tumors such as glioblastoma [128].

Intraventricular administration of CNS drugs results in higher and more reliable distribution of the drug in the ventricles and subarachnoid space but also has limited parenchymal penetration [126]. As a result, intraventricular delivery is particularly useful for meningioma treatment and to prevent tumor metastasis by cells floating in the CSF, but not for treating gliomas. Bolus intraventricular drug administration is limited because most small molecules have a short half-life in the CSF. As a result, repetitive dosing or continuous infusion is necessary in order to maintain cytotoxic concentrations within the CSF.

Sustained intraventricular delivery can be achieved using a pump, a refillable reservoir, and a catheter permanently implanted into the lateral ventricle [129]. The pump and reservoir are usually implanted on the surface of the skull near the skull hole used for catheter implantation. Intraventricular bolus or chronic infusion systems have been developed and are currently in clinical use, including the original Ommaya reservoir [129]and newer versions such as the Infusaid pump [130], the MiniMed PIMS system [131], and the Medtronic SynchroMed system [132].

These products have been used for the therapy of brain tumors in a number of patients. For example, an Ommaya reservoir has been used for delivery of etoposide in patients who suffered from metastatic brain tumors. Though peak etoposide concentrations in the CSF were more than 100-fold greater than that achieved by intravenous infusion, the treatment failed to inhibit metastasis into the parenchyma [133]. This is likely a result of insufficient drug penetration into this compartment.

Intraventricular administration of sustained release systems improves the pharmacokinetic profile of the drug in the CSF and improves therapeutic outcomes. For example, DepoCyt^{TM} consists of a suspension of multivesicular lipid particles that are 3 – 30 μm, which biodegrade to release encapsulated cytosine arabinoside. These particles have been injected intraventricularly or intrathecally. Preclinical studies in primates showed that compared to intrathecal delivery of unencapsulated cytosine arabinoside, use of DepoCyt^{TM} increased the CSF half-life from 0.74 hours to 156 hours. Clinical trials of intrathecal DepoCyt^{TM} for patients with neoplastic meningitis resulted in a complete response in 71% of patients compared to 15% of patients treated with intrathecal cytosine arabinoside [134].

I.4.2.2. Intraparenchymal

Intraparenchymal drug delivery involves the placement of a needle directly into the target parenchymal space for bolus injection or continuous infusion into the interstitial space (Figure 9A) [135, 136]. This technique has been used to deliver both particulate drug carriers and small molecule therapeutics such as BCNU and carboplatin. These treatments are generally well tolerated and show a therapeutic effect in both animal models and in clinical trials.

A

B
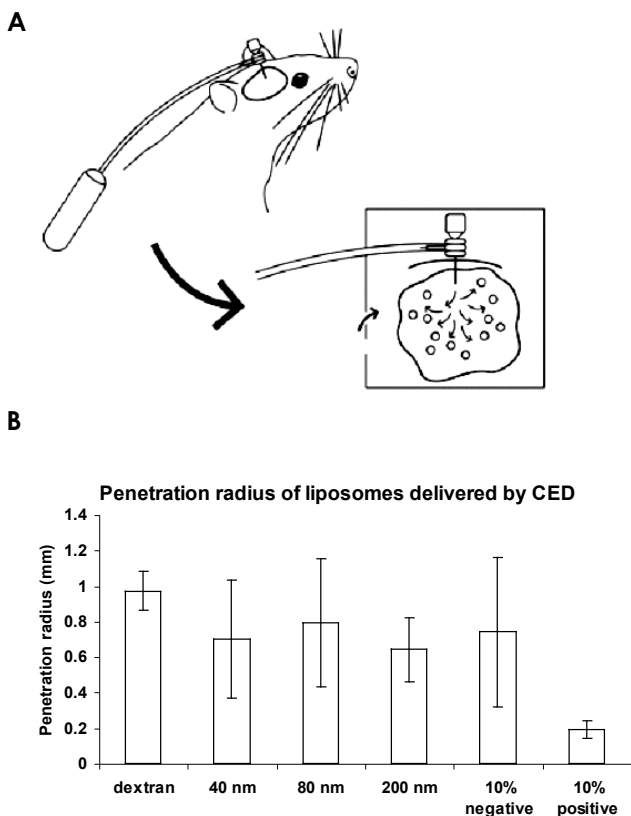
Figure 9.   Intraparenchymal drug delivery by convection enhanced delivery. A. A subcutaneous pump is implanted between the scapulae and a needle is cemented onto the skull to provide a constant infusion into the parenchymal space. B. Penetration radius of a small molecular weight dextran, and liposomes having various surface charge and diameter delivered using CED.   Labels indicate the following: 'dextran' is a 10 kD dextran (n=4), '40 nm' diameter liposomes (n=3), '80 nm' diameter liposomes (n=26), '200 nm' diameter liposomes (n=3), '10% negative' charged 80 nm liposomes (n=4) and '10% positive' charged 80 nm liposomes (n=4). Error bars indicate the standard deviation. [135].

When bolus injection is used, the resulting drug distribution throughout the tissue is primarily a result of concentration-dependent diffusion. Thus, in order to achieve and maintain therapeutic drug levels in a large tissue region, it may become necessary to use

high concentrations of the drug, which can quickly lead to dose-limiting neuro-toxicity. For this reason, direct injection is more efficacious for the delivery of small molecule therapeutics compared to particulate drug carriers.

An alternative to direct injection is convection enhanced delivery (CED); a continuous infusion uses a convective (vs. diffusive) flow to drive the therapeutic throughout a larger region of tissue. Animal experiments comparing bolus injection to a 1-week continuous infusion using CED have shown that CED is better able to deliver large doses and maintain drug distribution and concentration over time [137]. For example, intraparenchymal delivery of cytosine arabinoside achieved maximum drug concentrations 10 times greater than intraventricular delivery, 100 times greater than intrathecal delivery, and 1000–10,000 times greater than intravenous delivery. CED also maintained this maximum concentration over 2 mm from the injection site, while the maximum concentration of arabinoside delivered intraventricularly and intrathecally fell at a distance 1 mm and 0.5 mm away from the site of injection, respectively [126].

Other materials that have been delivered by CED include paclitaxel [138], immunotoxins [139], DNA in lipoplexes [140, 141], viruses [142], boronated compounds for neutron capture therapy [143], and liposomes [135, 144]. Many of these materials have been tested in clinical trials [145]. Liposomes of various surface charge and diameter were delivered into the rat brain using CED. However, their distribution is significantly reduced compared to that of small molecules such as a 10 kD dextran. Neutral liposomes of 40 nm and 80 nm in diameter distributed to a similar extent, which was slightly greater than the distance obtained by 200 nm liposomes. Negatively charged liposomes also shared a similar distribution but positively charged liposomes were

retained close to the infusion site (Figure 9B). [135]. This observation of retention of cationic particles has been widely reported in various gene therapy studies using synthetic gene vectors that are combined with DNA; lipid or polymer based systems, termed lipoplexes and polyplexes respectively, often achieve transfection only in the vicinity of the needle tract (described in section I.4.3).

The ability of CED to deliver agents to a large tumor volume has been exploited in a number of clinical trials. For example, clinical trials involving CED of immunotoxin into glioblastoma tumors were able to achieve complete regression with minimal systemic toxicity for some patients [139].

To further increase the distribution of the drug from the needle tip, solvent-facilitated perfusion can be used. In this method, the drug is dissolved in 100% ethanol, which distributes rapidly from the infusion site and may inhibit loss of the drug into the blood by reducing blood flow. In human brain tumors, BCNU in 100% ethanol distributed up to 2.4 cm from the site of injection [146]. Further studies in mouse tumors showed that this treatment correlates with a significant increase in the formation of DNA adducts, which are initiators in a cascade ending in cell death [147]. This was manifested as a reduction in tumor growth that was significantly lower compared to systemic administration of the same dose of BCNU [147]. Solvent-facilitated perfusion may be particularly promising to treat large tumors; however, this drug delivery method is still under development and large scale clinical trials beyond Phase I/II have not been completed.

I.4.2.3. Particulate drug carriers

Drug carriers such as liposomes and polymer nanoparticles have been administered directly into the tumor site. In contrast to systemic administration, direct injection into the brain increases the concentration and half-life of drug in the brain compartment and can protect the drug from degradation and binding to efflux proteins at the BBB. The low diffusion coefficient of these particulates significantly hampers their ability to diffuse a significant distance from the administration site. Thus, intraparenchymal delivery of particulate drug carriers has primarily used CED to distribute the drug through a larger region in the tissue.

In addition to the convective force to drive the particles through tissue, there are a number of other contributing factors that determine particle distribution within the tumor. Penetration through the tissue can be increased by a negative or neutral particle charge and by limiting particle size to less than 80 nm. In addition, including mannitol or a large excess of label/drug free liposomes in the perfusate can further increase the penetration distance [135, 144]. Attachment of targeting ligands can also be used to control which cells take up the particles and to increase the particle penetration distance [144]. These strategies raise the exciting prospect that liposomes containing drugs can be distributed to a large brain volume and provide a sustained local release of chemotherapeutic agent for a prolonged period. It has been suggested that optimal gene [148] or drug delivery [149] to brain tumors can be achieved using the simultaneous application of magnetic resonance imaging techniques to guide the optimal placement of the infusion catheter and the distribution of the drug carrier.

I.4.2.4. Polymer depot

There is a large literature involving the intratumoral administration of polymer depots (Table 3 and 4). Many combinations of polymer matrix and anti-neoplastic drugs have been tested in animal models and in clinical trials. The polymer literature has been covered by a number of recent reviews [154, 155]. Intratumoral implantation of large polymer depots allows for sustained slow release of drug as the polymer biodegrades [156, 157]. Drug release rate is primarily controlled by the type of polymer matrix being used and on the drug properties and loading concentration.

Table 4. Human clinical trials of polymer depots and polymer particulates

Polymer	Treatment	Loading	Tumor	General Conclusions	Study
CPP:SA	BCNU + radiation	3.85%	32 patients - glioma	survival increased from 39.9 to 58.1 weeks	[149]
CPP:SA	BCNU	3.85%	62 patients - GBM	survival increased insignificantly from 50 to 58 weeks	[150]
CPP:SA	BCNU + radiation	3.85%	240 patients - glioma	survival increased to 13.9 months from 11.6 months	[151]
6-carboxylcellulose	Cisplatin + radiation	1 mg /cm2	38 patients - GBM	survival increased from 211 to 427.5 days	[152]
polylactic acid	ACNU pellets	0.6 mg / pellet	11 patients - GBM	local necrosis observed 12 days after implantation	[153]

* all polymers implanted at resection

ACNU: 1-(4-amino-2-methyl-5-pyrimidinyl) methyl-3-(2-chloroethyl)-3-nitrosourea

The polymer depot that has been approved for brain tumor therapy is the Gliadel™ wafer [158], which contains 3.85% BCNU. The implant is inserted into the tumor resection cavity, releasing BCNU over a period of 5 days as the polymer degrades; complete polymer degradation occurs in approximately 6 weeks [159]. BCNU concentration in the brain is separated into 2 regions: a high dose region containing millimolar concentrations of BCNU within 3 mm of the polymer implant and a low dose region in the micromolar range at 1 day post-implantation. One week post-implantation, BCNU concentrations were in the micromolar range at a distance 1-2 cm from the implant [159]. This large parenchymal penetration was attributed to the lipophilic properties of BCNU, leading to permeation of the drug into the CSF and bloodstream before re-entry back the brain.

Phase III clinical trials of Gliadel[TM] in 240 newly diagnosed malignant glioma patients showed that the median survival increased from 11.6 months to 13.9 months [151]. For patients with recurrent glioblastoma, Gliadel[TM] treatment increased median survival from 4.6 months to 6.4 months. Of all patients enrolled in the trial, long term survivors at three years included 11 patients in the Gliadel group and 2 in the control group [154]. These studies confirmed that the use of drug-impregnated wafers for local chemotherapy can improve survival for patients with newly diagnosed malignant glioma.

Efforts to improve local wafer-mediated BCNU delivery include increasing the BCNU concentration and combining BCNU with other drugs. Recent dose-escalation studies in monkeys [160] and humans [161] have shown that concentrations up to 20% BCNU are well-tolerated with little systemic side effects. The distribution of BCNU from the implant remained in the low micromolar range up to 2 cm away from the implant. Based on these results, Phase III trials are currently being planned [154].

The toxicity of BCNU also can be increased by concurrent administration of molecules that enhance cell sensitivity to nitrosoureas. For example, the cell's ability to repair BCNU-induced DNA damage can be inhibited by systemic administration of O^6-benzylguanine. In animal models, administration of O^6-benzylguanine significantly increased survival from 25 to 34 days compared to animals receiving BCNU polymer implant alone [89]. However, Phase I/II trials of systemic O^6-benzylguanine plus BCNU have shown that administration of O^6-benzylguanine substantially lowers the maximum tolerated dose of BCNU, with unclear benefit of the combination therapy compared to BCNU alone [162, 163].

Local delivery using biodegradable wafers can also be used to deliver combinations of chemotherapy drugs [164] and as part of a treatment protocol with radiotherapy [165]. However, polymer implants containing drugs less lipophilic than BCNU, such as paclitaxel, showed substantially reduced parenchymal penetration to < 2 mm at 1 week post-implantation [160]. This limited penetration of drug from the wafer makes it unlikely that the placement of a monolithic depot in the brain will solve the drug delivery challenges to brain tumors including diffusion barriers, active transport from endothelial cells, and significant elimination of drug from the parenchyma by ISF flow.

I.4.3. Gene therapy

The brain is also a target for a variety of gene therapy approaches involving viral, lipid and polymer based, and cell based delivery strategies. Viral vectors are considered the most effective and have been used in a number of animal models and the majority of brain tumor gene therapy clinical trials. The use of viruses for brain tumor gene therapy has been reviewed extensively elsewhere [166]. Despite encouraging pre-clinical results, clinical studies have not shown similar success; few trials have shown substantial extended patient survival. This is thought to be caused by a failure to distribute the viral vector throughout the tumor mass and a wide variability in the infectivity of brain tumor cells, resulting in an insufficient number of transfected tumor cells [166].

Cellular methods, particularly those using neural stem cells, have the potential to enhance the efficacy of gene therapy because the stem cells are less immunogenic and can preferentially migrate to the tumor. This technique is relatively newer and has only been tested in a limited number of animal models. Studies that have been completed in

mice have shown significant promise and encourage further studies to investigate neural stem cells as an alternative to viral vectors [167].

Lipid and polymer based gene therapy strategies have been more extensively studied and have been tested in small clinical trials. These delivery systems are comparatively simple, easy to formulate and are generally less immunogenic and less neurotoxic than viral systems. However, lipid and polymer systems tend to achieve lower *in vivo* transfection efficiencies, shorter transgene expression times, and face similar distribution challenges as viral systems. Nonetheless, well designed synthetic lipid vectors can be nearly as efficacious as viral vectors [168]. We will briefly describe current progress using lipid and polymer based systems for gene therapy in the brain.

Lipoplexes or liposomes have been used more frequently to treat brain tumors (Table 5), while polyplexes usually have been applied to normal brain for the delivery of reporter genes or growth factors (Table 6). The majority of these reports have administered the vector directly into the brain or into the tumor in the brain. Expression of reporter genes has been observed for as long as two to three months post administration using either lipoplexes or polyplexes.

Table 5. Gene delivery by lipoplexes or lipid systems

Vehicle	Gene	Cationic lipid	Target region	Delivery	Day of treatment	General Conclusions	Study
Animal studies							
targeted liposome	AS EGFR mRNA	DDAB	U87 in mice	IV	5, weekly	survival increased from 18 days to 36 days	[84]
targeted liposome	RNAi: anti-luciferase	DDAB	C6 expressing luciferase	IV	10	luc expression inhibited by 90% for >5days	[169]
lipoplex	non-coding	DOTIM	4C8 mouse GBM	IV	3, 10 OR 17, weekly	significant decrease in tumor volume	[170]
targeted liposome	RNAi: EGFR	DDAB	U87 in mice	IV	5, weekly	88% increase in survival	[171]
lipoplex	CCK-8	lipofectin	P77PMC rat	IVC	congenitally epileptic rat	transfection & seizure repression for 14 days	[172]
lipoplex	NGF	DC-Chol	normal rat	IVC	injury: day 1	reduced neuron loss after brain injury	[173]
lipoplex	CAT	DOTIM	normal rat	IVC, IC	normal	transfection for up to 4 weeks	[174]
liposome	GFP	MLRI	normal brain	IVC	normal	extensive GFP expression throughout CNS	[175]
lipoplex	bcl-2	DOTAP	normal rat	IVC	normal	infarct reduction after MCA occlusion	[176]
multilamellar liposome	IFN beta	TMAG	U-251-SP in mice	IT			[177]
liposome + plasmid	IFN beta	TMAG	T9	IT	0	survival increased from 22 to 29.8 days	[178]
liposome + plasmid	luciferase	DOTMA	F98	IT	7	transfected 3 cell layers around injection tract	[141]
targeted liposome	IFN beta	TMAG	U-251-SP in mice	IT	7, 9, 11, 13, 15, 17 14, 16, 18, 20, 22, 24	day 7: all long term survivors day 14: reduced tumor size	[179]
multilamellar liposome	IFN beta	TMAG	U-251-SP in mice	IT	7, 9, 11, 13, 15	all long term survivors	[180]
lipoplex	IFN beta	TMAG	GL261, mouse	IT	4	survival increased from 32 days to 67 days	[181]
liposome	HSV-tk	DC-Chol, DOCSPER, DMRIE	F98	IT	HSV-tk: 7; ip GCV: 3-17	10/80 animals complete tumor regression	[168]
lipid-virus complex + ip GCV	HSV-tk	TMAG	GL261, mouse	IT	HSV-tk: day 4, 8, 12, GCV: 5, 6, 9, 10, 13, 14	significant decrease in tumor volume	[182]
lipoplex	beta-gal + NLS	lipofectin	normal mice	IC	normal	transfection for 9 days	[183]
lipoplex	beta-gal	lipofectin	mouse caudate	IC	normal	transfection for up to 21 days	[184]
Tf-lipoplex	NGF	DC-Chol	striatum	IC	injury: day 0 or 1	8/1 (+/-) maximizes gene transfer	[185]
lipoplex	beta-gal	DOGS	rat caudate	CED	normal	increased transfection for longer infusion	[186]
lipoplex + ip GCV	HSV-tk	DAC-Chol	F98	CED	HSV-tk: 7; ip GCV: 3-17	36% long term survivors	[140]
Clinical Trials							
lipoplex	ASPA	DC-Chol	2 patients: Canavan disease	IVC	1	biochemical, radiological & clinical changes	[187]
liposome + plasmid	IFN-beta	TMAG	5 patients: GBM & AA	IT	0, 14, 21, & 28	Phase I: 2 patients had partial response, 2 patients stabilized	[188]
liposome + plasmid	HSV-tk	DC-Chol	5 patients: GBM	CED	HSV-1-tk: day 1; GCV: day 4-14	development of PET to follow transfection	[189]
liposome + plasmid + iv GCV	HSV-tk	DC-Chol DC-Chol	Phase I/II 8 patients: GBM	CED	HSV-1-tk: day 1; GCV: day 4-14	2/8 showed >50% reduction in tumor volume	[148]

AA: anaplastic astrocytoma
AS: antisense
ASPA: aspartoacylase
CAT: chloramphenicol acetyltransferase
CCK-8 peptide: cholecystokinin octapeptide
DAC-Chol: DAC-30 (3 â (N-N, N'-dimethyl-aminoethane-carbamoxyl-cholesterol
DDAB: didodecyldimethyl ammoinium bromide
DOGS: lipopolyamine of dioctadecylamidoglycylspermine
DORI: (N-(1-(2,3-dioleoyloxy)propyl)-N-(1-2-hydroxy)ethyl)-N,N dimethyl ammoinium iodide
DOTAP: 1,2-dioleoyl-3-trimethylammonium-propane
DOTIM: octadecenoyloxy(ethyl-2-heptadecenyl-3-hydroxyethyl)imidazolinium chloride
DOTMA: N-[1-(2,3,-dioleyloxy)propyl]-N,N,N-trimethyl-ammonium chloride
EGFR: epidermal growth factor receptor
GFP: green fluorescent protein
IFN: interferon
IVC: intraventricular
MCA: middle cerebral artery
MLRI: disymmetric myristoyl & lauroyl substituted compound formed from tetraalkylammonium glycerol based prototypic cationic lipid DORI
NGF: nerve growth factor
NLS: nuclear localization signal
TMAG: N-(alpha-trimethylamminioacetyl)-didodecyl) glutamate chloride

Table 6. Gene delivery by polyplexes

Vehicle	Gene	Target region	Delivery	General Conclusions	Study
PEI	luciferase	brain stem	IM	transfection from 18h to 2wks after injection	[190]
PEI	beta-gal	periventricular neurons and glia	IVC	transfection in periventricular cells	[191]
PEI	luciferase	brain of xenopus tadpole	IVC	linear PEI more efficient than branched	[192]
PEGylated PEI	luciferase	spinal parenchyma & meninges	IVC	PEG-PEI 11x more efficient transfection than PEI alone	[193]
PPP, PEI	luciferase	mouse brain stem	IVC	transfection primarily in brain stem	[194]
targeted PEI	luciferase	dorsal root ganglia	IVC	targeting increased transfection 9-14x	[195]
polyamino polymer	luciferase	D54-MG (7-12 days) in mouse	IC	gene expression levels comparable to AAV vector	[196]
PEI	luciferase	newborn mouse striatum	IC	optimal PEI cation/anion balance is slightly cationic	[197]
PEI	luciferase & bcl-2	cortex, hippocampus in mice	IC	transfection observed up to 3 months later	[198]
PEI	dopamine transporter	substantia nigra	IC	transfection observed from day 3-14 after injection	[199]
PEI	Targeted luciferase	newborm hypothalamus	IC	transfection of cells near 3rd ventricle	[200]
PEI	fluorescein-DNA	hippocampus	IC	transfection in neurons and glia cells	[201]
targeted poly-lysine	GFP	substantia nigra	IC	transfection observed from 48hr to 15 days after injection	[202]
targeted poly-lysine + fusogenic peptide	GFP	substantia nigra	IC	transfection lasted up to 60 days	[203]
PEI	NGF	septum	IC	attenuated neuronal loss from 70% to 28% at day 7 after injury	[204]

IM: intramuscular
PPP: polyaminoethylpropylene phosphate

A variety of cationic lipids have been employed to prepare the lipoplexes; however, no particular lipid appears to convey a substantial gene transfer advantage. In those instances where tumors were treated, almost all of the reports described significant increases in survival time (Table 5) [84, 140, 148, 170, 171, 179-181]. There was complete tumor regression in about 30% of rats with F98 gliomas. The treatment group was administered a lipoplex-plasmid expressing Herpes simplex virus - thymidine kinase (HSV-tk) and also received a course of ganciclovir [196]. In the same study, animals treated with HSV-tk in an adenoviral vector had 70% complete tumor regression. Animals treated with a retroviral vector had no tumor regression, but the group size in the retroviral treated cohort was too small to draw any conclusions. The F98 glioma is reputed to be minimally immunogenic in the Fisher rat [44]; however, plasmid DNA and cationic lipids are very immunostimulating [205, 206]. The adenoviral and lipoplex vectors did not induce a significant infiltration of lymphocytes when administered via the osmotic minipump and were claimed by the authors to be well tolerated [168]. However the immunostimulating properties of DNA-lipid complexes may have contributed to the antitumor response.

37

The pronounced antitumor properties observed in animals treated with lipoplexes have been observed in immunocompromised mice; nude mice tumored with U251-SP human gliomas had a 100% survival rate when injected intratumorally with lipoplex carrying a plasmid expressing human beta interferon [177]. In this report, animals were dosed five times at two day intervals starting on day 7. Studies using this same vector in other models showed an increased survival time [178, 181] when treatment was initiated soon after tumor implantation (Table 5).

Targeted lipoplexes have been used to enhance the distribution of the lipoplexes from the injection site. A transferrin-targeted lipoplex that delivered a nerve growth factor transgene directly injected into the rat striatum enhanced gene transfer about three fold compared to a non-targeted lipoplex [185]. In addition to enhanced gene transfer, the transferrin targeting altered the distribution of transfected cells; nontargeted lipoplex transfection was primarily restricted to the vicinity of the needle tract, consistent with the restricted distribution of cationic lipoplexes administered into the caudate putamen via CED [135]. In contrast, transferrin-modified lipoplex transfected cells distant from the needle track throughout the striatum. Transgene expression was evident at 24 hours and returned to baseline at seven days post administration. The expression of the nerve growth factor attenuated a chemically induced lesion in the brain (Table 5).

Targeted lipoplexes have also been investigated for the delivery of RNAi and mRNA. Rats bearing a C6 glioma, which was permanently transfected with luciferase, received intravenous injection of lipoplexes targeted to the transferrin receptor containing anti-luciferase RNAi. When lipoplexes were administered 5 days following tumor implantation, luciferase expression fell by 90% for at least five days following injection.

The authors suggest that the transferrin targeting enables receptor mediated transcytosis across the BBB, enabling this system to be used for brain diseases where the BBB remains intact [84, 171]. A dual targeted lipoplex has been investigated for the delivery of mRNA [84]. These lipoplexes included targeting towards the transferrin receptor for BBB transcytosis and targeting towards the insulin receptor for transport across the plasma and nuclear membrane of the tumor cells. Intravenous injection of these lipoplexes delivering antisense EGFR at day 5 after U87 tumor implantation increased the mouse lifespan twofold. However, these systems have not yet been applied to improve therapy against diseases affecting normal brain where the BBB permeability may be lower compared to tumor models [84].

There are few reported human clinical trials of lipoplex administration directly into brain tumors (Table 5). Voges and coworkers treated eight glioblastoma patients with lipoplex delivery of HSV-tk with subsequent prodrug activation by intravenous ganciclovir [148]. Two of these patients showed a greater than 50% reduction in tumor volume and six showed focal treatment effects. These workers imaged and assessed the treatment effect in the tumor using MRI; they noted that placement of the catheter in the tumor was a significant factor that required optimization if gene therapy approaches were to achieve their full potential for treating brain tumors [148]. The gene expression of the HSV-tk using this delivery system was also followed by using I-124-labelled 2'-fluoro-2'-deoxy-1β-D-arabino-furanosyl-5-iodo-uracil ($[^{124}I]$–FIAU), a substrate of HSV-tk that is visible using PET [168].   In addition to the delivery of HSV-tk in human clinical trials, lipoplexes have also been used to deliver interferon-beta. Pilot studies of four malignant glioma patients showed that ten weeks after beginning the four week therapy, two

patients had stable disease and two patients had a greater than 50% reduction in tumor volume [188].

Lipoplexes have also been used to deliver genes in an attempt to correct a genetic neurodegenerative disorder known as Canavan disease, a spongiform brain degeneration related to a deficiency in functional aspartoacylase [187]. The aspartocylase gene lipoplex was injected intraventricularly in monkeys and two children. The lipoplexes, containing DC-cholesterol and the cations polylysine and protamine sulfate, were well tolerated and gene expression was detected at one month post-administration of the vector in monkeys. Lipoplex administration in the children was also well tolerated and both patients showed some improvement in clinical symptoms in addition to biochemical and radiological improvements.

These initial clinical trials of lipoplex administration into the brain have shown that non-viral gene therapy for the brain is generally safe and feasible. However, because only a small number of patients have been involved in these studies, it is not yet possible to draw conclusions about the efficacy of liposomal gene therapy to induce an anti-tumor response or prolong survival. Larger scale trials will benefit from a design that addresses the challenges common to both viral and non-viral gene delivery, particularly increasing the distribution from the site of injection and achieving prolonged gene transduction [207].

In addition to lipoplexes, polyplexes have been investigated for non-viral gene delivery. The majority of pre-clinical studies have investigated polyethylenimine (PEI)-mediated reporter gene transfection into normal brain following intraventricular or intracranial injection. Though there are few studies on delivery into tumor models, a

number of reports have detailed delivery into various other brain regions such as the brain stem, the substantia nigra, and the hippocampus (Table 6). Polyplex-mediated gene delivery has not yet been tested in clinical trials.

The polyplex-mediated delivery of reporter genes has been used to characterize the time frame and tissue volume of gene expression in the brain. Gene expression has been observed up to three months following delivery [198]. Transfection efficiency can be increased by using linear PEI instead of branched PEI [192] and by PEGylating the PEI [193]. In addition, as observed for targeted lipoplexes, targeted polyplexes increases transfection an order of magnitude compared to nontargeted vectors. Targeting also allows for the possibility of directing polyplex uptake and accumulation to a subset of neurons [195].

Though there are few studies on polyplex delivery of therapeutic genes, these reports have shown some promising results. Polyplexes carrying a nerve growth factor transgene injected into the rat septum provided a three-fold greater neuroprotective effect against tissue injury. This level of neuroprotection was 80-90% of that achievable by viral vector-mediated transfer [204]. Injection into the brain of polyplexes delivering the dopamine transporter gene results in gene expression for as long as 14 days; by delivering sense or antisense plasmid, the transporter expression could be directly controlled. Despite this positive result, transgene expression was limited to 800 μm from the needle track, indicating that an improved distribution system will be required before these polyplexes can be tested in clinical trials [199]. This conclusion is further supported by polyplex delivery of bcl-2 into the cerebral cortex. Gene expression was limited to 6 mm^3 but continued for more than three months post injection [198]. In spite of these

promising reports, more work is needed to optimize polyplex gene delivery and distribution within the brain before clinical trials are warranted.

I.4.4. Comparison of delivery strategies

Though the standard method of drug delivery is oral or by systemic injection, delivery by alternative methods has been used for most common small molecule chemotherapeutics to reduce systemic toxicity and increase the concentrations of drug in the brain (Figure 10A). Improvements in systemic delivery are successful at reducing systemic toxicity, but the global nature of oral and systemic delivery substantially increases normal brain drug exposure. This makes oral systemic delivery useful for treatment of diffuse brain disease where it is necessary to get drug to a large region of brain tissue.
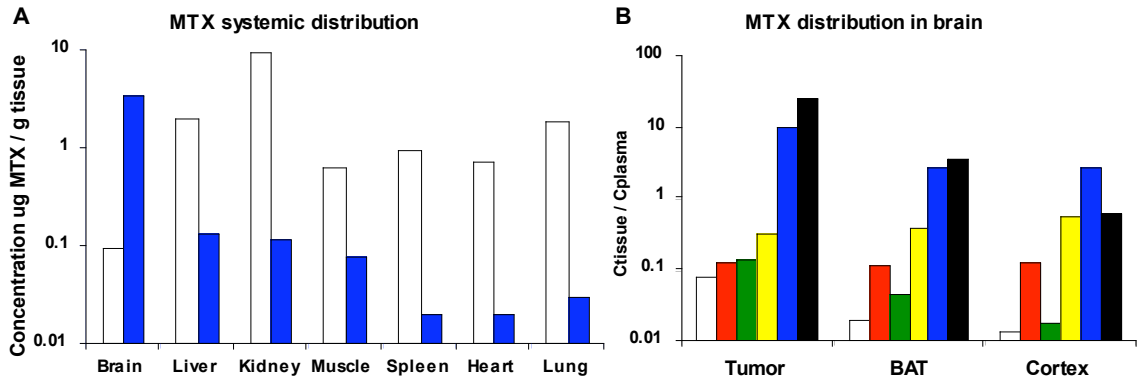
Figure 10. Methotrexate (MTX) accumulation in tumor, brain around tumor (BAT), normal cortex, and systemic tissues. A. Concentration of MTX in systemic tissues 30 min post injection of 1.25 mg (□, white) intravenously in the rat [208], and 20 min post (■, blue) intraventricular injection of 1.69 mg in the monkey [209]. Compared to intraventricular injection, intravenous delivery exposes the systemic tissues to higher levels of MTX, particularly the kidneys and liver which clear material from the blood. B. MTX accumulation in and near the tumor is substantially higher using (■, black) convection enhanced delivery or (■, blue) intrathecal routes compared to (□, white) intravenous, (■, red) intravenous with 25% mannitol BBB disruption, (■, green) intra-arterial, or (■, yellow) intra-arterial with 25% mannitol BBB disruption. Ratio of MTX concentration in tissue and plasma in tumor bearing rat brain at 30 min post injection [208], and in 1 hr post intrathecal injection in mice [210] and steady state during constant infusion CED in a patient [211].

For the treatment of a smaller brain region, intra-CSF or intraparenchymal methods should be used. Intra-CSF methods result in a high concentration of drug in the bulk CSF but limited penetration into the parenchyma. This makes intra-CSF delivery well-suited to distribute drugs against meningeal and ventricular diseases. To achieve high concentrations of drug in a local region within the parenchyma, intraparenchymal delivery is the best option because distribution is limited to a small volume near the needle tip. This is particularly useful for solid tumors and for degenerative diseases that are surgically accessible and confined to a single structure of the brain.

As an example, intraparenchymal, intra-CSF, and systemic methods have been used to distribute methotrexate in a solid brain tumor (Figure 10B). Drug delivery by CED or the intrathecal route results in the highest concentrations in the tumor and brain

surrounding tumor; intrathecal delivery into the bulk CSF results in a more global effect, increasing concentrations of methotrexate in the normal brain region [208, 210, 211]. The concentration of methotrexate in all brain regions is substantially higher by CED or by the intrathecal route compared to systemic delivery with and without BBB disruption.

I.5. Modeling

Compartmental models have been used to describe the distribution of drug within the brain since the mid-1970s. For example, Levin et al. [212] modeled drug distribution from the blood into a spherical tumor containing three regions: a poorly perfused low permeability center, a well-perfused high permeability outer shell, and an outermost shell with intermediate perfusion and permeability. This model could be used to predict the drug area under the curve (AUC) in the tumors with different blood flow when drugs of varying capillary permeability were administered intravenously.

Models have also been developed to characterize the diffusive transport of drugs throughout the parenchyma when the drugs are directly injected [213, 214] or implanted via a polymeric implant [215]. For example, Saltzman and Radomsky [215] modeled release, transport, and elimination of a drug from a polymeric implant using equations defining a mass balance for a differential volume tissue element [216]. This model was used to analyze previous data on dexamethasone distribution from a polymeric implant [215].

However, these models are inherently limited by the assumption that the tissue properties are uniform in all directions. Thus, though the models may predict sustained therapeutic levels of drug within the tumor space, this is unlikely to occur in animal or

human tumors. Tumor inhomogeneity can contribute to uneven drug distribution, leading to the development of drug resistance and tumor regrowth [3]. Further, invasive methods such as CED or polymer implantation lead to a measurable and significant inflammation and local edema [3]. This is nontrivial and can lead to convective mixing near the invasive site, altering the distribution of drug within the tumor and normal brain space. This adds to the difficulties involved in drawing conclusions about the efficacy of tumor treatment in pre-clinical studies.

More complex mathematical models more rigorously predict drug distribution and could help guide rational design of drugs and the development of drug delivery systems. In particular, transcapillary drug transfer across the BBB has been modeled by a number of techniques such as quantitative structure activity models and artificial neural networks [217, 218]. Finite element models have been used to portray the movement of drugs throughout the parenchymal space. The model of Kalyanasundaram and coworkers [219] includes 800 triangular elements that depict realistic brain anatomy and transport properties of gray and white matter, diffusion and convection in two directions, and the effects of ECF flow and edema. Model parameters were defined using MRI tracking of paramagnetic contrast markers from a polymeric implant and bolus intraparenchymal dose; the simulation was then used to predict the transport and distribution of a bolus intraparenchymal dose of interleukin 2. Though these simulations have a high level of detail, it is difficult to completely correlate these predictions with direct intraparenchymal measurements due to the technical feasibility of making such precise measurements and the high inter-animal variability. Nonetheless, models that incorporate realistic fluid flow properties in the brain and predict drug levels in various brain areas based upon the drug

input into different regions would be useful for the design and testing of alternative and novel dosing and delivery strategies to treat tumors.

I.6. Summary

Although a number of strategies have been developed to deliver drugs into the brain, patients with brain tumors continue to face a poor prognosis and limited treatment options that are unlikely to be resolved even as effective novel anticancer drugs are devised. This is because the physiology of the brain presents unique challenges, including tight regulation of what can enter the brain space, limited distribution of substances along ECF flow pathways, and clearance from the tissue by structures different from the conventional lymphatics found in peripheral tissues.

Pre-clinical studies have highlighted the importance of treating tumors early, at a stage where they are small enough to distribute the drug throughout the entire tumor. There are promising ways to improve brain tumor therapy, including intravenous therapies that exploit the leakiness of the tumor vasculature, targeting to tumor associated features or mechanisms that can be triggered to release drug in the tumor. Exploiting these possibilities depends upon the identification of appropriate targets in the tumor and the development of suitable ligands to bind to these targets. In addition, the introduction of multi-source CED [220, 221] to infuse drugs or drug carriers in multiple directions may increase drug delivery to tumors. The implementation of such approaches guided by MRI or far IR imaging technologies to position the infusion catheters in the appropriate locations could improve tumor drug delivery.

In addition to these promising advances, novel solutions that take into account the fluid handling characteristics of the brain clearly are required before effective treatments are realized for patients affected by brain tumors.

I.7. References

[1]   SEER: Surveillance, Epidemiology and End Results, National Cancer Institute,
       http://seer.cancer.gov/csr/19752001/sections.html (accessed 01 March 2005)

[2]   J.M. Legler, L.A. Gloeckler, M.A. Smith, J.L. Warren, E.F. Heineman, R.S. Kaplan, M.S.
       Linet, Brain and other central nervous system cancers: recent trends in incidence and mortality,
       J NCI. **91**(1999), pp. 1382-1390.

[3]   M.S. Berger and M. Bernstein, Neuro-oncology: the essentials, Thieme Medical Publishers,
       New York, NY, 2000.

[4]   W.M. Pardridge, Brain drug targeting: the future of brain drug development, Cambridge
       University Press, New York, NY, 2001.

[5]   W.M. Pardridge, Overcoming the blood-brain barrier, *Mol. Interventions.* **3** (2003), pp. 90-105.

[6]   D.J. Begley, Delivery of therapeutic agents to the central nervous system: the problems and
       possibilities, *Pharm. & Therapeutics.* **104** (2004), pp. 29-45.

[7]   E.M. Kemper, W. Boogerd, I. Thuis, J.H. Beijnen, O. van Tellingen, Modulation of the blood-
       brain barrier in oncology: therapeutic opportunities for the treatment of brain tumours?, *Cancer
       Treatment Reviews.* **30** (2004), pp. 415-423.

[8]   J. Rautio and P.J. Chikhale, Drug delivery systems for brain tumor therapy, *Current
       Pharm.Design.* **10** (2004), 1341-1353.

[9]   J.N. Rich and D.D. Bigner, Therapies in the treatment of malignant glioma, *Nat. Rev.: Drug
       Discovery.* **3** (2004), pp. 430-446.

[10]   J. Nolte, The human brain: an introduction to its functional anatomy, Mosby Inc., St. Louis,
       MO, 2002.

[11]   B. Mokri, The Monro-Kellie hypothesis: Applications in CSF volume depletion, *Neurology.* **56**
       (2001), pp. 1746-1748.

[12]   P.L. Golden & G.M. Pollack, Blood-brain barrier efflux transport, *J. Pharm Sci.* **92** (2003), pp.
       1739-1753.

[13]   H. Davson and M.B. Segal, Physiology of the CSF and the Blood-brain barriers, CRC, Boca-
       Raton, FL, 1996.

[14]   P.C. Buijs, M.J. Krabbe-Hartkamp, C.J. Bakker, E.E. de Lange, L.M. Ramos, M.M. Breteler,
       W.P. Mali, Effect of age on cerebral blood flow: measurement with ungated two-dimensional
       phase-contrast MR angiography in 250 adults, *Radiology.* **209** (1998), pp. 667-674.

[15]   M.B. Segal. The choroid plexuses and the barriers between the blood and the cerebrospinal
       fluid, *Cellular and Mol. Neurobiology.* **20** (2000), pp. 183-194.

[16]   I. Szentistvanyi, C.S. Patlak, R.A. Ellis, H.F. Cserr, Drainage of interstitial fluid from different
       regions of rat brain, *Am. J. Phys.* **246** (1984), pp. F835-844, 1984.

[17]   E.E. Chaffee & E.M. Greisheimer, Basic physiology and anatomy, Lippincott Press,
       Philadelphia, PA, 1974.

[18]   R.W. Greenberg, E.L. Lane, J. Cinnamon, P. Farmer, R.A. Hyman, The cranial meninges:
       anatomic considerations, *Semin Ultrasound CT MR.* **15** (1994), pp. 454-465.

[19]   G.J. Dohrmann, The choroid plexus: a historical review, *Brain Res.* **18** (1970), pp. 197-218.

[20]   J.L. Venero, M.L. Vizuete, A. Machado, J. Cano, Aquaporins in the central nervous system,
       Progress in Neurobiology. **63** (2001), pp. 321-336.

[21]   M. Amiry-Moghaddam, O.P. Ottersen, The molecular basis of water transport in the brain,
       Nature Reviews: Neuroscience, **4** (2003), pp. 991-1001.

[22]   M.W.B. Bradbury and H.F. Cserr, in: M.G. Johnston (Ed.), Res. Monographs in Cell and
       Tissue Phys, Vol. 9, Elsevier, New York, 1985, pp. 355-394.

[23]   M. Boulton M, M. Flessner, D. Armstrong, R. Mohamed, J. Hay, M. Johnston, Contribution of
       extracranial lymphatics and arachnoid villi to the clearance of a CSF tracer in the rat, *Am. J.
       Phys.* **276** (1999), pp. R818-823.

[24]   M.L. Upton and R.O. Weller, The morphology of cerebrospinal fluid drainage pathways in
       human arachnoid granulations, *J. Neurosurg.* **63** (1985), pp. 867-875.

[25]   N. Cauma E.H. Hinderer, Fine structure of blood vessels of the human nasal respiratory mucosa, *Ann. Otol. Rhinol. Laryngol.* **78** (1969), pp. 865-879.

[26]   P. Knox and J.J. Pflug, The effect of the canine popliteal node on the composition of lymph, *J. Phys.* **345** (1983), pp. 1-14.

[27]   M.W.B. Bradbury and R.J. Westrop, in: K. Shapiro and A. Marmarou (Eds.), Hydroencephalus, Raven Press, New York, 1983, pp. 69-81.

[28]   L.L. Rubin and J.M. Staddon, The cell biology of the blood-brain barrier, *Ann. Rev. Neurosci.* **22** (1999), pp. 11-28.

[29]   E.M. Renkin, Transport pathways through capillary endothelium, *Microvas. Res.* **15** (1978), pp. 123-135.

[30]   N.J. Abbott, Evidence for bulk flow of brain interstitial fluid: significance for physiology and pathology, *Neurochem. Int.* **45** (2000), pp. 545-552.

[31]   C.P. Geer and S.A. Grossman, Interstitial fluid flow along white matter tracts : A potentially important mechanism for the dissemination of primary brain tumors, *J. Neuro-Oncology.* **32** (1997), pp. 193-201.

[32]   M.L. Rennels, T.F. Gregory, O.R. Blaumanis, K. Fujimoto, P.A. Grady, Evidence for a 'paravascular' fluid circulation in the mammalian central nervous system, provided by the rapid distribution of tracer protein throughout the brain from the subarachnoid space, *Brain Res.* **326** (1985), pp. 47-63.

[33]   R.O. Weller, R.S. Kida, E.T. Zhang, Pathways of fluid drainage from the brain – Morphological aspects and immunological significance in rat and man, *Brain Path.* **2** (1992), pp. 277-284.

[34]   E.T. Zhang, H.K. Richards, S. Kida, R.O. Weller, Directional and compartmentalized drainage of interstitial fluid and cerebrospinal fluid from the rat brain, *Acta Neuropath.* **83** (1992), pp. 233-239.

[35]   M.M.J. Polfliet, P.H. Goede, E.M.L. van Kesteren-Hendrikx, N. van Rooijen, C.D. Dijkstra, T.K. van den Berg, A method for the selective depletion of perivascular and meningeal macrophages in the central nervous system, *J. Neuroimmunol.* **116** (2001), pp. 188-195.

[36]   F.Z. Yetkin and D. Mendelsohn, Hypoxia imaging in brain tumors, *Neuroimaging Clin. N. Am.* **12** (2002), pp. 537-542.

[37]   M.P. Lovely, Symptom management of brain tumor patients, *Seminars in Oncology Nursing.* **20** (2004), pp. 273-283.

[38]   Y. Boucher, L.T. Baxter, R.K. Jain, Interstitial pressure gradients in tissue-isolated and subcutaneous tumors: implications for therapy, *Cancer Res.* **50** (1990), pp. 4478-4484.

[39]   K.E. Schlageter, P. Molnar, G.D. Lapin, D.R. Groothuis, Microvessel Organization and structure in experimental brain tumors: microvessel populations with distinctive structural and functional properties, *Microvas Res.* **58** (1999), pp. 312-328.

[40]   P. Vajkoczy and M.D. Menger, Vascular microenvironment in gliomas, *J. Neuro-Oncology.* **50** (2000), pp. 99-108.

[41]   M.C. Papadopoulos, S. Krishna A.S. Verkman, Aquaporin water channels and brain edema, *Mt. Sinai J. of Med.* **69** (2002), pp. 242-248.

[42]   J. Badaut, F. Lasbennes, P.J. Magistretti, L. Regli, Aquaporins in brain: Distribution, physiology and pathophysiology, *J. Cereb. Blood Flow Metab.* **22** (2002), pp. 367-378.

[43]   A. Regina, M. Demeule, A. Laplante, J. Jodoin, C. Dagenais, F. Berthelet, A. Moghrabi, R. Beliveau, Multidrug resistance in brain tumors: roles of the BBB, *Cancer and Metastasis Reviews.* **20** (1-2):13-25, 2001.

[44]   R.F. Barth, Rat brain tumor models in experimental neuro-oncology: the 9L, C6, T9, F98, RG2 (D74), RT-2 and CNS-1 Gliomas, *J. Neuro-oncology.* **36** (1998), pp. 91-102.

[45]   K. Camphausen, B. Purow, M. Sproull, T. Scott, T. Ozawa, D.F. Deen, P.J. Tofilon, Influence of in vivo growth on human glioma cell line gene expression: convergent profiles under orthotopic conditions, *PNAS.* **102** (2005), pp. 8287-8292.

[46]   R.F. Barth, W. Yang, J.A. Coderre, Rat brain tumor models to assess the efficacy of boron neutron capture therapy: a critical evaluation, *J. Neuro-Oncology* **62** (2003), pp. 61-74.

[47]   R.D. Fross, P.C. Warnke, D.R. Groothuis, Blood flow and blood-to-tissue transport in 9L gliosarcomas: the role of the brain tumor model in drug delivery research, *J. Neurooncol.* **11** (1991), pp. 185-197.

[48]   G. Hesselager and E.C. Holland, Using mice to decipher the molecular genetics of brain tumors. *Neurosurgery.* **53** (2003), pp. 685-695.

[49]   M. Patel, C. McCully, K. Godwin, F.M. Balis, Plasma and cerebrospinal fluid pharmacokinetics of intravenous temozolomide in non-human primates, *J. Neuro-oncol.* **61** (2003), pp. 203-207.

[50]   Carpentier AF, Neuro-oncology: the growing role of chemotherapy in glioma, *Lancet: Neur.* **4** (2005), pp. 4-5.

[51]   E.H. Lo, A.B. Singhal, V.P. Torchilin, N.J. Abbott, Drug delivery to damaged brain, *Brain Res. Rev.* **38** (2001), pp. 140-148.

[52]   C.V. Borlongan, D.F. Emerich, Facilitation of drug entry into the CNS via transient permeation of blood brain barrier: laboratory and preliminary clinical evidence from bradykinin receptor agonist, Cereport, *Brain Res Bull.* **60** (2003), pp. 297-306.

[53]   S.I. Rapoport, Osmotic opening of the blood-brain barrier: Principles, mechanism and therapeutic applications, *Cellular and Mol. Neurobiol.* **20** (2000), pp. 217-230.

[54]   N.D. Doolittle, A. Petrillo, S. Bell, P. Cummings, S. Eriksen, Blood-brain barrier disruption for the treatment of malignant brain tumors: The National Program, *J. Neurosci. Nurs.* **30**(1992), pp. 81-90.

[55]   H. Maeda, J. Fang, T. Inutsuka, Y. Kitamoto, Vascular permeability enhancement in solid tumor: various factors, mechanisms involved and its implications, *Int. Immunopharmacol.***3** (2003), pp. 319-328.

[56]   K. Kakinuma, R. Tanaka, H. Takahashi, M. Watanabe, T. Nakagawa, M. Kuroki, Targeting chemotherapy for malignant brain tumor using thermosensitive liposome and localized hyperthermia, *J. Neurosurg.* **84** (1996), pp. 180-184.

[57]   T. Siegal, A. Horowitz, A. Gabizon, Dosorubicin encapsulated in sterically stabilized liposomes for the treatment of a brain tumor model: biodistribution and therapeutic efficacy, *J. Neurosurg.* **83** (1995), pp. 1029-1037.

[58]   U.S. Sharma, A. Sharma, R.I. Chau, R.M. Straubinger, Liposome-mediated therapy of intracranial brain tumors in a rat model, *Pharm. Res.* **14** (1997), pp. 992-998.

[59]   R. Zhou, R. Mazurchuk, R.M. Straubinger, Antivasculature effects of doxorubicin-containing liposomes in an intracranial rat brain tumor model, *Cancer Res.* **62** (2002), pp. 2561-2566.

[60]   H. Aoki, K. Kakinuma, K. Morita, M. Kato, T. Uzuka, G. Igor, H. Takahashi, R. Tanaka, Therapeutic efficacy of targeting chemotherapy using local hyperthermia and thermosensitive liposome: evaluation of drug distribution in a rat glioma model, *Int. J. Hyperthermia.* **20** (2004), pp. 595-605.

[61]   E. Barbarese, S.Y. Ho, J.S. D'Arrigo, R.H. Simon, Internalization of microbubbles by tumor cells in vivo and in vitro, *J. Neurooncol.* **26** (1995), pp. 25-34.

[62]   S.Y. Ho, E. Barbarese, J.S. D'Arrigo, C. Smith-Slatas, R.H. Simon, Evaluation of lipid-coated microbubbles as a delivery vehicle for Taxol in brain tumor therapy, *Neurosurgery.* **40** (1997), pp. 1260-68.

[63]   F. Jiang, L. Lilge, J. Grenier, Y. Li, M.D. Wilson, M. Chopp, Photodynamic therapy of U87 human glioma in nude rat using liposome-delivered photofrin, *Lasers Surg. Med.* **22** (1998), pp. 74-80.

[64]   F. Jiang, L. Lilge, M. Belcuig, G. Singh, J. Grenier, Y. Li, M. Chopp, Photodynamic therapy using Photofrin in combination with buthionine sulfoximine (BSO) to treat 9L gliosarcoma in rat brain, *Lasers Surg. Med.* **23** (1998), pp. 161-166.

[65]   F. Jiang, L. Lilge, B. Logie, Y. Li, M. Chopp, Photodynamic therapy of 9L gliosarcoma with liposome-delivered photofrin, *Photochem. Photobiol.* **65** (1997), pp. 701-706.

[66]   G. Schackert, D. Fan, R. Nayar, I.J. Fidler, Arrest and retention of multilamellar liposomes in the brain of normal mice or mice bearing experimental brain metastases, *Sel. Cancer Ther.* 5 (1989), pp. 73-79.

[67] S. Shibata, A. Ochi, K. Mori, Liposomes as carriers of cisplatin into the central nervous system--experiments with 9L gliomas in rats, *Neurol. Med. Chir. (Tokyo).* **30** (1990), pp. 242-245.

[68] S. Shibata, T. Jinnouchi, K. Mori K, Ultrastructural study of capillary permeability of liposome-encapsulated cisplatin in an experimental rat brain tumor model, *Neurol. Med. Chir. (Tokyo).* **29** (1989), pp. 696-700.

[69] F. Hong and E. Mayhew E, Therapy of central nervous system leukemia in mice by liposome-entrapped 1-beta-D-arabinofuranosylcytosine, *Cancer Res.* **49** (1989), pp. 5097-5102.

[70] M. Werthle, D. Bochelen, M. Adamczyk, A. Kupferberg, P. Poulet, J. Chambron, P. Lutz, A. Privat, M. Mersel, Local administration of 7 beta-hydroxycholesteryl-3-oleate inhibits growth of experimental rat C6 glioblastoma, *Cancer Res.* **54** (1994), pp. 998-1003.

[71] B. Ji, W. Chen, D.R. Lu, D.S. Halpern, Cell culture and animal studies for intracerebral delivery of borocaptate in liposomal formulation, *Drug Deliv.* **8** (2001), pp.13-17.

[72] C. Mamot, J.B. Nguyen, M. Pourdehnad, P. Hadaczek, R. Saito, J.R. Bringas, D.C. Drummond, K. Hong, D.B. Kirpotin, T. McKnight, M.S. Berger, J.W. Park, K.S. Bankiewicz, Extensive distribution of liposomes in rodent brains and brain tumors following convection-enhanced delivery, *J. Neurooncol.* **68** (2004), pp. 1-9.

[73] R. Saito, J.R. Bringas, T.R. McKnight, M.F. Wendland, C. Mamot, D.C. Drummond, D.B. Kirpotin, J.W. Park, M.S. Berger, K.S. Bankiewicz, Distribution of liposomes into brain and rat brain tumor models by convection-enhanced delivery monitored with magnetic resonance imaging, *Cancer Res.* **64** (2004), pp. 2572-2579

[74] R.J.J. Lippens, Liposomal daunorubicin (DaunoXome) in children with recurrent or progressive brain tumors, *Ped. Hema. Oncol.* **16** (1999), pp. 131-139.

[75] M. Zucchetti, A. Boiardi, A. Silvani, I. Parisi, S. Piccolrovazzi, M. D'Incalci. Distribution of daunorubicin and daunorubicinol in human glioma tumors after administration of liposomal daunorubicin, *Cancer Chemother. Pharmacol.* **44** (1999), pp. 173-176.

[76] A. Fiorillo, G. Maggi, N. Greco, R. Migliorati, A. D'Amico, M.D. De Caro, M.S. Sabbatino, F. Buffardi, Second-line chemotherapy with the association of liposomal daunorubicin, carboplatin and etoposide in children with recurrent malignant brain tumors, *J. Neurooncol.* **66** (2004), pp.179-185.

[77] M.I. Koukourakis, S. Koukouraki, I. Fezoulidis, N. Kelekis, G. Kyrias, S. Archimandritis, N. Karkavitsas, High intratumoural accumulation of stealth liposomal doxorubicin (Caelyx) in glioblastomas and in metastatic brain tumours, *Br. J. Cancer.* **83** (2000), pp. 1281-1286.

[78] N.M. Marina, D. Cochrane, E. Harney, K. Zomorodi, S. Blaney, N. Winick, M. Bernstein, M.P. Link, Dose escalation and pharmacokinetics of pegylated liposomal doxorubicin (Doxil) in children with solid tumors: a pediatric oncology group study, *Clin. Cancer Res.* **8** (2002), pp. 413-418.

[79] P. Hau, K. Fabel, U. Baumgart, P. Rummele, O. Grauer, A. Bock, C. Dietmaier, W. Dietmaier, J. Dietrich, C. Dudel, F. Hubner, T. Jauch, E. Drechsel, I. Kleiter, C. Wismeth, A. Zellner, A. Brawanski, A. Steinbrecher, J. Marienhagen, U. Bogdahn, Pegylated liposomal doxorubicin-efficacy in patients with recurrent high-grade glioma, *Cancer.* **100** (2004), pp. 1199-1207.

[80] A. Khalifa, D. Dodds, R. Rampling, J. Paterson, T. Murray, Liposomal distribution in malignant glioma: possibilities for therapy, *Nucl. Med. Commun.* **18** (1997), pp. 17-23.

[81] G.B. Firth, M. Firth, R.O. McKeran, J. Rees, P. Walter, D. Uttley, V. Marks, Application of radioimmunoassay to monitor treatment of human cerebral gliomas with bleomycin entrapped within liposomes, *J. Clin. Pathol.* **41** (1988), pp. 38-43.

[82] J. Huwyler, D. Wu, W.M. Pardridge, Brain drug delivery of small molecules using immunoliposomes, *PNAS.* **93** (1996), pp. 14164-14169.

[83] N. Shi, Y. Zhang Y, C. Zhu, R.J. Boado, W.M. Pardridge, Brain-specific expression of an exogenous gene after i.v. administration, *PNAS.* **98** (2001), pp. 12754-12759.

[84] Y. Zhang, C. Zhu, W.M. Pardridge, Antisense gene therapy of brain cancer with an artificial virus gene delivery system, *Mol. Ther.* **6** (2002), pp. 67-72.

[85] C.O. Noble, D.B. Kirpotin, M.E. Hayes, C. Mamot, K. Hong, J.W. Park, C.C. Benz, J.D. Marks, D.C. Drummond, Development of ligand-targeted liposomes for cancer therapy, *Expert Opin. Ther. Targets*.**8** (2004), pp. 335-353.

[86] J.F. Strasser, L.K. Fung, S. Eller, S.A. Grossman, W.M. Saltzman, Distribution of 1,3-bis(2-chloroethyl)-1-nitrosourea and tracers in the rabbit brain after interstitial delivery by biodegradable polymer implants, *J. Pharm. Exp. Ther.* **275** (1995), pp. 1647-1655.

[87] E.P. Sipos, B. Tyler, S. Piantadosi, P.C. Burger, H. Brem, Optimizing interstitial delivery of BCNU from controlled release polymers for the treatment of brain tumors, *Cancer Chemother. Pharmacol.* **39** (1997), pp. 383-389.

[88] M.G. Ewend, P. Sampath, J.A. Williams, B.M. Tyler, H. Brem, Local delivery of chemotherapy prolongs survival in experimental brain metastases from breast carcinoma, *Neurosurgery*. **43** (1998), pp. 1185-1193.

[89] L.D. Rhines, P. Sampath, M.E. Dolan, B.M. Tyler, H. Brem, J. Weingart, O6-benzylguanine potentiates the antitumor effect of locally delivered carmustine against an intracranial rat glioma, *Cancer Res*. **60** (2000), pp. 6307-6310.

[90] P.B. Storm, J.L. Moriarity, B. Tyler, P.C. Burger, H. Brem, J. Weingart. Polymer delivery of camptothecin against 9L gliosarcoma: release, distribution, and efficacy, *J. Neurooncol*. **56** (2002), pp. 209-217.

[91] Q. Kong, B.K. Kleinschmidt-Demasters, K.O. Lillehei, Intralesionally implanted cisplatin cures primary brain tumor in rats, *J. Surg. Oncol*. **64** (1997), pp. 268-273.

[92] K.D. Judy, A. Olivi, K.G. Buahin, A. Domb, J.I. Epstein, O.M. Colvin, H. Brem, Effectiveness of controlled release of a cyclophosphamide derivative with polymers against rat gliomas, *J. Neurosurg*. **82** (1995), pp. 481-486.

[93] R.J. Tamargo, A.K. Sills Jr, C.S. Reinhard, M.L. Pinn, D.M. Long, H. Brem, Interstitial delivery of dexamethasone in the brain for the reduction of peritumoral edema, *J. Neurosurg*. **74** (1991), pp. 956-961.

[94] W.H. Tan, T. Lee, C.H. Wang, Simulation of intratumoral release of Etanidazole: effects of the size of surgical opening, *J. Pharm. Sci*. **92** (2003), pp. 773-789.

[95] W.H. Tan, F. Wang, T. Lee, C.H. Wang, Computer simulation of the delivery of etanidazole to brain tumor from PLGA wafers: comparison between linear and double burst release systems, *Biotechnol. Bioeng*. **82** (2003), pp. 278-288.

[96] X. Yuan, L.E. Dillehay, J.R. Williams, V.R. Shastri, J.A. Williams, IUdR polymers for combined continuous low-dose rate and high-dose rate sensitization of experimental human malignant gliomas, *Int. J. Cancer*. **96** (2001), pp. 118-125.

[97] W. Dang, O.M. Colvin, H. Brem, W.M. Saltzman, Covalent coupling of methotrexate to dextran enhances the penetration of cytotoxicity into a tissue-like matrix, *Cancer Res*. **54** (1994), pp. 1729-1735.

[98] J.L. Frazier, P.P. Wang, D. Case, B.M. Tyler, G. Pradilla, J.D. Weingart, H. Brem, Local delivery of minocycline and systemic BCNU have synergistic activity in the treatment of intracranial glioma, *J. Neuro-oncol*. **64** (2003), pp. 203-209.

[99] M. Saini, F. Roser, S. Hussein, M. Samii, M. Bellinzona, Intralesional mitoxantrone biopolymer-mediated chemotherapy prolongs survival in rats with experimental brain tumors, *J. Neuro-Oncol*. **68** (2004), pp. 225-232.

[100] W.M. Saltzmanm M.W. Mak, M.J. Mahoney, E.T. Duenas, J.L. Cleland, Intracranial delivery of recombinant nerve growth factor: release kinetics and protein distribution for three delivery systems, *Pharm. Res*. **16** (1999), pp. 232-240.

[101] K.A. Walter, M.A. Cahan, A. Gur, B. Tyler, J. Hilton, O.M. Colvin, P.C. Burger, A. Domb, H. Brem, Interstitial taxol delivered from a biodegradable polymer implant against experimental malignant glioma, *Cancer Res*. **54** (1994), pp. 2207-2212.

[102] M. Bellinzona, F. Roser, C. Matthies, M. Samii, M. Saini, Biopolymer-mediated suramin chemotherapy in the treatment of experimental brain tumours, *Acta Oncol*. **43 (**2004), pp. 259-263.

[103] R. Sutton, N. Yu, E. Luck, D. Brown, F. Conley, Reduction of vinblastine neurotoxicity in mice utilizing a collagen matrix carrier, *Sel. Cancer Ther.* **6** (1990), pp. 35-49.

[104] R.F. Barth, W. Yang, D.M. Adams, J.H. Rotaru, S. Shukla, M. Sekido, W. Tjarks, R.A. Fenstermaker, M. Ciesielski, M.M. Nawrocky, J.A. Coderre JA, Molecular targeting of the epidermal growth factor receptor for neutron capture therapy of gliomas, *Cancer Res.* **62** (2002), pp. 3159-3166.

[105] Y. Li, A. Owusu, S. Lehnert, Treatment of intracranial rat glioma model with implant of radiosensitizer and biomodulator drug combined with external beam radiotherapy, *Int. J. Radiat. Oncol. Biol. Phys.* **58** (2004), pp. 519-527.

[106] D.F. Emerich, S.R. Winn, Y. Hu, J. Marsh, P. Snodgrass, D. LaFreniere, T. Wiens, B.P. Hasler, R.T. Bartus, Injectable chemotherapeutic microspheres and glioma I: enhanced survival following implantation into the cavity wall of debulked tumors, *Pharm. Res.* **17** (2000), pp. 767-775.

[107] D.F. Emerich, S.R. Winn, R.T. Bartus, Injection of chemotherapeutic microspheres and glioma. IV: Eradicating tumors in rats, *Cell Transplant.* **11** (2002), pp. 47-54.

[108] L. Lemaire, V.G. Roullin, F. Franconi, M.C. Venier-Julienne, P. Menei, P. Jallet, J.J. Le Jeune, J.P. Benoit, Therapeutic efficacy of 5-fluorouracil-loaded microspheres on rat glioma: a magnetic resonance imaging study, *NMR Biomed.* **14** (2001), pp. 360-366.

[109] V.G. Roullin, J.R. Deverre, L. Lemaire, F. Hindre, M.C. Venier-Julienne, R. Vienet, J.P. Benoit, Anti-cancer drug diffusion within living rat brain tissue: an experimental study using [3H](6)-5-fluorouracil-loaded PLGA microspheres, *Eur. J. Pharm. Biopharm.* **53** (2002), pp. 293-299.

[110] F. Miura, S. Moriuchi, M. Maeda, A. Sano, M. Maruno, A.M. Tsanaclis, R. Marino Jr, J.C. Glorioso, T. Yoshimine, Sustained release of low-dose ganciclovir from a silicone formulation prolonged the survival of rats with gliosarcomas under herpes simplex virus thymidine kinase suicide gene therapy, *Gene Ther.* **9** (2002), pp. 1653-1658.

[111] M. Maeda, S. Moriuchi, A. Sano, T. Yoshimine, New drug delivery system for water-soluble drugs using silicone and its usefulness for local treatment: application of GCV-silicone to GCV/HSV-tk gene therapy for brain tumor, *J. Control Release.* **84** (2002), pp. 15-25.

[112] B. Rama, T. Mandel, J. Jansen, E. Dingeldein, H.D. Mennel. The intraneoplastic chemotherapy in a rat brain tumour model utilizing methotrexate-polymethylmethacrylate-pellets, *Acta Neurochir (Wien).* **87** (1987), pp. 70-75.

[113] J. Kreuter, R.N. Alyautdin, D.A. Kharkevich, A.A. Ivanov, Passage of peptides through the blood-brain barrier with colloidal polymer particles (nanoparticles), *Brain Res.* **674** (1995), pp. 171-174.

[114] I. Brigger, J. Morizet, L. Laudani, G. Aubert, M. Appel, V. Velasco, M.J. Terrier-Lacombe, D. Desmaele, J. d'Angelo, P. Couvreur, G. Vassal, Negative preclinical results with stealth nanospheres-encapsulated Doxorubicin in an orthotopic murine brain tumor model, *J. Control Release.* **100** (2004), pp. 29-40.

[115] S.C. Steiniger, J. Kreuter, A.S. Khalansky, I.N. Skidan, A.I. Bobruskin, Z.S. Smirnova, S.E. Severin, R. Uhl, M. Kock, K.D. Geiger, S.E. Gelperina, Chemotherapy of glioblastoma in rats using doxorubicin-loaded nanoparticles, *Int. J. Cancer.* **109** (2004), pp. 759-767.

[116] R.N. Alyautdin, V.E. Petrov, K. Langer, A. Berthold, D.A. Kharkevich, J. Kreuter, Delivery of loperamide across the blood-brain barrier with polysorbate 80-coated polybutylcyanoacrylate nanoparticles, *Pharm. Res.* **14** (1997), pp. 325-328.

[117] J.M. Koziara, P.R. Lockman, D.D. Allen, R.J. Mumper, Paclitaxel nanoparticles for the potential treatment of brain tumors, *J. Cont. Release.* **99** (2004), pp. 259-269.

[118] R.N. Alyautdin, E.B. Tezikov, P. Ramge, D.A. Kharkevich, D.J. Begley, J. Kreuter, Significant entry of tubocurarine into the brain of rats by adsorption to polysorbate 80-coated polybutylcyanoacrylate nanoparticles: an in situ brain perfusion study, *J. Microencap.* **15** (1998), pp. 67-74.

[119] A.E. Gulyaev, S.E. Gelperina, I.N. Skidan, A.S. Antropov, G.Y. Kivman, J. Kreuter, Significant transport of doxorubicin into the brain with polysorbate 80-coated nanoparticles, *Pharm Res.* **16** (1999), pp. 1564-1569.

[120] C.V. Borlongan, D.F. Emerich, Facilitation of drug entry into the CNS via transient permeation of blood brain barrier: laboratory and preliminary clinical evidence from bradykinin receptor agonist, Cereport, *Brain Res Bull.* **60** (2003), pp. 297-306.

[121] S.I. Rapoport, Osmotic opening of the blood-brain barrier: Principles, mechanism and therapeutic applications, *Cellular and Mol. Neurobiol.* **20** (2000), pp. 217-230.

[122] E. Zylber-Katz, J.M. Gomori, A. Schwartz, A. Lossos, F. Bokstein, T. Siegal, Pharmacokinetics of methotrexate in cerebrospinal fluid and serum after osmotic blood-brain barrier disruption in patients with brain lymphoma, *Clin. Pharmacol. Ther.* **67** (2000), pp.631-641.

[123] L.D. McAllister, N.D. Doolittle, P.E. Guastadisegni, D.F. Kraemer, C.A. Lacy, J.R. Crossen, E.A. Neuwelt. Cognitive outcomes and long-term follow-up results after enhanced chemotherapy delivery for primary CNS lymphoma, *Neurosurg.* **46** (2000), pp. 51-61.

[124] N.D. Doolittle, A. Petrillo, S. Bell, P. Cummings, S. Eriksen, Blood-brain barrier disruption for the treatment of malignant brain tumors: The National Program, *J. Neurosci. Nurs.* **30**(1992), pp. 81-90.

[125] G. Hocking and J.A.W. Wildsmith, Intrathecal drug spread, *Br. J. Anaesthesia.* **93**(2004), pp. 568-578.

[126] D.R. Groothuis, H. Benalcazar, C.V. Allen, R.M. Wise, C. Dills, C. Dobrescu, V. Rothholtz, and R.M. Levy, Comparison of cytosine arabinoside delivery to rat brain by intravenous, intrathecal, intraventricular and intraparenchymal routes of administration, *Brain Res.* **856** (2000), pp. 281-290.

[127] N. Savarj, L.G. Feun, K. Lu, K. Gray, C. Wang, T.L. Loo, Pharmacology of intrathecal VP-16-213 in dogs, *J. Neuro-Oncology.* **13** (1992), pp. 211-215.

[128] J.Z. Kerr, S. Berg, S.M. Blaney, Intrathecal chemotherapy, *Crit. Rev. in Onc/Hematology.* **37** (2001), pp. 227-236.

[129] A.K. Ommaya, Implantable devices for chronic access and drug delivery to the central nervous system, *Cancer Drug Delivery.* **1** (1984), pp. 169-179.

[130] S. Dakhil, W. Ensminger, G. Kindt, J. Niederhuber, W. Chandler, H. Greenberg, R. Wheeler, Implanted system for intraventricular drug infusion in central nervous system tumors, *Cancer Treat. Rep.* **65** (1981), pp. 401-411.

[131] P. Lord, H. Allami, M. Davis, R. Diaz, P. Heck, R. Fischell, MiniMed Technologies Programmable Implantable Infusion System, *Ann. NY Acad. Sci.* **531** (1988), pp. 66-71.

[132] K.T. Heruth, Medtronic SynchroMed drug administration system, *Ann. N.Y. Acad Sci.* **531** (1988), pp. 72-75.

[133] G. Fleischhack, S. Reif, C. Hasan, U. Jaehde, S. Hettmer, U. Bode, Feasibility of intraventricular administration of etoposide in patients with metastatic brain tumors, *Br. J. Cancer.* **84**(2001), pp. 1453-9.

[134] D.J. Murry and S.M. Blaney, Clinical pharmacology of encapsulated sustained-release cyarabine, *Ann. Pharmacotherapy.* **34** (2000), pp. 1173-1177.

[135] J.A. MacKay, D.F. Deen, F.C. Szoka Jr, Distribution in brain of liposomes after convection enhanced delivery; modulation by particle charge, particle diameter, and presence of steric coating, *Brain Res.* **1035** (2005), pp. 129-53.

[136] R.H. Bobo, D.W. Laske, A. Akbasak, P.F. Morrison, R.L. Dedrick, E.H. Oldfield, Convection-enhanced delivery of macromolecules in the brain, *PNAS.* **91** (1994), pp. 2076-2080.

[137] K. Kawakami, M. Kawakami, M. Kioi, S.R. Husain, R.K. Puri, Distribution kinetics of targeted cytotoxin in glioma by bolus or convection-enhanced delivery in a murine model, *J. Neurosurg.* **101** (2004), pp. 1004-11.

[138] Z. Lidar, Y. Mardor, T. Jonas, R. Pfeffer, M. Faibel, D. Nass, M. Hadani, Z. Ram, Convection-enhanced delivery of paclitaxel for the treatment of recurrent malignant glioma: a phase I/II clinical study, *J. Neurosurg.* **100** (2004), pp. 472-9.

[139] S.R. Husain and R.K. Puri, Interleukin-13 receptor-directed cytotoxin for malignant glioma therapy: from bench to bedside, *J.Neuro-Oncology*. **65** (2003), pp. 37-48.

[140] J. Zhu, L. Zhang, U.K. Hanisch, P.L. Felgner, R. Reszka, A continuous intracerebral gene delivery system for in vivo liposome-mediated gene therapy, *Gene Ther*. **3** (1996), pp. 472-476.

[141] R. Reszka, J.H. Zhu, F. Weber, W. Walther, R. Greferath, S. Dyballa. Liposome mediated transfer of marker and cytokine genes into rat and human glioblastoma cells in vitro and in vivo. *J. Lipos. Res*. **5** (1995), pp. 149-167.

[142] J. Cunningham, Y. Oiwa, D. Nagy, G. Podsakoff, P. Colosi, K.S. Bankiewicz, Distribution of AAV-TK following intracranial convection enhanced delivery into rats, *Cell Transplant*. **9** (2000), pp. 585-594.

[143] W. Yang, R.F. Barth, D.M. Adams, M.J. Ciesielski, R.A. Fenstermaker, S. Shukla, W. Tjarks, M.A. Caligiuri, Convection-enhanced delivery of boronated epidermal growth factor for molecular targeting of EGF receptor-positive gliomas. *Cancer Res*. **15** (2002), pp. 6552-6558.

[144] C. Mamot, J.B. Nguyen, M. Pourdehnad, P. Hadaczek, R. Saito, J.R. Bringas, D.C. Drummond, K. Hong, D.B. Kirpotin, T. McKnight, M.S. Berger, J.W. Park, K.S. Bankiewicz, Extensive distribution of liposomes in rodent brains and brain tumors following convection-enhanced delivery, *J. Neurooncol*. **68** (2004), pp. 1-9.

[145] E.A. Chiocca, W.C. Broaddus, G.T. Gillies, T. Visted, M.L.M. Lamfers, Neurosurgical delivery of chemotherapeutics, targeted toxins, genetic and viral therapies in neuro-oncology, *J. Neuro-oncology*. **69** (2004), pp. 101-117.

[146] W.J. Bodell, D.D. Giannini, S. Hassenbusch, V.A. Levin, Levels of N7-(2-hydroxyethyl)guanine as a molecular dosimeter of drug delivery to human brain tumors, *Neuro-Oncology*. **2** (2001), pp. 3241-3245.

[147] W.J. Bodell, D.D. Giannini, S. Singh, D. Pietronigro, V.A. Levin, Formation of DNA adducts and tumor growth delay following intratumoral administration of DTI-015, *J Neuro-oncology*. **62** (2003), pp. 251-258.

[148] J. Voges, R. Reszka, A. Gossmann, C. Dittmar, R. Richter, G. Garlip, L. Kracht, H.H. Coenen, V. Sturm, K. Wienhard, W.D. Heiss, A.H. Jacobs, Imaging-guided convection-enhanced delivery and gene therapy of glioblastoma, *Ann. Neurol*. **54** (2003), pp. 479-487.

[149] S.Valtonen, U. Timonen, P. Toivanen, H. Kalimo, L. Kivipelto, O. Heiskanen, G. Unsgaard, T. Kuurne, Interstitial chemotherapy with carmustine-loaded polymers for high-grade gliomas: a randomized double-blind study, *Neurosurgery*. **41** (1997), pp. 44-48.

[150] B.R. Subach, T.F. Witham, D. Kondziolka, L.D. Lunsford, M. Bozik, D. Schiff, Morbidity and survival after 1,3-bis(2-chloroethyl)-1-nitrosourea wafer implantation for recurrent glioblastoma: a retrospective case-matched cohort series, *Neurosurgery*. **45** (1999), pp. 17-22.

[151] M. Westphal, D.C. Hilt, E. Bortey, P. Delavault, R. Olivares, P.C. Warnke, I.R. Whittle, J. Jaaskalainen, Z. Ram, A phase 3 trial of local chemotherapy with biodegradable carmustine (BCNU) wafers (Gliadel wafers) in patients with primary malignant glioma, *Neuro-oncology*. **5** (2003), pp. 79-88.

[152] S.V. Sheleg, E.A. Korotkevich, E.A. Zhavrid, G.V. Muravskaya, A.F. Smeyanovich, Y.G. Shanko, T.L. Yurkshtovich, P.B. Bychkovsky, S.A. Belyaev, Local chemotherapy with cisplatin-depot for glioblastoma multiforme, *J. Neuro-oncol*. **60** (2002), pp. 53-59.

[153] R. Kuroda, F. Akai, H. Iwasaki, J. Nakatani, T. Uchiyama, M. Ioku, I. Kaetsu, Interstitial chemotherapy with biodegradable ACNU pellet for glioblastoma, *Stereotact. Funct. Neurosurg*. **63** (1994), pp. 154-159.

[154] M.S. Lesniak and H. Brem, Targeted therapy for brain tumors, *Nat. Rev.: Drug Discovery*. **3** (2004), pp. 499-508.

[155] C. Guerin, A. Olivi, J.D. Weingart, H.C. Lawson, H. Brem, Recent advances in brain tumor therapy: local intracerebral drug delivery by polymers, *Invest. New Drugs*.**22** (2004), pp. 27-37.

[156] R.J. Tamargo, J.S. Myseros, J.I. Epstein, M.B. Yang, M. Chasin, H. Brem, Interstitial chemotherapy of the 9L gliosrcoma : controlled relsease polymers for drug delivery in the brain, *Cancer Res*. **53** (1993), pp. 329-333.

[157] H. Brem, S. Piantadosi, P.C. Burger, M. Walker, R. Selker, N.A. Bick, K. Black, M. Sisti, S. Brem, G. Mohr, P. Muller, R. Morawetz, S.C. Schold, Placebo controlled trial of safety and efficacy of intraoperative controlled delivery by biodegradable polymers for recurrent gliomas, *Lancet*. **345** (1995), pp. 1008-1012.

[158] Gliadel, Gliadel wafer: Chemotherapeutic implant for certain brain tumors. http://www.gliadel.com (accessed 01 July 2005)

[159] A.B. Fleming and W.M. Saltzman. Pharmacokinetics of the carmustine implant. *Clin Pharmacokinet.* **41**(2002), pp. 403-19.

[160] L.K. Fung, M.G. Ewend, A. Sills, E.P. Sipos, R. Thompson, M. Watts, O,M. Colvin, H. Brem, W.M. Saltzmann, Pharmacokinetics of interstitial delivery of carmustine, 4-hydroperoxycyclophosphamide, and paclitaxel from a biodegradable polymer implant in the monkey brain, *Cancer Res.***58** (1998), pp. 672-684.

[161] A. Olivi, S.A. Grossman, S. Tatter, F. Barker, K. Judy, J. Olsen, J. Bruce, D. Hilt, J. Fisher, S. Piantadosi, Dose escalation of carmustine in surgically implanted polymers in patients with recurrent malignant glioma: a New Approaches to Brain Tumor Therapy CNS Consortium trial, J. Clin. Oncol. 21 (2003), pp. 1845-1849.

[162] J.A. Quinn, J. Pluda, M.E. Dolan, S. Delaney, R. Kaplan, J.N. Rich, A.H. Friedman, D.A. Reardon, J. Sampson, O.M. Colvin, M.M. Haglund, A.E. Pegg, R.C. Moschel, R.E. McLendon, J.M. Provenzale, S. Gururangan, S. Tourt-Uhlig, J.E. Herndon II, D.D. Bigner, H.S. Friedman, Phase II trial of carmustine plus O^6-benzylguanine for patients with nitrosourea-resistant recurrent or progressive malignant glioma, *J. Clin. Oncol.* **20**(2002), pp.2277-2283.

[163] R.L. Schilsky, M.E. Dolan, D. Bertucci, R.B. Ewesuedo, N.J. Vogelzang, S. Mani, L.R. Wilson, M.J. Ratain, Phase I clinical and pharmacological study of O^6-benzylguanine followed by carmustine in patients with advanced cancer, *Clin. Cancer Res.* **6**(2000), pp.3025-3031.

[164] S. Gururangan, L. Cokgor, J.N. Rich, S. Edwards, M.L. Affronti, J.A. Quinn, J.E. Herndon 2nd, J.M. Provenzale, R.E. McLendon, S. Tourt-Uhlig, J.H. Sampson, V. Stafford-Fox, S. Zaknoen, M. Early, A.H. Friedman, H.S. Friedman, Phase I study of Gliadel wafers plus temozolomide in adults with recurrent supratentorial high-grade gliomas, *Neuro-oncol.* **3** (2001), pp. 246-250.

[165] L.R. Kleinberg, J. Weingart, P. Burger, K. Carson, S.A. Grossman, K. Li, A. Olivi, M.D. Wharam, H. Brem, Clinical course and pathologic findings after Gliadel and radiotherapy for newly diagnosed malignant glioma: implications for patient management, *Cancer Invest.***22** (2004), pp. 1-9.

[166] S.E. Lawler, P.P. Peruzzi, E.A. Chiocca, Genetic strategies for brain tumor therapy, *Cancer Gene Ther.* (2005), pp. 1-9 [Epub]

[167] A.B. Brown, W. Yang, N.O. Schmidt, R. Carroll, K.K. Leishear, N.G. Rainov, P.M. Black, X.O. Breakefield, K.S. Aboody, Intravascular delivery of neural stem cell lines to target intracranial and extracranial tumors of neural and non-neural origin, *Hum. Gene Ther.* **14** (2003), pp. 1777-1785.

[168] K.L. von Eckardstein, S. Patt, J. Zhu, L. Zhang, J. Cervos-Navarro, R. Reszka, Short-term neuropathological aspects of in vivo suicide gene transfer to the F98 rat glioblastoma using liposomal and viral vectors, *Histol. Histopathol.* **16** (2001), pp. 735-744.

[169] Y. Zhang, R.J. Boado, W.M. Pardridge, In vivo knockdown of gene expression in brain cancer with intravenous RNAi in adult rats, *J. Gene Med.* **5** (2003), pp. 1039-1045.

[170] R.J. Higgins, M. McKisic, P.J. Dickinson, D.F. Jimenez, S.W. Dow, L.D. Tripp, R.A. LeCouteur, Growth inhibition of an orthotopic glioblastoma in immunocompetent mice by cationic lipid-DNA complexes, *Cancer Immunol. Immunother.* **53** (2004), pp. 338-344.

[171] Y. Zhang, Y.F. Zhang, J. Bryant, A. Charles, R.J. Boado, W.M. Pardridge, Intravenous RNA interference gene therapy targeting the human epidermal growth factor receptor prolongs survival in intracranial brain cancer, *Clin. Cancer Res*. **10** (2004), pp. 3667-3677.

[172] L.X. Zhang, M. Wu, J.S. Jan, Suppresion of audiogenic epileptic seizures by intracerebral injection of a CCK gene vector, *Neuroreport.* **3** (1992), pp. 700-2.

[173] L.L. Zou, L. Huang, R.L. Hayes, C. Black, Y.H. Qiu, J.R. Perez-Polo, W. Le, G.L. Clifton, K. Yang, Liposome-mediated NGF gene transfection following neuronal injury: potential therapeutic applications, *Gene Ther.* **6** (1999), pp. 994-1005.

[174] A. Thorsell, E. Fox, M. Heilig. Lipid mediated gene delivery in the adult rat brain: quantitative analysis of expression. *Neurochem Int.* **35** (1999) 65-71.

[175] J.G. Hecker, L.L. Hall, V.R. Irion, Nonviral gene delivery to the lateral ventricles in rat brain: initial evidence for widespread distribution and expression in the central nervous system, *Mol. Ther.* **3** (2001), pp. 375-384.

[176] Y.J. Cao, T. Shibata, N.G. Rainov, Liposome-mediated transfer of the bcl-2 gene results in neuroprotection after in vivo transient focal cerebral ischemia in an animal model. *Gene Ther.* **9** (2002) 415-419.

[177] K. Yagi, Y. Hayashi, N. Ishida, M. Ohbayashi, N. Ohishi, M. Mizuno, J. Yoshida, Interferon-beta endogenously produced by intratumoral injection of cationic liposome-encapsulated gene: cytocidal effect on glioma transplanted into nude mouse brain, *Biochem. Mol. Biol. Int.* **32** (1994), pp. 167-171.

[178] K. Harada, J. Yoshida, M. Mizuno, K. Kurisu, T. Uozumi, Growth inhibition of intracerebral rat glioma by transfection-induced human interferon-beta, *J. Surg. Oncol.* **59** (1995), pp. 105-109.

[179] M. Mizuno and J. Yoshida, Effect of human interferon beta gene transfer upon human glioma, transplanted into nude mouse brain, involves induced natural killer cells, *Cancer Immunol. Immunother.* **47** (1998), pp. 227-232.

[180] K. Yagi, N. Ohishi, A. Hamada, M. Shamoto, M. Ohbayashi, N. Ishida, A. Nagata, S. Kanazawa, M. Nishikimi, Basic study on gene therapy of human malignant glioma by use of the cationic multilamellar liposome-entrapped human interferon beta gene, *Hum. Gene Ther.* **10** (1999), pp. 1975-1982.

[181] A. Natsume, K. Tsujimura, M. Mizuno, T. Takahashi, J. Yoshida, IFN-beta gene therapy induces systemic antitumor immunity against malignant glioma, *J. Neurooncol.* **47** (2000), pp. 117-124.

[182] M. Mizuno, Y. Ryuke, J. Yoshida, Cationic liposomes conjugation to recombinant adenoviral vectors containing herpes simplex virus thymidine kinase gene followed by ganciclovir treatment reduces viral antigenicity and maintains antitumor activity in mouse experimental glioma models, *Cancer Gene Ther.* **9** (2002), pp. 825-829.

[183] T. Ono, Y. Fujino, T. Tsuchiya, T. Tsuda, Plasmid DNAs directly injected into mouse brain with lipofectin can be incorporated and expressed by brain cells, *Neurosci. Lett.* **117** (1990), pp. 259-263.

[184] B.J. Roessler, B.L. Davidson. Direct plasmid mediated transfection of adult murine brain cells in vivo using cationic liposomes. *Neurosci Lett.* **167** (1994) 5-10.

[185] M. Teresa Girao da Cruz, A.L.C. Cardoso, L.P. de Almeida, S. Simoes, M.C. Pedroso de Lima, Tf-lipoplex-mediated NGF gene transfer to the CNS: neuronal protection and recovery in an excitotoxic model of brain injury, *Gene Therapy*. 2005. 1-11 [Epub].

[186] T. Imaoka, I. Date, T. Ohmoto, T. Yasuda, M. Tsuda M. In vivo gene transfer into the adult mammalian central nervous system by continuous injection of plasmid DNA-cationic liposome complex. *Brain Res.* **780** (1998) 119-128.

[187] P. Leone, C.G. Janson, L. Bilaniuk, Z. Wang, F. Sorgi, L. Huang, R. Matalon, R. Kaul, Z. Zeng, A. Freese, S.W. McPhee, E. Mee, M.J. During, Aspartoacylase gene transfer to the mammalian central nervous system with therapeutic implications for Canavan disease, *Ann. Neurol.* **48** (2000), pp. 27-38.

[188] J. Yoshida, M. Mizuno, M. Fujii, Y. Kajita, N. Nakahara, M. Hatano, R. Saito, M. Nobayashi, T. Wakabayashi, Human gene therapy for malignant gliomas (glioblastoma multiforme and anaplastic astrocytoma) by in vivo transduction with human interferon beta gene using cationic liposomes, *Human Gene Ther.* **15** (2004), pp. 77-86.

[189] A. Jacobs, J. Voges, R. Reszka, M. Lercher, A. Gossmann, L. Kracht, C. Kaestle, R. Wagner, K. Wienhard, W.D. Heiss, Positron-emission tomography of vector-mediated gene expression in gene therapy for gliomas, *Lancet*. **358** (2001), pp. 727-729.

[190] S. Wang, N. Ma, S.J. Gao, H. Yu, K.W. Leong, Transgene Expression in the Brain Stem effected by intramuscular injection of polyethylenimine/DNA complexes. *Mol. Ther*. **3** (2001), pp. 658-664.

[191] D. Goula, J.S. Remy, P. Erbacher, M. Wasowicz, G. Levi, B. Abdallah, B.A. Demeneix, Size, diffusibility and transfection performance of linear PEI/DNA complexes in the mouse central nervous system, *Gene Ther*. **5** (1998), pp. 712-717.

[192] T. Ouatas, S. Le Mevel, B.A. Demeneix, A. de Luze, T3-dependent physiological regulation of transcription in the Xenopus tadpole brain studied by polyethylenimine based in vivo gene transfer, *Int. J. Dev. Biol*. **42** (1998), pp. 1159-1164.

[193] G.P. Tang, J.M. Zeng, S.J. Gao, Y.X. Ma, L. Shi, Y. Li, H.P. Too, S. Wang, Polyethylene glycol modified polyethylenimine for improved CNS gene transfer: effects of PEGylation extent, *Biomaterials*. **24** (2003), pp. 2351-2362.

[194] Y. Li, J. Wang, C.G. Lee, C.Y. Wang, S.J. Gao, G.P. Tang, Y.X. Ma, H. Yu, H.Q. Mao, K.W. Leong, S. Wang, CNS gene transfer mediated by a novel controlled release system based on DNA complexes of degradable polycation PPE-EA: a comparison with polyethylenimine/DNA complexes, *Gene Ther*. **11** (2004), pp. 109-114.

[195] N. Ma, S.S. Wu, Y.X. Ma, X. Wang, J. Zeng, G. Tong, Y. Huang, S. Wang. Nerve growth factor receptor-mediated gene transfer, *Mol. Ther*. **9** (2004), pp. 270-281.

[196] C.K. Goldman, L. Soroceanu, N. Smith, G.Y. Gillespie, W. Shaw, S. Burgess, G. Bilbao, D.T. Curiel, In vitro and in vivo gene delivery mediated by a synthetic polycationic amino polymer, *Nat. Biotechnol*. **15** (1997), pp. 462-466.

[197] O. Boussif, F. Lezoualc'h, M.A. Zanta, M.D. Mergny, D. Scherman, B. Demeneix, J.{. Behr, A versatile vector for gene and oligonucleotide transfer into cells in culture and in vivo: polyethylenimine, *PNAS*. **92** (1995), pp. 7297-7301.

[198] B. Abdallah, A. Hassan, C. Benoist, D. Goula, J.P. Behr, B.A. Demeneix, A powerful nonviral vector for in vivo gene transfer into the adult mammalian brain: polyethylenimine, *Hum Gene Ther*. **7** (1996), pp. 1947-1954.

[199] M.P. Martres, B. Demeneix, N. Hanoun, M. Hamon, B. Giros, Up- and down-expression of the dopamine transporter by plasmid DNA transfer in the rat brain, *Eur. J. Neurosci*. **10** (1998), pp. 3607-3616.

[200] H. Guissouma, N. Becker, I. Seugnet, B.A. Demeneix, Transcriptional repression of TRH promoter function by T3: analysis by in vivo gene transfer, *Biochem. Cell Biol*. **78** (2000), pp. 155-163.

[201] A.C. Hirko, D.D. Buethe, E.M. Meyer, J.A. Hughes, Plasmid delivery in the rat brain, *Biosci. Rep*. **22** (2002), pp. 297-308.

[202] I. Alvarez-Maya, I. Navarro-Quiroga, M.A. Meraz-Rios, J. Aceves, D. Martinez-Fong, In vivo gene transfer to dopamine neurons of rat substantia nigra via the high-affinity neurotensin receptor, *Mol. Med.* **7** (2001), pp. 186-192.

[203] I. Navarro-Quiroga I, J. Antonio Gonzalez-Barrios, F. Barron-Moreno, V. Gonzalez-Bernal, D.B. Martinez-Arguelles, D. Martinez-Fong, Improved neurotensin-vector-mediated gene transfer by the coupling of hemagglutinin HA2 fusogenic peptide and Vp1 SV40 nuclear localization signal, *Brain Res. Mol. Brain Res*. **105** (2002), pp. 86-97.

[204] K. Wu, C.A. Meyers, J.A. Bennett, M.A. King, E.M. Meyer, J.A. Hughes, Polyethylenimine-mediated NGF gene delivery protects transected septal cholinergic neurons, *Brain Res*. **1008** (2004), pp. 284-287.

[205] M. Whitmore, S. Li, L. Huang, LPD lipopolyplex initiates a potent cytokine response and inhibits tumor growth, *Gene Ther*. **6** (1999), pp. 1867-75.

[206] S.W. Dow, L.G. Fradkin, D.H. Liggitt, A.P. Willson, T.D. Heath, T.A. Potter, Lipid-DNA complexes induce potent activation of innate immune responses and antitumor activity when administered intravenously, *J Immunol*. **163** (1999), pp. 1552-61.

[207] K.J. Pulkkannen and S. Yla-Herttuala, Gene therapy for malignant glioma: current clinical status, *Mol. Ther.* Aug 8 (2005), [Epub]

[208] E.A. Neuwelt, E.P. Frenkel, A.N. D'Agnostino, D.N. Carney, J.D. Minna, P.A. Barnett, C.I. McCormick, Growth of human lung tumor in the brain of the nude rat as a model to evaluate antitumor agent delivery across the blood-brain barrier, *Cancer Res.* **45** (1985), pp. 2827-2833.

[209] H.K. Kimelberg, D. Kung, R.E. Watson, F.L. Reiss, S.M. Biddlecome, R.S. Bourke. Direct administration of methotrexate into the central nervous system of primates: part 1, *J. Neurosurg.* **48** (1978), pp. 883-894.

[210] Y. Ushio, T. Hayakawa, H. Mogami, Uptake of tritiated methotrexate by mouse brain tumors after intravenous or intrathecal administration, *J. Neurosurgery.* **40** (1974), pp. 706-716.

[211] D. Nierenberg, R. Harbaugh, L.H. Maurer, T. Reeder, G. Scott, J. Fratkin, E. Newman, Continuous intratumoral infusion of methotrexate for recurrent glioblastoma: a pilot study, *Neurosurgery.* **28** (1991), pp. 752-761.

[212] V.A. Levin, C.S. Patlak, H.D. Landahl, Heuristic modeling of drug delivery to malignant brain tumors, *J. Pharmacokinet. Biopharm.* **8** (1980), pp. 257-296.

[213] C. Nicholson, Diffusion from an injected volume of a substance in brain tissue with arbitrary volume fraction and tortuosity, *Brain Res.* **333** (1985), pp. 325-329.

[214] P.F. Morrison and R.L. Dedrick, Transport of cisplatin in rat brain following microinfusion: an analysis, *J. Pharm. Sci.* **75** (1986), pp. 120-128.

[215] W.M. Saltzman and M.L. Radomsky, Drugs released from polymers: diffusion and elimination in brain tissue, *Chem. Eng. Sci.* **46** (1991), pp. 2429-2444.

[216] C.S. Patlak and J.D. Fenstermacher, Measurements of dog blood-brain transfer constants by ventriculocisternal perfusion, *Am. J. Phys.* **229** (1975), pp. 877-884.

[217] D.E. Clark, In silico prediction of blood-brain barrier permeation, *Drug Disc. Today,* **8** (2003), pp. 927-933.

[218] G.F. Ecker and C.R. Noe, In silico prediction models for blood-brain barrier permeation, *Curr. Med. Chem.* **11**(2004), pp. 1617-1628.

[219] S. Kalyanasundaram, V.D. Calhoun, K.W. Leong, A finite element model for prediciting the distribution of drugs delivered intracranially to the brain, *Am. J. Phys.: Regul. Integr. Comp. Physiol.* **273** (1997), pp. 1810-1821.

[220] W.C. Broaddus, G.T. Gillies, J. Kucharczyk, Minimally invasive procedures: Advances in image-guided delivery of drug and cell therapies into the central nervous system, *Neuroimaging clinics of North America.* **11** (2001), pp. 727-735.

[221] Image Guided Neurologics, IGN. http://www.igneurologics.com (accessed 01 July 2005)

Chapter II: Retro-Convection Enhanced Delivery to increase blood to brain transfer of macromolecules

II.1. Abstract and Introduction

II.1.1. Abstract

A retro-convection enhanced delivery (R-CED) method has been developed to improve the entry of intravenously administered therapeutics within solid brain tumors. R-CED uses an osmotic gradient to withdraw brain interstitial fluid (ISF) in a controlled manner via an implanted microdialysis catheter. Withdrawal of ISF increases the local tissue specific gravity in normal brain and increases two-fold the extravasation of intravenous Evans blue (EB) albumin in normal brain and in an orthotopic 9L tumor. R-CED also increases the extravasation of 70 nm fluorescent liposomes five-fold in the 9L tumor. Thus the transmembrane osmotic gradient induces movement of substances in the blood into the tissue parenchyma. Following probe removal, the magnitude of the R-CED effect on EB-albumin extravasation decreases to control values within 1.5 hrs in normal brain; however, the effect persists beyond six hrs in the tumor. There was no evidence of histologic damage to the neurons at either six hours or two weeks after R-CED. These studies establish the feasibility of applying R-CED to increase the distribution of systemically administered drugs in both the normal tissue-tumor margin as well as in the central tumor core, holding forth the possibility of improved antitumor drug efficacy.

II.1.2. Introduction

Approximately 18,500 new cases of primary malignant brain tumors are

diagnosed in the United States per year [5]. Despite significant advances in tumor imaging, neurosurgery, and radiation therapy, the average one year survival rate has increased little over the past three decades [5]. First-line treatment includes surgery and radiation therapy, which can reduce the typical tumor cell burden of 3-6 x 10^{10} cells by nearly 1000-fold [19]; however, chemotherapy cannot yet reduce the tumor cell number a further 100-fold, a requirement before the immune system can control the tumor burden [19]. Though many potent chemotherapeutic drugs exist, the lack of a drug effect is variously ascribed to factors such as rapid clearance from the brain extracellular space [11], tumor-cell drug resistance [26], high intratumor pressure [6] and poor drug delivery to the brain tumor mass and its peripheral regions [10,29].

The majority of brain tumor chemotherapy drugs delivered by the systemic route have limited efficacy because of poor penetration across the endothelial cell membranes lining the blood vessels that form the blood brain barrier (BBB) [16]. Current efforts to circumvent this problem include osmotic opening of the BBB [27], implantation of drug impregnated depots [13], and direct intracerebral infusion by convection enhanced delivery (CED) [3,6]. CED has shown substantial promise in clinical trials for the delivery of drugs such as paclitaxel [18] and immunotoxins [15], distributing small molecule drugs at a fairly constant drug concentration throughout tissue volumes as large as 600 mm^3 [28]. However, there is a significant variability in the extent of tissue penetration due to factors such as the convective flow rate, catheter diameter, and variations in tissue consistency and interstitial pressure within the tumor [6,30].

Recently, an alternative drug delivery technique has been shown to increase the uptake of systemically delivered chemotherapeutics in peripheral tumors. This method

involves the reduction of tumor pressure to elevate the transendothelial pressure gradient such that the blood pressure drives fluid from the blood vessel into the tissue [8,14]. DiResta and coworkers introduced a needle connected to a vacuum to remove interstitial fluid (ISF) and lower the tumor pressure [8,24]. The reduction in local tumor pressure correlated with increased tumor accumulation of intravenously administered doxorubicin and monoclonal antibodies [7]. However, the vacuum produced in the tissue lacked sufficient control to prevent significant tissue disruption [8,17] and treatment exposure times were limited by difficulties in maintaining a consistently high vacuum within the tissue [7,24].

Retro-convection enhanced delivery (R-CED) improves the rate and consistency of fluid removal by using a polymeric osmolyte to extract fluid from the tissue. This reduces the tissue disruption observed with the vacuum system such that transendothelial pressure reduction is suitable for use in brain tumors. Fluid removal from the tissue is mediated by the magnitude of an osmotic gradient across a semipermeable membrane at the distal end of an implanted commercially available microdialysis catheter (Fig. 1). Fluid pumped through the probe, termed the perfusate, can interact with the brain ISF through the semipermeable membrane; molecules smaller than the membrane's molecular weight cutoff (MWCO) move freely between the tissue and the fluid inside the probe. In contrast, when the perfusate consists of a hyperosmotic solution of an impermeable solute, the transmembrane osmotic pressure gradient induces fluid flow from the tissue space into the probe, where it mixes with the perfusate and is ultimately pumped out of the brain space. Manipulation of the perfusate composition permits direct control over the rate and total magnitude of fluid removal from the brain space with

minimal risk of tissue disruption beyond that typical of probe insertion into the tissue. Removal of interstitial fluid is a distinctive application of microdialysis probes, which are generally used in animal studies and patients to monitor solute concentrations in the interstitial fluid and to deliver drugs in a tissue region by including the drug in the perfusate [2].
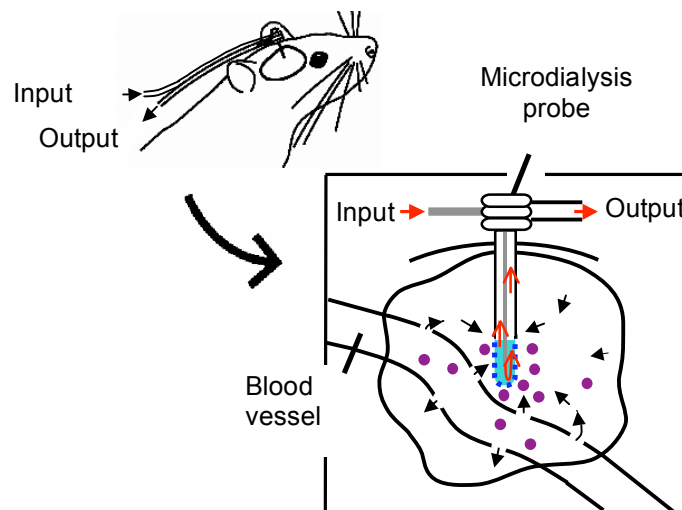
Figure 1. Schematic diagram of R-CED. A. Animals have a microdialysis probe implanted into the brain that is connected to a pump which drives perfusate through the probe. The microdialysis probe consists of two concentric tubes where the perfusate flows (red arrows) through the inner tube (gray) into the space where dialysis occurs (light blue) between the inner tube and the microdialysis membrane (dotted blue line). At this point, the flow direction reverses and exits the system through the outer tube (outlined in black). Fluid flow from the blood into the ISF towards the microdialysis probe is diagrammed with black arrows.

We report that R-CED reliably and safely removes fluid from the brain compartment, increasing the local distribution of systemically delivered Evans blue-albumin (EB-albumin) and liposomes in both normal rat brain and in an intracranial 9L rat tumor. The successful implementation of R-CED demonstrated in this study is indicative of the potential to use R-CED as a tumor drug delivery technique in the brain and in other solid tumors.

II.2. Results

II.2.1. Selection of polymer osmolyte to include in the perfusate fluid

We evaluated the osmolality of dextran, polyethylene glycol (PEG), and polyvinylpyrrlidone (PVP) at varying concentrations (Table 1); these polymers notably exert a higher osmotic pressure than would be predicted simply by their concentration because they have high hydrogen bonding capability and adsorb many layers of water onto the polymer surface. As the osmolality increases, the flow from the brain compartment into the membrane increases, as predicted by the Starling equation; this flow rate begins to plateau at high osmolalities (Fig. 2), possibly because higher osmolality solutions are more significantly opposed by a higher backpressure caused by the increased viscosity of the perfusate. Solutions of the 35 kD PEG were too viscous to pump through the microdialysis probe at concentrations above 6 mM. We selected the 40 kD dextran for use in all subsequent studies.

Table 1. Osmolality of polymer perfusates at various concentrations

Conc. mM	Osmolality mmol/kg			
	PEG 20 kD	PEG 35 kD	PVP 40 kD	Dextran 40kD
2	314	305	317	300
4	328	350	334	309
5	361	365	376	325
6	378	386	388	338
8	428	516	423	375
10	466	692	528	497

Osmolality of aCSF:285 mmol/kg

Fluid removed from the brain compartment
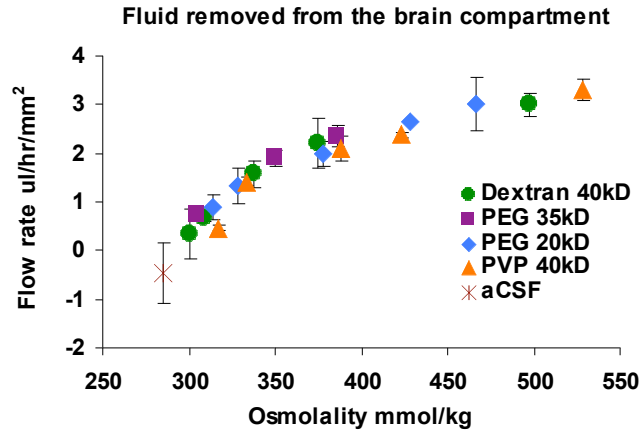
Figure 2. Effect of polymer type and polymer osmolality on flow across the microdialysis membrane from the simulated brain compartment into the microdialysis probe. Flow rate across the microdialysis membrane when the R-CED perfusate is composed of increasing concentrations of dextran (40 kD), polyethylene glycol (PEG, 20 kD and 35 kD), and polyvinylpyrrolidone (PVP, 40 kD). Values are mean $\pm$ SD, n = 3 for each data point.

It is unlikely that dextran in the perfusate leaked out of the microdialysis probe and entered the brain compartment, either *in vitro* or *in vivo*. When a 50 kD fluorescent dextran was included in the perfusate, there was no detectable leakage of fluorescence from the microdialysis membrane into the simulated brain compartment. Inspection of the dialysis membrane after the probe was removed following R-CED *in vivo* showed that the membrane remained intact.

II.2.2. Fluid removal from rat brain

The amount of fluid removed from the brain during one hour of R-CED was dependent on the osmolality of the perfusate used (Table 2). The volume withdrawn in one hour from the simulated brain compartment, composed of aCSF, was 4.3 $\pm$ 1.3 μl (n = 3) and 10.0 $\pm$ 0.8 μl (n = 3) for the 5 and 10 mM dextran perfusate respectively. In the brain, isoosmotic artificial cerebrospinal fluid (aCSF) perfusate solutions did not

withdraw interstitial fluid; a hyperosmotic perfusate of a 5 or 10 mM dextran solution removed 3.2 ± 0.5 µl (n = 5) and 5.8 ± 1.7 µl (n = 15) respectively, which are statistically greater than the average volume removed with an aCSF perfusate. In the orthotopic 9L brain tumor, significantly more fluid can be removed from the tumor than from the normal brain. The amount of fluid withdrawn by the probe *in vivo* is less than the amount of fluid withdrawn from the simulated brain compartment, suggesting that fluid removal is limited by fluid transport in the tissue.

Table 2. Influence of perfusate composition on the volume of fluid removed from the brain during 1 hour of R-CED

	µl of fluid removed from:		
Perfusate	Simulated brain	Normal brain	Tumor brain
aCSF	-1.6 ± 2.0 (3)	-0.5 ± 1.3 (19)	-0.2 ± 0.8 (7)
5 mM 40 kD dextran	4.3 ± 1.3 (3)	$3.2 \pm 0.5^*$ (5)	n.d.
10 mM 40kD dextran	10 ± 0.8 (3)	$5.8 \pm 1.7^*$ (15)	$8.2 \pm 1.3^*$ (11)

Values are mean + SD (n); n.d., not determined
*, $p < 0.001$ compared to aCSF in the same tissue type

II.2.3. Specific gravity measurement

Fluid removal by R-CED increased the local tissue density, as measured using a linear kerosene-bromobenzene gradient. The average specific gravity of caudate putamen samples from the untreated hemisphere was 1.039 ± 0.004 g/cm^3 (n = 26). This value is consistent with Murr and coworkers' measurement of the specific gravity of rabbit caudate putamen samples, which averaged 1.0352 g/cm^3 [21].

When R-CED was used with an isoosmotic aCSF perfusate solution, there was no significant change in the specific gravity of caudate putamen samples. This was significantly different (p = 0.003 and 0.004, respectively) when hyperosmotic solutions

of 5 or 10 mM dextran were used as the R-CED perfusate; in these cases, the increases in specific gravity in the R-CED treated hemisphere were $9.2 \times 10^{-3} \pm 5.0 \times 10^{-3}$ and $7.6 \times 10^{-3} \pm 3.7 \times 10^{-3}$ respectively (n = 5, Fig. 3). There was no significant difference between the specific gravity increases induced by the 5 and 10 mM dextran groups. The 10 mM dextran solution withdrew more fluid but did not further increase the specific gravity compared to the 5 mM dextran solution, implying that the fluid withdrawn from the brain comes from a larger tissue region in the 10 mM dextran case (Table 2). Further specific gravity measurements at time points 1.5 and 6 hrs after R-CED with the 10 mM dextran perfusate showed that the observed increase in specific gravity did not remain significantly different from R-CED with the aCSF perfusate at these later time points (n = 3, Fig. 3).
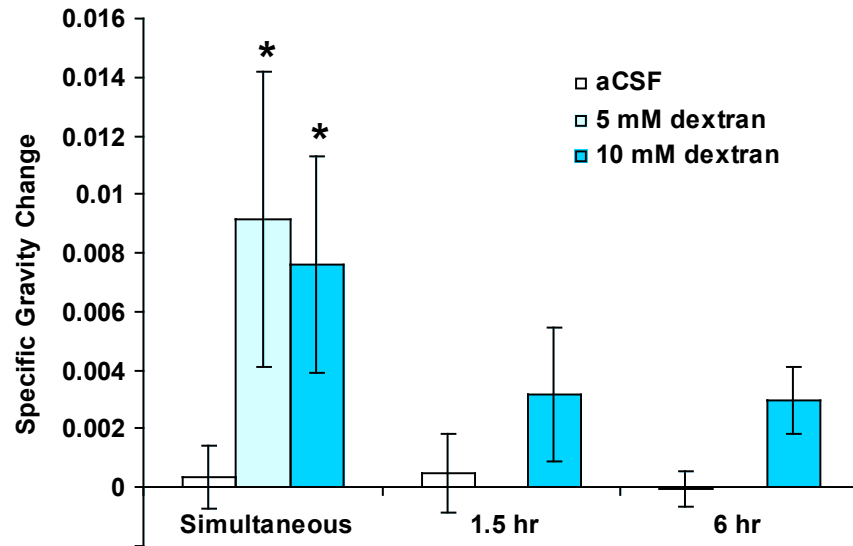
Figure 3. Effect of R-CED on local tissue specific gravity. The specific gravity increases immediately after 1 hr of R-CED with a hyperosmotic 5 or 10 mM dextran perfusate (n = 5) but remains unchanged after R-CED with an isoosmotic aCSF perfusate (n = 4). At later time points after R-CED, no significant difference exists between the groups receiving hyperosmotic or isoosmotic R-CED. Values are mean $\pm$ 95% confidence interval. *, $p < 0.05$ as compared with aCSF group.

II.2.4. Systemic EB-albumin extravasation into normal brain

Application of R-CED increased local extravasation near the microdialysis probe, as visualized by EB-albumin in the brain tissue. The duration of increased EB extravasation after the R-CED probe was removed is depicted in Figure 4. In all cases, R-CED was for one hour and EB exposure was for one hour. EB was injected simultaneously with the start of R-CED (Fig. 4A, B), 1.5 hrs following R-CED (Fig. 4D, E) or 6 hrs following R-CED (Fig. 4G, H). In some cases, animals in the simultaneous group receiving 10 mM dextran R-CED showed percolation of the EB-albumin along the white matter tract (Fig. 4B). However, this did not occur in animals from the other groups.
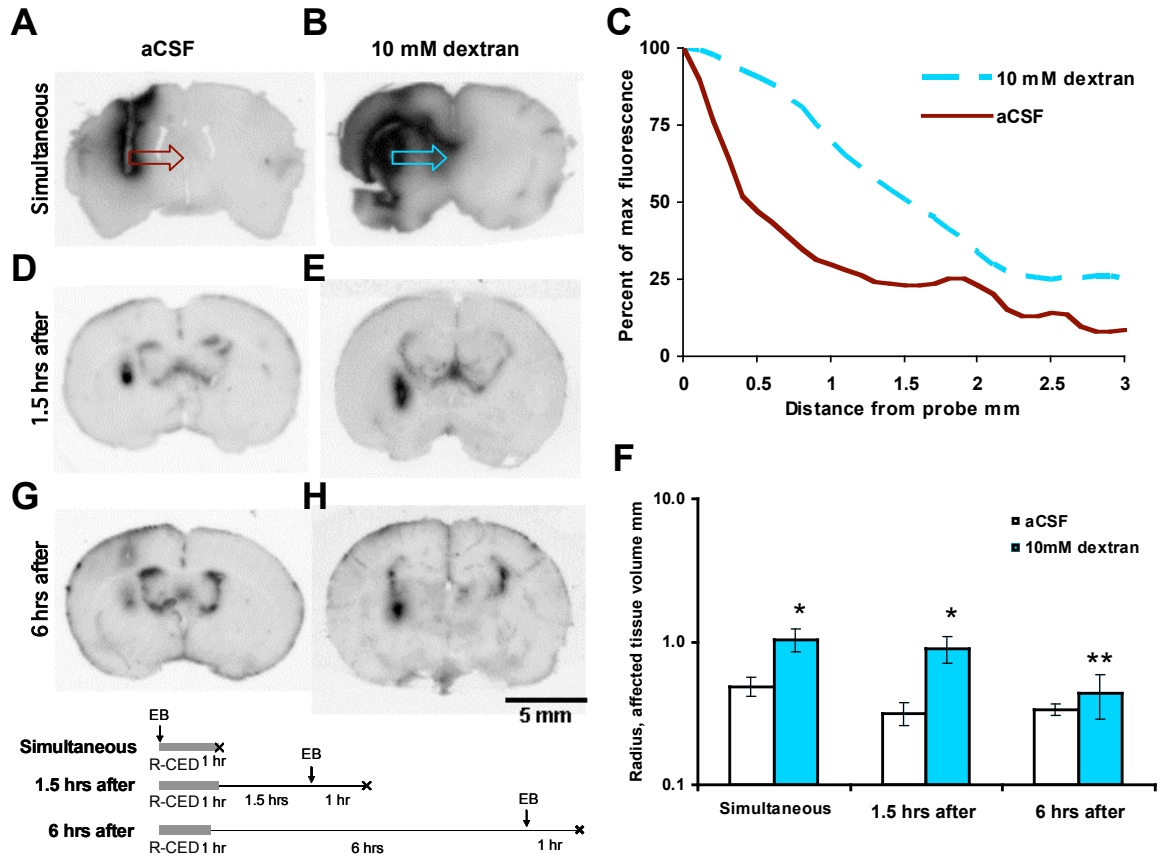
Figure 4. Effect of R-CED on extravasation of EB-albumin in normal brain. A, B, D, E, G, H. The time course of the R-CED effect on EB-albumin extravasation was quantified by injecting EB in the tail vein simultaneous with 1 hr of R-CED (A, B), 1.5 hrs after R-CED probe removal (D, E) or 6 hrs (G, H) after R-CED probe removal. The amount of EB-albumin in the brain increases when the R-CED perfusate consists of hyperosmotic 10 mM dextran (B, E, H) compared to isoosmotic aCSF (A, D, G). C. Average fluorescence profile from the microdialysis probe (in direction of arrows) using representative measurements from each animal for aCSF (solid, n = 3) and 10 mM dextran (dotted, n = 3) for animals where EB-albumin circulated simultaneously with R-CED. F. The log of the radius from the probe to the half maximum fluorescence is dependent on the perfusate type during R-CED. 10 mM dextran (blue) compared to aCSF (white). Values are mean ± SD, n = 3 for all cases; *, $p < 0.05$, as compared with aCSF at the same time point; **, $p < 0.05$, as compared with simultaneous treatment of the same type (either aCSF or 10 mM dextran).

The distribution of EB-albumin in the brain tissue was quantified by determination of the half maximum radius of distribution using profiles from the track of the microdialysis probe such as those shown by the box arrows in Fig. 4A and B. These

69

profiles were standardized by converting the profile to a percentage of the maximum (at the probe insertion point). An average of these standardized profiles is shown in Fig. 4C to visualize how the fluorescence profiles differ when the perfusate consists of hyperosmotic 10 mM dextran or aCSF.

The largest region of local EB-albumin extravasation was observed when EB-albumin circulated in the vasculature simultaneous with R-CED and 1.5 hrs after R-CED. The hyperosmotic perfusate significantly increased (p = 0.01) the radius of distribution to 1.0 ± 0.19 mm, nearly twice the radius observed when an isoosmotic perfusate was used (Fig. 4F, Simultaneous). In both the isoosmotic and hyperosmotic cases, the half maximum radius of EB staining diminished with time after the probe was removed and the animal was allowed to recover. At 1.5 hrs after probe removal, the half maximum radius of EB staining remained significantly larger (p = 0.001) when the hyperosmotic perfusate was used (Fig. 4F). However, 6 hrs after probe removal, the R-CED effect had diminished and no significant difference existed for the half maximum radius of EB staining between the isoosmotic and hyperosmotic groups (Fig. 4F), indicating either that the BBB permeability had returned to a state more similar to normal BBB permeability in the time between 1.5 and 6 hrs following R-CED or the pressure difference between the blood and tissue was eliminated. The duration of the R-CED effect on EB-albumin extravasation persisted longer than did the duration of the change in specific gravity (Fig. 3), where there was no significant difference at the time points 1.5 and 6 hrs after R-CED probe removal. This implies that recovery of the fluid balance in the tissue was faster than the recovery of the BBB to limit protein extravasation into the tissue.
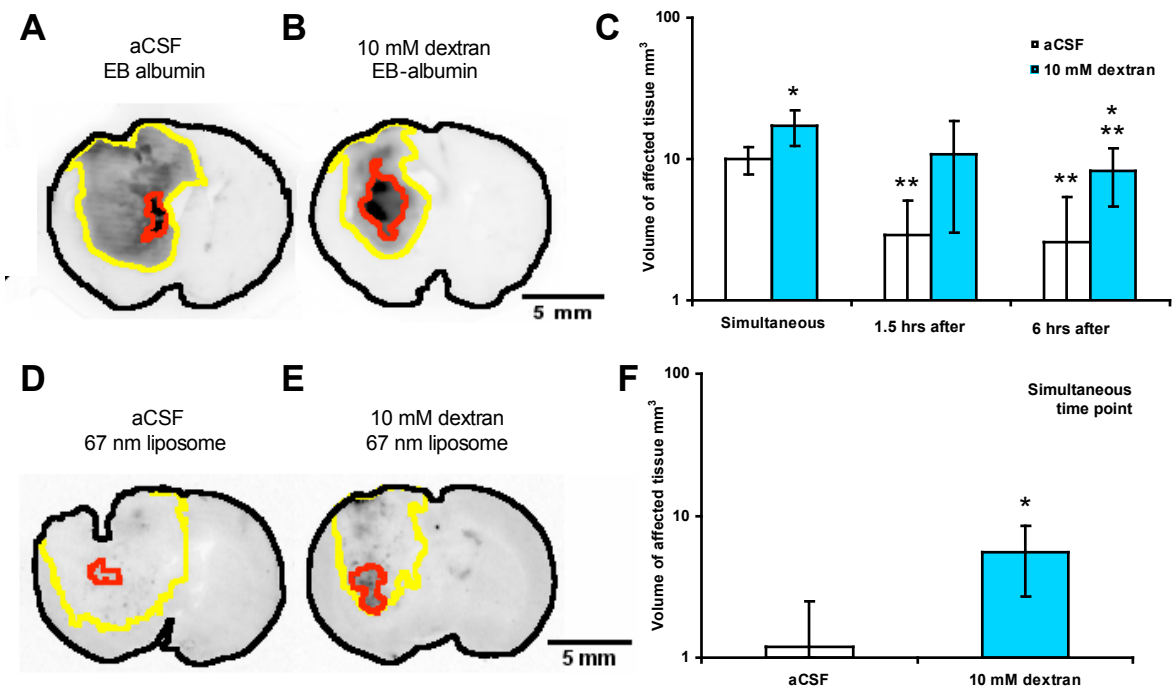
Figure 5. Effect of R-CED on extravasation of EB-albumin and DiD fluorescent liposomes in the intracranial 9L tumor. A, B. The region of half maximal EB-albumin fluorescence (outlined in red) increases after 1 hour of EB-albumin circulation simultaneous with R-CED when the R-CED perfusate is changed from isoosmotic aCSF (A) to hyperosmotic 10 mM dextran (B) solution. C. The half maximal tissue volume of EB-albumin extravasation is a function of R-CED with 10 mM dextran (blue) or aCSF (white) perfusate. Values are mean $\pm$ 95% confidence interval; n = 5: aCSF, 1.5 & 6 hours, 10 mM dextran 6 hours; n = 6 for all other time points. *, $p < 0.05$, as compared with aCSF at the same time point; **, $p < 0.05$, as compared with the simultaneous treatment of the same type (either aCSF or 10 mM dextran). D, E. Low background liposomal fluorescence is observed in the tumor (yellow outline) when no probe is implanted. The region of half maximal fluorescence (outlined in red) is larger when the perfusate is changed from isoosmotic aCSF (D) to hyperosmotic 10 mM dextran (E) when the liposomes circulate simultaneous with R-CED. F. The tissue volume having increased extravasation of the liposomes is significantly greater due to R-CED with 10 mM dextran (n = 5) compared to aCSF (n = 4) perfusate. Values are mean $\pm$ 95% confidence interval; *, $p < 0.05$, as compared with aCSF.

II.2.5. Systemic EB-albumin and 67 nm liposome extravasation into 9L brain tumor

The time course of the R-CED effect on local extravasation of EB-albumin and fluorescent liposomes in the 9L rat glioma model is depicted in Fig. 5. Some EB-albumin extravasation into the tumor was observed in animals when no probe was inserted into the brain, indicating that the 9L tumor blood vessels exhibit an incomplete blood brain barrier. R-CED with the 10 mM dextran perfusate substantially increased the region of EB-albumin extravasation near the microdialysis probe compared with R-CED using aCSF as the perfusate (Fig. 5A, B). Because the needle track could not be identified in all cases, the R-CED effect was quantified using the half maximal volume, measured as the total area over all 1 mm thick brain slices containing the tumor. The largest staining of EB-albumin was observed when EB circulated in the vasculature simultaneous with R-CED and when EB circulated in the vasculature 1.5 hrs after R-CED; this effect was significantly greater for the 10 mM dextran perfusate compared to the aCSF perfusate ($p = 0.03$, Fig. 5C), as was also observed in normal brain (Fig. 4F). The effect remained statistically significant when EB was injected 6 hrs after probe removal ($p = 0.03$, Fig. 5C).

R-CED also affected the extravasation of nanoparticulates such as liposomes in the 9L tumor. Fluorescent liposomes of 67 nm diameter were prepared and injected into the tail vein immediately before one hour of R-CED. These liposomes cannot cross the BBB, as evidenced by the minimal background fluorescence in regions of both normal and tumor brain (Fig. 5D, E). Introduction of the R-CED probe induced a modest region of tissue perturbation where the liposomes were able to enter the parenchymal space of the normal brain. The tissue volume with increased liposome extravasation increased

when R-CED was used with a perfusate consisting of 10 mM dextran compared to aCSF (Fig. 5F). This tissue volume with enhanced liposome extravasation (5.6 ± 2.3 mm^3) was lower than the tissue volume with enhanced extravasation of EB albumin (17 ± 4.8 mm^3) (Fig. 5C, F), indicating that the dimensions of the vascular marker dictate the extent of extravasation into the tissue.

II.2.6. Acute and sub-acute toxicity following R-CED

There were no observable symptoms of neuronal damage in rats exposed to R-CED and maintained for either 6 hrs or 2 weeks, the longest period studied, after probe removal. Histological analysis of H & E sections from R-CED treated animals 6 hrs post treatment revealed no visible neuronal damage beyond that which is known to occur as a result of probe insertion into the brain. The infarcted area was not noticeably larger than that typical of needle insertion into the brain, as visualized by H&E staining 6 hrs and 2 weeks following R-CED (Figure 6). Most importantly, there was no histological difference between animals treated with R-CED using the aCSF perfusate and animals treated with the dextran osmolyte perfusate (Figure 6).
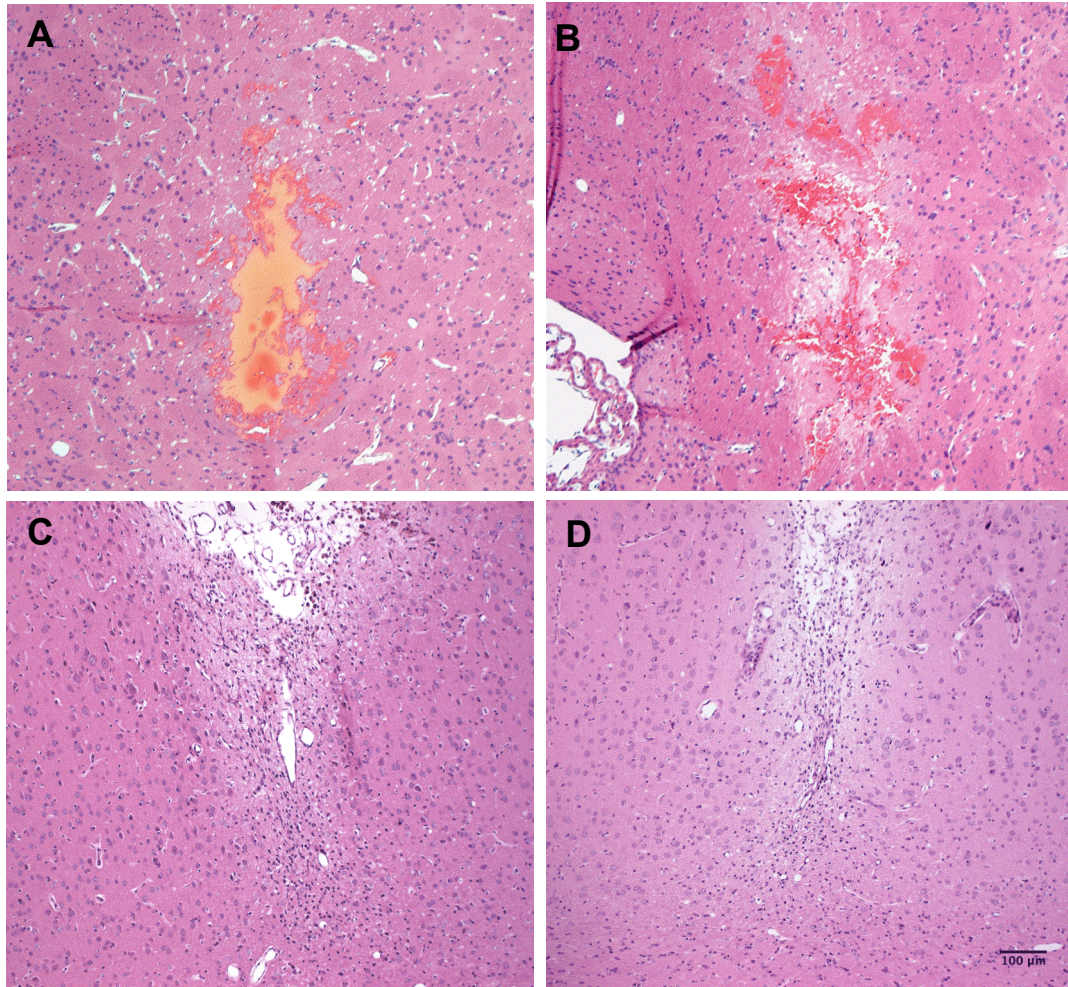
Figure 6. Representative H&E sections of the treated area in the vicinity of the probe 6 hrs and 2 weeks following R-CED treatment show that R-CED treatment results in an infarcted area that is not noticeably larger than that which is typical of needle insertion into the brain. A. aCSF perfusate, 6 hrs after R-CED. B. 10 mM dextran perfusate, 6 hrs after R-CED. C. aCSF perfusate, 2 weeks after R-CED. D. 10 mM dextran perfusate, 2 weeks after R-CED.

II.3. Discussion

We demonstrate that removal of brain interstitial fluid by a hyperosmotic solute via an implanted dialysis probe can increase the extravasation of a vascular marker into both normal brain and an implanted orthotopic brain tumor. DiResta and coworkers have shown that removal of interstitial fluid increases the local extravasation of doxorubicin and molecular antibodies in peripheral tumors (16, 19). R-CED extends this technique to the brain by providing a simple method to reliably and safely control the rate of interstitial fluid removal from the tissue space.

The effect of R-CED was visualized using the fluorescent vascular tracers EB-albumin (6 nm diameter) and DiD liposomes (67 nm diameter). Because these tracers have minimal BBB permeability into normal brain, their visualization in the tissue at distances far from the inserted probe strongly suggests that the BBB permeability has increased at sites distal to the probe location. It is unlikely that these tracers diffuse outwardly from the site of tissue injury caused by probe insertion, because use of the isoosmotic perfusate results in a smaller distribution of vascular tracer within the tissue when compared to use of the hyperosmotic perfusate. Tracer diffusion within the tissue is limited by the short one hour time interval allowed for tracer diffusion, the large size of the vascular tracers, and the high tortuosity of the tissue [22,23]. Further, modeling of the effect of interstitial fluid removal predicts a local convective flow towards the probe, which would significantly inhibit diffusion in the opposite direction [1,8]. For all of these reasons, we believe the fluid extraction from the tissue by the hyperosmotic perfusate increases BBB permeability to vascular markers at locations distal to the R-CED probe.

In the normal brain, R-CED increases extravasation of vascular tracers. Insertion of the R-CED probe without interstitial fluid removal, by circulation of an aCSF perfusate, causes local tissue injury in a region having a half maximum radius of ~0.5 mm surrounding the R-CED probe, as shown in this study and others (Fig. 4A, C; [12]). R-CED with a hyperosmotic solution increases the extravasation and accumulation of these tracers into the brain in a larger tissue volume having a half maximum radius of 1 mm (Fig. 4F). In some cases, R-CED in the normal brain also resulted in percolation of EB-albumin along the white matter tract. Following probe removal, the R-CED effect on EB-albumin extravasation resolves, as evidenced by a decreased region where EB-albumin can enter the brain. In normal brain, the effect of interstitial fluid removal is completely eliminated six hours after R-CED probe removal (Fig. 4F). This time course is paralleled by the time course of the change in specific gravity (Fig. 3), which increases substantially during R-CED but falls to normal levels at time points 1.5 and 6 hrs following R-CED. Taken together, these data suggest that after R-CED, the low permeability of the BBB is recovered. Because the region of EB-extravasation gets smaller at later time points instead of simply accumulating EB-albumin in the tissue, the data suggests that any substances and fluid that have moved from the blood into the tissue are cleared from the brain.

R-CED did not cause any observable acute neurological symptoms for the duration of the experiment following R-CED. Histological tissue sections of the treated area in the vicinity of the probe show no morphological evidence of cytotoxicity and neuronal cell shape appeared normal. The infarcted area is not noticeably larger than that

which is typical of needle insertion into the brain. This suggests that R-CED does not cause acute anatomic damage in the normal brain within 2 weeks of R-CED.

R-CED also increases extravasation of vascular tracers in the 9L rat glioma. Studies using EB-albumin as the vascular marker showed that the maximum effect was observed when the tracer was allowed to circulate simultaneous with R-CED compared to circulation at time points following R-CED probe removal. This process was less complete in the 9L tumor, which showed a persistent, though smaller, R-CED effect six hours after R-CED probe removal. The reduced capacity of the 9L tumor to recover the low permeability of the BBB may be a consequence of the discontinuous and disordered nature of tumor vessels [31], which is also reflected in the larger magnitude of the injury caused by probe insertion compared to that observed in normal brain.

The R-CED effect on the local extravasation of vascular tracers also depends on the size of the vascular tracer; extravasation of liposomes is restricted to a smaller tissue volume compared to the region of EB-albumin. This may be a direct result of the pressure-mediated mechanism by which R-CED makes pathways available for material to extravasate into the tissue. Liposomes, which are an order of magnitude larger than the EB-albumin, require a larger pathway to flow convectively from the blood into the tissue; as such, the tissue region where the transendothelial pressure gradient is high enough to allow liposome extravasation is smaller than the region where EB-albumin can cross the BBB. This is further supported by histological tissue sections which showed little extravasation of red blood cells, which are two orders of magnitude larger than the liposomes.

The radius of the affected tissue for increased liposome entry into the brain is slightly smaller than that shown by CED over a similar treatment time frame. R-CED over one hour extracted 5.8 μl of fluid from the tissue and distributed 67 nm liposomes ~0.61 mm (half maximal radius) away from the R-CED probe. In comparison, a 1-day CED protocol involving an infusion of 200 μl of a similarly sized liposome, resulted in a distribution of ~0.70 to 0.79 mm (half maximal radius) away from the infusion site [20]. Similarly, a one hour R-CED protocol resulted in EB-albumin extravasation within 1.03 mm of the R-CED probe; the 1-day CED protocol distributed a 10 kD dextran 0.97 mm away from the infusion site [20]. Because the R-CED and CED protocols result in a similar drug distribution around the catheter, it is likely that this distribution is highly influenced by the elimination rate of the drug from the tissue.

Other techniques to increase the uptake of systemically administered chemotherapeutic agents into tumors include blood brain barrier disruptors such as hyperosmotic mannitol [27]. These treatments are not tumor selective and can increase fluid and drug uptake into both normal and tumor brain, leading to increased risk of seizures and elevated intracranial pressure [9]. R-CED is more selective for a smaller region of tissue, increasing the influx of drug into the tumor as opposed to normal brain as defined by the position of the microdialysis probe. In addition, R-CED mediated removal of tumor interstitial fluid counteracts the elevated intratumoral pressure, a known barrier to movement of drug from the blood into the tumor [4,14].

These studies establish the feasibility of R-CED to increase extravasation of molecules and nanoparticulates from the vasculature into normal and tumor brain without causing overt toxicity to the normal tissue. It is unlikely that the scale of the effect

observed in our experiments is sufficient to substantially affect the efficacy of intravenously administered BBB-limited anticancer drugs. However, it is easily foreseeable that the R-CED effect can be scaled up by increasing the flux of ISF, achievable by modifications such as increasing the dialysis membrane area, changing the probe geometry, membrane type, polymer type in the perfusate, perfusate flow rate and/or altering the duration of R-CED. It may also be advantageous to design therapies where the isoosmotic and hyperosmotic perfusate solutions can be alternated without removal of the R-CED probe, allowing for long term use of R-CED. Development of these systems is straightforward because microdialysis systems are currently used for monitoring of brain metabolites in patients suffering from a number of brain maladies, including brain tumors [2]. Further, R-CED may be useful in conjunction with therapies such as CED, where fluid is pumped into the tissue directly. Use of R-CED in the vicinity of a CED catheter could alter the pressure gradient in the tissue and enhance convective flow between the two probes, allowing for a patterned distribution of the substance infused by CED. Based on this initial study showing that R-CED can increase local BBB permeability without obvious neuronal toxicity, these modifications to R-CED warrant further investigation.

We have demonstrated that removal of brain interstitial fluid using R-CED is a viable and well-tolerated technique to increase local BBB permeability and enhance the distribution of vascular tracers in both normal brain and in the intracranial 9L glioma. These changes are concurrent with a change in tissue specific gravity associated with fluid removal from the tissue. There are many opportunities to modify R-CED design to scale

up the R-CED affected tissue region, enabling future drug distribution and antitumor

efficacy studies in larger tumors and possibly in humans.

II.4. Materials and methods

II.4.1. R-CED procedure: optimal polymer determination

Polymers (Fluka; Buchs, Switzerland) that were evaluated included dextran,

polyethylene glycol (PEG), and polyvinylpyrrolidone (PVP), of molecular weight greater

than the 20 kD MWCO of the microdialysis membrane. Polymers were dissolved in

artificial cerebrospinal fluid (aCSF: 147 mM NaCl, 2.7 mM KCl, 1.2 mM $CaCl_2$, 0.85

mM $MgCl_2$, osmolality 285 mOsm/kg) at increasing concentrations, which did not alter

the pH. The polymer solution was pumped at 1 μl/min through the microdialysis probe

and positioned in a 0.4 ml solution of aCSF at a temperature of 37°C, a simulated brain

compartment. The volume of water removed from the brain compartment after one hour

of R-CED was measured by weighing the fluid from the R-CED outflow and subtracting

the weight of the perfusate that was pumped through the system. Osmolality was

measured by a vapor pressure osmometer (Wescor; Logan, UT).

II.4.2. Brain tumor implantation

9L rat glioma cells were a generous gift from Dr. Krys Bankiewciz (UCSF Brain

Tumor Research Center, Department of Neurological Surgery). Cells were mycoplasma

free and were maintained and implanted as described by Ozawa et al [25], adhering to the

protocol recommended by the National Institute of Health Guide for the Care and Use of

Laboratory Animals and as approved by the UCSF Institutional Animal Care and Use

Committee. Fischer 344 rats were purchased from Harlan (Indianapolis, Indiana) and Simonsen (Gilroy, California).

II.4.3. R-CED procedure: *in vivo*

Microdialysis probes (CMA/12, 8309562, CMA Microdialysis; North Chelmsford, MA) employed a 20 kDa MWCO polycarbonate membrane with a 0.5 mm diameter and a nominal length of 2 mm. Probes were implanted 5 mm below the top of the skull using the same skull hole that was used for tumor implantation. For experiments involving normal brain, the skull hole was drilled as described for tumor implantation before probe insertion. An external syringe pump (Bioanalytical Systems Inc; West Lafayette, IN) was used to drive the perfusate through the microdialysis probe to the external waste reservoir at 1 μl/min for one hour. In all experiments, the microdialysis outflow, consisting of the fluid pumped through the R-CED probe and the fluid removed from the brain, was collected and weighed to calculate the volume of fluid removed from the brain compartment. After one hour of R-CED, the probe was removed slowly and the animal euthanized. For the tissue specific gravity measurements, animals were euthanized by decapitation immediately following probe removal and the brain immediately frozen at -80°C. In all other experiments, animals were euthanized by perfusion fixation with 350 ml of phosphate-buffered saline (PBS: 100 mM phosphate, 150 mM NaCl, pH 7.4) and 350 ml of 4% paraformaldehyde in PBS. Brains were removed and fixed overnight in 4% paraformaldehyde at room temperature.

II.4.4. Evans blue assay

Evans blue (EB, 4% in saline, 2 ml/kg) was injected into the tail vein. For experiments investigating the duration of the R-CED effect, animals were allowed to recover for a short time following R-CED probe removal. The skull hole was covered with bone cement to prevent reflux, the skin stapled, and animals were given a subcutaneous injection of buprenophine (0.05 mg/kg) to relieve pain. EB was injected simultaneous with the start of R-CED or at time points 1.5 or 6 hours after the R-CED microdialysis probe was removed. One hour after injection of EB, animals were euthanized by perfusion fixation as described above.

II.4.5. Preparation of specific gravity gradient

A linear kerosene-bromobenzene specific gravity gradient was set up using the gravimetric technique of Marmarou (33). All columns had a linear regression correlation coefficient of > 0.99**.** Samples for the column were prepared from frozen 2 mm thick brain slices using a blunt 18G syringe to core out samples 1 mm in diameter from the caudate putamen. All samples were position-matched from the treated and untreated hemispheres to determine the difference in specific gravity between the two hemispheres. The position of samples immersed in the gradient was determined 3 minutes after insertion into the gradient.

II.4.6. Liposome preparation

1,2-Distearoyl-*sn*-Glycero-3-phosphocholine (DSPC), 1,2-Distearoyl-*sn*-Glycero-3-Phosphoethanolamine-N-[Methoxy(Polyethylene glycol)-2000] (PEG-DSPE),

and cholesterol (Chol) were obtained from Avanti Polar Lipids (Alabaster, AL). The fluorescent lipid tracer 1,1'-dioctadecyl-3,3,3',3'-tetramethylindodicarbocyanine perchlorate (DiD, D-307) was purchased from Molecular Probes (Eugene, OR). Liposomes were composed of DSPC/Chol/DSPE-PEG/DiD at a ratio of 55:40:5:0.1 and were prepared by extrusion as described by MacKay et al (28). Particle size was measured using a Malvern (Southborough, MA) Zeta3000 Dynamic Light Scattering Instrument. Liposomes were diluted to 10 μmole/ml of Hepes buffered saline and injected into the tail vein (10 μmole/animal) immediately before the start of R-CED.

II.4.7. Imaging and quantification

Macroscopic images were taken using a flatbed fluorescence scanner (Molecular Dynamics Storm™; Amersham Biosciences; Piscataway, NJ) to visualize the red fluorescence (excitation = 640 nm; emission > 650 nm) of EB-albumin and the lipid tracer DiD. 16-bit images were saved as TIFF files for analysis in Image J (NIH; Bethesda, MD).

Analysis of the R-CED effect in normal brain was done using a variation of the technique used by MacKay et al (28). For the brain section containing the needle track, 4-6 fluorescence profiles 0.5 mm in height were extracted to estimate the half maximum fluorescence radius as a measure of the distance of extravasation from the microdialysis probe. All radii measurements for each animal were averaged together so that one radius was used to characterize each animal in further analysis. In the 9L tumor, background extravasation into the tumor made it difficult to identify the needle track in all cases. Thus, a threshold was applied to quantify a half maximal volume where the intensity fell

to halfway between the maximum signal and the average tumor fluorescence. Average tumor fluorescence was determined by taking the average fluorescence of six samples from the tumor section where no R-CED effect was observed.

Following fluorescence imaging, selected brain tissues were embedded in paraffin, sliced into 5 μm sections and stained with hematoxylin and eosin (H & E). These sections were evaluated by a neuropathologist.

II.4.8. Statistical analysis

Statistical analysis was performed using SPSS version 11.5 (Chicago, IL) to perform a one way ANOVA and these were followed by multiple comparisons using the Tukey t-test to identify significant differences. To normalize the variance between groups, for all EB experiments, ANOVA was performed on the logarithm of the measured values. Additionally, the Kruskal-Wallis test followed by the Mann-Whitney multiple comparisons test were used to identify significant differences in animals bearing the 9L tumor. In no case was the test of homogeneity of variances violated.

II.5. Acknowledgements

II.6. References

[1]   L.T. Baxter and R.K. Jain, 1989. Transport of fluid and macromolecules in tumors. I. Role of interstitial pressure and convection. *Microvasc Res.* **37,** 77-104.

[2]   R.K. Benjamin, F.H. Hochberg, E. Fox, P.M. Bungay, W.F. Elmquist, C.F. Stewart, J.M. Gallo, J.M. Collins, R.P. Pelletier, J.F. de Groot, R.C. Hickner, I. Cavus, S.A. Grossman and O.M. Colvin, 2004. Review of microdialysis in brain tumors, from concept to application: first annual Carolyn Frye-Halloran symposium. *Neuro-oncol.* **6,** 65-74.

[3]   R.H. Bobo, D.W. Laske, A. Akbasak, P.F. Morrison, R.L. Dedrick and E.H. Oldfield, 1994. Convection-enhanced delivery of macromolecules in the brain. *Proc Natl Acad Sci U S A.* **91,** 2076-2080.

[4]   Y. Boucher, H. Salehi, B. Witwer, G.R.t. Harsh and R.K. Jain, 1997. Interstitial fluid pressure in intracranial tumours in patients and in rodents. *Br J Cancer.* **75,** 829-836.

[5]   CBTRUS, Statistical Report: Primary Brain Tumors in the United States, 1998-2002. Central Brain Tumor Registry of the United States, Illinois, 2005.

[6]   M.Y. Chen, R.R. Lonser, P.F. Morrison, L.S. Governale and E.H. Oldfield, 1999. Variables affecting convection-enhanced delivery to the striatum: a systematic examination of rate of infusion, cannula size, infusate concentration, and tissue-cannula sealing time. *J Neurosurg.* **90,** 315-320.

[7]   G.R. DiResta, J. Lee, J.H. Healey, S.M. Larson and E. Arbit, 2000. Enhancing the uptake of chemotherapeutic drugs into tumors using an "artificial lymphatic system". *Ann Biomed Eng.* **28,** 556-564.

[8]   G.R. DiResta, J. Lee, J.H. Healey, A. Levchenko, S.M. Larson and E. Arbit, 2000. "Artificial lymphatic system": a new approach to reduce interstitial hypertension and increase blood flow, pH and pO2 in solid tumors. *Ann Biomed Eng.* **28,** 543-555.

[9]   N.D. Doolittle, A. Petrillo, S. Bell, P. Cummings and S. Eriksen, 1998. Blood-brain barrier disruption for the treatment of malignant brain tumors: The National Program. *J Neurosci Nurs.* **30,** 81-90.

[10]   D.R. Groothuis, H. Benalcazar, C.V. Allen, R.M. Wise, C. Dills, C. Dobrescu, V. Rothholtz and R.M. Levy, 2000. Comparison of cytosine arabinoside delivery to rat brain by intravenous, intrathecal, intraventricular and intraparenchymal routes of administration. *Brain Res.* **856,** 281-290.

[11]   D.R. Groothuis, M.W. Vavra, K.E. Schlageter, E.W. Kang, A.C. Itskovich, S. Hertzler, C.V. Allen and H.L. Lipton, 2006. Efflux of drugs and solutes from brain: the interactive roles of diffusional transcapillary transport, bulk flow and capillary transporters. *J Cereb Blood Flow Metab.*

[12]   D.R. Groothuis, S. Ward, K.E. Schlageter, A.C. Itskovich, S.C. Schwerin, C.V. Allen, C. Dills and R.M. Levy, 1998. Changes in blood-brain barrier permeability associated with insertion of brain cannulas and microdialysis probes. *Brain Res.* **803,** 218-230.

[13] C. Guerin, A. Olivi, J.D. Weingart, H.C. Lawson and H. Brem, 2004. Recent advances in brain tumor therapy: local intracerebral drug delivery by polymers. *Invest New Drugs.* **22,** 27-37.

[14] C.H. Heldin, K. Rubin, K. Pietras and A. Ostman, 2004. High interstitial fluid pressure - an obstacle in cancer therapy. *Nat Rev Cancer.* **4,** 806-813.

[15] S.R. Husain and R.K. Puri, 2003. Interleukin-13 receptor-directed cytotoxin for malignant glioma therapy: from bench to bedside. *J Neurooncol.* **65,** 37-48.

[16] G.H. Huynh, D.F. Deen and F.C. Szoka, Jr., 2006. Barriers to carrier mediated drug and gene delivery to brain tumors. *J Control Release.* **110,** 236-259.

[17] G. Leegsma-Vogt, E. Janle, S.R. Ash, K. Venema and J. Korf, 2003. Utilization of in vivo ultrafiltration in biomedical research and clinical applications. *Life Sci.* **73,** 2005-2018.

[18] Z. Lidar, Y. Mardor, T. Jonas, R. Pfeffer, M. Faibel, D. Nass, M. Hadani and Z. Ram, 2004. Convection-enhanced delivery of paclitaxel for the treatment of recurrent malignant glioma: a phase I/II clinical study. *J Neurosurg.* **100,** 472-479.

[19] K. Lillehei, Immunotherapy. In: M.a.B. Berger, M (Ed.), Neuro-oncology: the essentials, Thieme Medical Publishers, New York, NY, 2000, pp. 264-272.

[20] J.A. MacKay, D.F. Deen and F.C. Szoka, Jr., 2005. Distribution in brain of liposomes after convection enhanced delivery; modulation by particle charge, particle diameter, and presence of steric coating. *Brain Res.* **1035,** 139-153.

[21] R. Murr, S. Berger, L. Schurer, K. Peter and A. Baethmann, 1995. Influence of isoflurane, fentanyl, thiopental, and alpha-chloralose on formation of brain edema resulting from a focal cryogenic lesion. *Anesth Analg.* **80,** 1108-1115.

[22] C. Nicholson and J.M. Phillips, 1981. Ion diffusion modified by tortuosity and volume fraction in the extracellular microenvironment of the rat cerebellum. *J Physiol.* **321,** 225-257.

[23] C. Nicholson and E. Sykova, 1998. Extracellular space structure revealed by diffusion analysis. *Trends Neurosci.* **21,** 207-215.

[24] R. Odland, A.H. Schmidt, B. Hunter, L. Kidder, J.E. Bechtold, B.M. Linzie, R.A. Pedowitz and A.R. Hargens, 2005. Use of tissue ultrafiltration for treatment of compartment syndrome: a pilot study using porcine hindlimbs. *J Orthop Trauma.* **19,** 267-275.

[25] T. Ozawa, G.W. Britz, D.H. Kinder, A.M. Spence, S. VandenBerg, K.R. Lamborn, D.F. Deen and M.S. Berger, 2005. Bromophenol blue staining of tumors in a rat glioma model. *Neurosurgery.* **57,** 1041-1047; discussion 1041-1047.

[26] W.M. Pardridge, 2002. Drug and gene targeting to the brain with molecular Trojan horses. *Nat Rev Drug Discov.* **1,** 131-139.

[27] S.I. Rapoport, 2000. Osmotic opening of the blood-brain barrier: principles, mechanism, and therapeutic applications. *Cell Mol Neurobiol.* **20,** 217-230.

[28] R. Saito, M.T. Krauze, J.R. Bringas, C. Noble, T.R. McKnight, P. Jackson, M.F. Wendland, C. Mamot, D.C. Drummond, D.B. Kirpotin, K. Hong, M.S. Berger, J.W. Park and K.S. Bankiewicz, 2005. Gadolinium-loaded liposomes allow for real-time magnetic resonance imaging of convection-enhanced delivery in the primate brain. *Exp Neurol.* **196,** 381-389.

[29] J.K. Tunggal, D.S. Cowan, H. Shaikh and I.F. Tannock, 1999. Penetration of anticancer drugs through solid tissue: a factor that limits the effectiveness of chemotherapy for solid tumors. *Clin Cancer Res.* **5,** 1583-1586.

[30] M.A. Vogelbaum, 2005. Convection enhanced delivery for the treatment of malignant gliomas: symposium review. *J Neurooncol.* **73,** 57-69.

[31] T. Yamashima, T. Ohnishi, Y. Nakajima, T. Terasaki, M. Tanaka, J. Yamashita, T. Sasaki and A. Tsuji, 1993. Uptake of drugs and expression of P-glycoprotein in the rat 9L glioma. *Exp Brain Res.* **95,** 41-50.

Chapter III: R-CED Mediated Delivery of Liposomal Doxorubicin in the Treatment of the 9L Rat Glioblastoma

III.1. Abstract and Introduction

III.1.1. Abstract

Retro-Convection Enhanced Delivery (R-CED) removes brain interstitial fluid from the region near the probe and increases the extravasation of fluorescent liposomes fivefold in the 9L rat brain tumor. We tested whether this increased extravasation was sufficient to enhance the efficacy of intravenous liposomal doxorubicin chemotherapy. A one hour R-CED treatment applied immediately after intravenous injection of liposomal doxorubicin ten days after tumor implantation showed no therapeutic effect compared to animals treated with intravenous PBS alone. Major factors contributing to this result include the short time of R-CED treatment and the large size of the tumor at the time point treatment was initiated.

III.1.2. Introduction

Particulate drug carriers such as liposomes have been shown to effectively reduce tumor size in animal models, clinical trials and human tumor treatment [1-3]. Compared to free drug, a liposome formulation increases the intravenous half life, decreases systemic toxicity, and increases the drug accumulation within the tumor via the enhanced permeation and retention (EPR) effect. Current liposome drugs that are FDA approved include encapsulated amphotericin B for the treatment of visceral leishmaniasis and encapsulated anthracyclines such as doxorubicin and daunorubicin for recurrent ovarian

cancer and HIV related Kaposi's sarcoma respectively [2]. For neurological disease, intrathecal injection of a cytarabine in a lipid based carrier has been approved for use in lymphomatous meningitis [4].

Liposome drugs have been investigated as a treatment for brain tumors in a number of animal studies and in clinical trials. In the 9L intracranial rat brain tumor, intravenous liposomal doxorubicin, given once a week for three weeks, significantly improved survival from 23.5 to 31.5 days compared to free doxorubicin, which had nearly no effect compared to animals receiving saline injections [5]. However, the increase in lifespan was only observed when treatment was initiated on day 7 and not on day 11. Siegal et al. [6] showed that single dose liposomal doxorubicin (8 mg/kg) given on day 11 improved survival of rats bearing an intracranial T-749 histiocytoma.

To circumvent systemic toxicity due to intravenous delivery of the liposomal doxorubicin, Bankiewicz et al. have also studied convection enhanced delivery of liposomal doxorubicin into rats bearing an intracranial U251 brain tumor, showing 50% of animals with no tumor symptoms following a single CED infusion [7]. Co-infusion of the liposomal doxorubicin with liposomal topotecan in the U87 tumor showed a synergistic effect of the two infused drugs and results in a median survival of the treated group that was greater than 90 days [8]. CED of liposomal drugs can also be imaged by MRI by co-infusion with a liposome containing Gadolinium, permitting *in vivo* monitoring of the infusion distribution[9-13]. Clinical trials of systemic liposomal doxorubicin or brain tumor patients have also shown some efficacy but are limited by systemic toxicity and poor penetration across the blood brain barrier [14-16].

In this study, we investigated whether R-CED would be able to increase the accumulation of liposomal doxorubicin in the intracranial 9L rat brain tumor model. We have shown that R-CED increases five-fold the extravasation of intravenous fluorescent liposomes in this tumor model (Chapter II, [17]). We hypothesized that this increased deposition of the liposomal doxorubicin would lead to an increased therapeutic effect, enabling us to initiate treatment at time points beyond day 7. A one hour R-CED treatment was initiated on day 10, immediately following intravenous administration of the liposomal doxorubicin. We chose to limit the R-CED to a single treatment to limit the number of surgeries tumor bearing animals would experience.

Using this therapeutic protocol, no increase in survival was observed compared to animals receiving PBS control. This experiment suggests several ways in which R-CED and the treatment protocol could be improved to more clearly show the therapeutic efficacy of R-CED against brain tumors. This includes the development of implantable R-CED probes where treatment could be modulated on and off over days to weeks, enabling multiple dosing schedules and potentially increasing the region of R-CED affected tissue. Further, as shown by Straubinger et al. [5], the day of treatment after tumor implantation is a major factor in determining therapeutic effect, and may need to be altered to better visualize the therapeutic capabilities of R-CED.

III.2. Results and Discussion

The therapeutic effect of liposomal doxorubicin on the 9L tumor was investigated by initiating R-CED on day 10 following tumor implantation. Animals received one dose of intravenous PBS (control), or liposomal doxorubicin at a dose of 4 mg/kg. PBS

injected animals received no further treatment. R-CED treatment was initiated

immediately after liposomal doxorubicin injection.

As shown in Figure 1, the median survival for the PBS-treated control group was

21 days. This is typical for animals bearing a 9L intracranial tumor [18,19]. The median

day of death for the R-CED doxorubicin group was day 20.5. The difference in survival

was not significant by the Kaplan-Meier test. These results suggest that the doxorubicin

accumulation in the tumor did not control tumor growth sufficiently to increase the

lifespan of the tumor bearing animals.
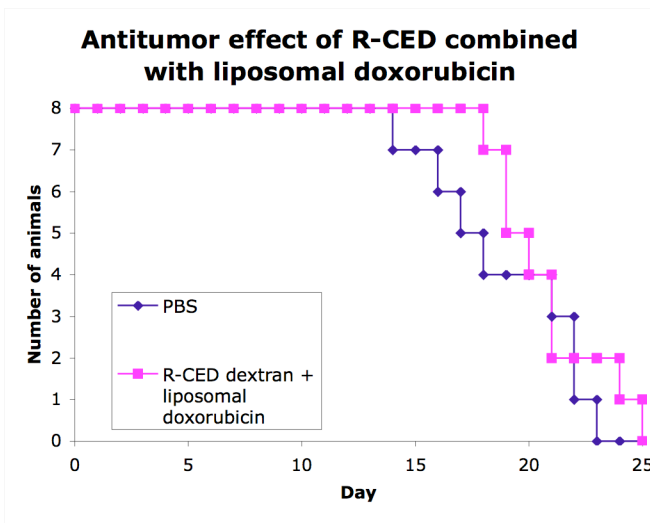
Figure 1. Antitumor effect of R-CED combined with liposome-encapsulated doxorubicin. Rats bearing 9L brain tumors were treated by intravenous injection of liposomal doxorubicin (4 mg/kg) immediately followed by one hour of R-CED. Control animals received PBS injection and no R-CED. Using the Kaplan-Meier test, no significant difference exists between the PBS and R-CED/liposomal doxorubicin treated group.

The antitumor effect is a combined result of many factors, including distribution,

total uptake of the chemotherapeutic, and size of the tumor bulk on the day of treatment.

All of these factors likely contributed to the result we observed in this study.

The tissue region where R-CED increased fluorescent liposome extravasation is

approximately 10 mm^3 (Chapter II). This is approximately 10-20% of the total tumor

volume on day 10 [19]. Treatment of such a small portion of the total tumor cells is

unlikely to result in tumor regression. Further, the R-CED treatment lasted only one hour

and the R-CED effect has been shown to decrease within 6 hours of probe removal (Chapter II); thus, the enhancement of liposome extravasation in the brain occurred for approximately 10% of the 55 hour half life of the liposomal doxorubicin [20]. Knowing that a single administration of liposomal doxorubicin on day 11 is not sufficient to induce 9L tumor regression, the R-CED effect would likely have to be larger than predicted by our fluorescence studies in order for this experiment to result increase in lifespan.

These experiments provide guidance for future studies that will enable R-CED to be therapeutically effective. They show that is important to not only increase the tissue volume affected by R-CED, but also to increase the time that R-CED can be administered such that it is comparable to large vascular half lives of drugs and amenable to multiple dosing schedules. This would be possible with the development of implantable R-CED driven by an implanted pump, where the osmolarity of the perfusate could be externally controlled. Further, probe designs with alternative membrane geometries would also have the potential to form R-CED affected regions having non-spherical geometries. Future studies to measure the therapeutic efficacy of R-CED may also benefit from treatment at a day closer to tumor implantation, when the tumor is smaller. *In vivo* imaging techniques which would enable treatment at specified tumor size, as opposed to a specified day after tumor implantation, which would also help minimize variability in the tumor response to R-CED.

We have completed an initial study into the therapeutic efficacy of R-CED with liposomal doxorubicin. Though no increase in lifespan was observed in this study, our experiment suggests several areas where the current R-CED design can be improved. Changes in R-CED probe design, treatment protocol, and the type and dosing schedule of

the chemotherapeutic will significantly impact the utility of R-CED to enhance the therapeutic effect on systemic chemotherapy delivery to the brain.

III.3. Materials and Methods

III.3.1. Brain tumor implantation

9L rat glioma cells were a generous gift from Dr. Dennis Deen (UCSF Brain Tumor Research Center, Department of Neurological Surgery). Cells were defrosted and passaged 1-3 times before implantation. Cells were mycoplasma free and were maintained and implanted as described by Ozawa et al. [21], adhering to the protocol recommended by the National Institute of Health Guide for the Care and Use of Laboratory Animals and as approved by the UCSF Institutional Animal Care and Use Committee. Fischer 344 rats were purchased from Harlan (Indianapolis, Indiana) and Simonsen (Gilroy, California).

III.3.2. R-CED therapy

Liposomal doxorubicin was purchased from the UCSF Pharmacy and intravenously injected at a concentration of 4 mg/kg. Immediately afterwards, R-CED therapy was started as described in Chapter II [17]. Microdialysis probes (CMA/12, 8309562, CMA Microdialysis; North Chelmsford, MA) employed a 20 kDa MWCO polycarbonate membrane with a 0.5 mm diameter and a nominal length of 2 mm. Probes were implanted 5 mm below the top of the skull using the same skull hole that was used for tumor implantation. An external syringe pump (Bioanalytical Systems Inc; West Lafayette, IN) was used to drive the perfusate through the microdialysis probe to the

external waste reservoir at 1 μl/min for one hour. In all experiments, the microdialysis outflow, consisting of the fluid pumped through the R-CED probe and the fluid removed from the brain, was collected and weighed to calculate the volume of fluid removed from the brain compartment. After one hour of R-CED, the probe was removed slowly, the skull hole covered with bone wax, and the scalp closed with staples. Animals were given subcutaneous buprenorphine to recover. When animals showed neurological signs of increased intracranial pressure due to growth of the tumor, they were euthanized by perfusion fixation with 350 ml of phosphate-buffered saline (PBS: 100 mM phosphate, 150 mM NaCl, pH 7.4) and 350 ml of 4% paraformaldehyde in PBS. Brains were removed and fixed overnight in 4% paraformaldehyde at room temperature.

III.3.3. Statistical analysis

Statistical analysis was performed using SPSS version 11.5 (Chicago, IL) to complete Kaplan-Meier analysis and identify significant differences.

III.4. Acknowledgements

III.5. References

[1]   T.M. Allen and P.R. Cullis, Drug delivery systems: entering the mainstream. *Science.* 303, **(**2004) 1818-1822.

[2]   V.P. Torchilin, Recent advances with liposomes as pharmaceutical carriers. *Nat Rev Drug Discov.* 4, **(**2005) 145-160.

[3]   G.H. Huynh, D.F. Deen and F.C. Szoka, Jr., Barriers to carrier mediated drug and gene delivery to brain tumors. *J Control Release.* 110, **(**2006) 236-259.

[4]   D.J. Murry and S.M. Blaney, Clinical pharmacology of encapsulated sustained-release cytarabine. *Ann Pharmacother.* 34, **(**2000) 1173-1178.

[5]   U.S. Sharma, A. Sharma, R.I. Chau and R.M. Straubinger, Liposome-mediated therapy of intracranial brain tumors in a rat model. *Pharm Res.* 14, **(**1997) 992-998.

[6]   T. Siegal, A. Horowitz and A. Gabizon, Doxorubicin encapsulated in sterically stabilized liposomes for the treatment of a brain tumor model: biodistribution and therapeutic efficacy. *J Neurosurg.* 83, **(**1995) 1029-1037.

[7]   Y. Yamashima, S. R., M.T. Krauze, T. Kawaguchi, C. Noble, D.C. Drummond, D.B. Kirpotin, J.W. Park, M.S. Berger and K. Bankiewicz, Convection-enhanced delivery of liposomal doxorubicin in intracranial brain tumor xenografts. *Targ Oncol.* 1, **(**2006) 79-85.

[8]   Y. Yamashita, M.T. Krauze, T. Kawaguchi, C.O. Noble, D.C. Drummond, J.W. Park and K.S. Bankiewicz, Convection-enhanced delivery of a topoisomerase I inhibitor (nanoliposomal topotecan) and a topoisomerase II inhibitor (pegylated liposomal doxorubicin) in intracranial brain tumor xenografts. *Neuro-oncol.* 9, **(**2007) 20-28.

[9]   R. Saito, M.T. Krauze, J.R. Bringas, C. Noble, T.R. McKnight, P. Jackson, M.F. Wendland, C. Mamot, D.C. Drummond, D.B. Kirpotin, K. Hong, M.S. Berger, J.W. Park and K.S. Bankiewicz, Gadolinium-loaded liposomes allow for real-time magnetic resonance imaging of convection-enhanced delivery in the primate brain. *Exp Neurol.* 196, **(**2005) 381-389.

[10]   R. Saito, J.R. Bringas, T.R. McKnight, M.F. Wendland, C. Mamot, D.C. Drummond, D.B. Kirpotin, J.W. Park, M.S. Berger and K.S. Bankiewicz, Distribution of liposomes into brain and rat brain tumor models by convection-enhanced delivery monitored with magnetic resonance imaging. *Cancer Res.* 64, **(**2004) 2572-2579.

[11]   C. Mamot, J.B. Nguyen, M. Pourdehnad, P. Hadaczek, R. Saito, J.R. Bringas, D.C. Drummond, K. Hong, D.B. Kirpotin, T. McKnight, M.S. Berger, J.W. Park and K.S. Bankiewicz, Extensive distribution of liposomes in rodent brains and brain tumors following convection-enhanced delivery. *J Neurooncol.* 68, **(**2004) 1-9.

[12]   M.T. Krauze, T.R. McKnight, Y. Yamashita, J. Bringas, C.O. Noble, R. Saito, K. Geletneky, J. Forsayeth, M.S. Berger, P. Jackson, J.W. Park and K.S. Bankiewicz, Real-time visualization and characterization of liposomal delivery into the monkey brain by magnetic resonance imaging. *Brain Res Brain Res Protoc.* 16, **(**2005) 20-26.

[13] M.T. Krauze, J. Forsayeth, J.W. Park and K.S. Bankiewicz, Real-time imaging and quantification of brain delivery of liposomes. *Pharm Res.* 23, **(**2006) 2493-2504.

[14] P. Hau, K. Fabel, U. Baumgart, P. Rummele, O. Grauer, A. Bock, C. Dietmaier, W. Dietmaier, J. Dietrich, C. Dudel, F. Hubner, T. Jauch, E. Drechsel, I. Kleiter, C. Wismeth, A. Zellner, A. Brawanski, A. Steinbrecher, J. Marienhagen and U. Bogdahn, Pegylated liposomal doxorubicin-efficacy in patients with recurrent high-grade glioma. *Cancer.* 100, **(**2004) 1199-1207.

[15] K. Fabel, J. Dietrich, P. Hau, C. Wismeth, B. Winner, S. Przywara, A. Steinbrecher, W. Ullrich and U. Bogdahn, Long-term stabilization in patients with malignant glioma after treatment with liposomal doxorubicin. *Cancer.* 92, **(**2001) 1936-1942.

[16] M.I. Koukourakis, S. Koukouraki, I. Fezoulidis, N. Kelekis, G. Kyrias, S. Archimandritis and N. Karkavitsas, High intratumoural accumulation of stealth liposomal doxorubicin (Caelyx) in glioblastomas and in metastatic brain tumours. *Br J Cancer.* 83, **(**2000) 1281-1286.

[17] G.H. Huynh, T. Ozawa, D.F. Deen, T. Tihan and F.C. Szoka, Jr., Retro-convection enhanced delivery to increase blood to brain transfer of macromolecules. *Brain Res.* **(**2006).

[18] M. Weizsaecker, D.F. Deen, M.L. Rosenblum, T. Hoshino, P.H. Gutin and M. Barker, The 9L rat brain tumor: description and application of an animal model. *J Neurol.* 224, **(**1981) 183-192.

[19] T. Ozawa, J. Afzal, K.R. Lamborn, A.W. Bollen, W.F. Bauer, M.S. Koo, S.B. Kahl and D.F. Deen, Toxicity, biodistribution, and convection-enhanced delivery of the boronated porphyrin BOPP in the 9L intracerebral rat glioma model. *Int J Radiat Oncol Biol Phys.* 63, **(**2005) 247-252.

[20] O. Biotech, http://www.doxil.com/pdf/DOXIL_PI_Booklet.pdf. **(**2007).

[21] T. Ozawa, G.W. Britz, D.H. Kinder, A.M. Spence, S. VandenBerg, K.R. Lamborn, D.F. Deen and M.S. Berger, Bromophenol blue staining of tumors in a rat glioma model. *Neurosurgery.* 57, **(**2005) 1041-1047; discussion 1041-1047.

Chapter IV: Predicting Drug Patterning in the Brain following Multi-Probe Convection and Retro-Convection Enhanced Delivery.

IV.1. Abstract and Introduction

IV.1.1. Abstract

Retro-Convection Enhanced Delivery (R-CED) removes brain interstitial fluid via a microdialysis probe and increases the movement of small proteins and particulates from the blood into the tissue. A mathematical model has been developed to predict the size of the R-CED affected region as a function of the rate of fluid removal, the tissue hydraulic conductivity, and the vascular hydraulic permeability. The model confirms the *in vivo* measurement that a larger tissue region is affected in tumor tissue compared with normal tissue. The model predicts a non-spherical flow pattern when there is simultaneous application of two spatially separated infusions or simultaneous application of R-CED and CED from different catheters. The altered flow is most evident when both probes have a comparable fluid flow velocity. The predicted hemispherical distribution pattern of solute flow during the simultaneous infusion of two different florescent tracers in adjacent CED catheters was observed in an agarose gel brain phantom. This analysis provides guidance into how catheter placement affects the penetration of macromolecules in the tissue following R-CED and CED. It also suggests a strategy for the compartmentalization of drugs infused into the brain via one catheter by using a drug-free fluid infusion in a second catheter.

IV.1.2. Introduction

Primary malignant brain tumors continue to be a significant therapeutic challenge despite substantial advances in tumor imaging, neurosurgery, and radiation therapy. The efficacy of potent chemotherapy drugs is limited by biochemical and physiological barriers, including rapid clearance from the brain extracellular space [1], high intratumor pressure [2] and poor drug delivery to the brain tumor mass and its peripheral regions [3-5].

Recently, convection enhanced delivery (CED), a positive pressure infusion directly into the brain, has shown promising results in both animal models and clinical trials [6-8]. CED has been shown to distribute macromolecules, proteins, and particulate therapies into large volumes of tissue [9-11]. In addition to the convective driving force, the transport pathway and distribution are affected by diffusion, uptake and metabolism, and clearance via interstitial and extracellular fluid drainage. These factors result in a deviation from the predicted distribution centered around the infusion catheter, as observed with magnetic resonance imaging [10].

Models of varying complexity, ranging from analytical to finite element models, have been developed to better understand and predict the distribution of material infused by CED [12-17]. In addition, these models have also been used to predict other relevant parameters such as the interstitial fluid pressure, interstitial fluid velocity, tissue swelling, and the transvascular fluid exchange rate during CED.

In this article, we extend these models to predict the distribution of material following Retro-Convection Enhanced Delivery (R-CED) [18], simultaneous application of R-CED and CED and dual probe CED. R-CED is a recently developed drug delivery

technique that removes interstitial fluid to increase the movement of small proteins and

particulates from the blood into the tissue [18-20]. To better understand the parameters

governing the size of the R-CED affected brain region, we used a simplified model based

on the previously established theoretical framework for transvascular/extravascular

transport [12] and high flow microinfusion [16]. The model predictions support our *in

vivo* [18] observations of fluid distribution following R-CED and our *in vitro*

observations of fluid distribution following dual probe CED in an agarose gel brain

phantom. Further, the model provides insight into how multiple CED/R-CED probes

should be positioned to enable spatial drug patterning in the brain.

IV.2. Model

IV.2.1. R-CED alone

   The mathematical model for extravascular transport assumes the tissue to be an

axisymmetric rigid homogenous porous medium, utilizing the equation for continuity of

water and Darcy's law to predict the interstitial fluid velocity, the interstitial pressure and

the solute concentration in the tissue [12,16]. Baxter and Jain [21] included terms for the

diffusive and convective spread of the solute, solute binding to the tissue, and lymphatic

drainage of fluid from the tissue. In our analysis of the size of the R-CED affected region,

we considered a simple best-case scenario, where the initial tissue pressure is 0 mmHg

and both lymphatic drainage and diffusion are neglected. This simplifies the governing

equations for the pressure p and the interstitial fluid velocity u to:

$$\frac{\partial^2 p}{\partial r^2} = \frac{\alpha^2}{R^2}(p - p_e)$$

Eq. 1a

$$u = -k\frac{\partial p}{\partial r}$$

Eq. 1b

where

R = outer radius of tissue

p_e = interstitial pressure yielding zero net volume flux out of the vasculature
(use blood pressure)

$\alpha = R\sqrt{\dfrac{L_p S}{KV}}$ = dimensionless measure of interstitial and vascular resistance to flow

L_p = hydraulic conductivity of the vascular wall

S/V = surface area per unit volume for transvascular transport

k = hydraulic conductivity of the interstitial space

These two equations form the foundation for the model of fluid transport. Eq. 1a shows that the Laplacian of the pressure is related to the tissue pressure modulated by the interstitial and vascular hydraulic conductivity for fluid flow. Eq. 1b, Darcy's law, shows that the fluid velocity is directly related to the pressure gradient through the hydraulic conductivity of the interstitial space.

In the case of R-CED, Eq. 1a and 1b can be solved using the following 2 boundary conditions:

1. the pressure far from the R-CED probe is p_∞

$$p_i\big|_{r=R} = p_\infty$$

Eq. 2a

2. the R-CED fluid removal rate at the catheter radius, R_p is q

$$u\big|_{r=R_p} = -k\frac{\partial p}{\partial r}\bigg|_{r=R_p} = q$$

Eq. 2b

Using these 2 boundary conditions, Eq. 1a can be solved to give

$$p_i = c_1 \frac{1}{r} \cosh\left(\frac{\alpha r}{R}\right) + c_2 \frac{1}{r} \sinh\left(\frac{\alpha r}{R}\right) + p_e \qquad\qquad \text{Eq. 3a}$$

$$u = -k\left(c_1 \frac{1}{r}\frac{\alpha}{R} \sinh\left(\frac{\alpha r}{R}\right) + c_2 \frac{1}{r}\frac{\alpha}{R} \cosh\left(\frac{\alpha r}{R}\right)\right) \qquad\qquad \text{Eq. 3b}$$

where

$$c_1 = \frac{R(p_\infty - p_e) - c_2 \sinh(\alpha)}{\cosh(\alpha)}$$

$$c_2 = \frac{-\dfrac{R_m^2 u_m}{k} - \dfrac{R(p_\infty - p_e)}{\cosh(\alpha)}\left(\alpha \dfrac{R_m}{R}\sinh\left(\dfrac{\alpha R_m}{R}\right) - \cosh\left(\dfrac{\alpha R_m}{R}\right)\right)}{\dfrac{\alpha R_m}{R}\cosh\left(\dfrac{\alpha R_m}{R}\right) - \sinh\left(\dfrac{\alpha R_m}{R}\right) - \dfrac{\alpha R_m \sinh(\alpha)}{R\cosh(\alpha)}\sinh\left(\dfrac{\alpha R_m}{R}\right) + \dfrac{\sinh(\alpha)}{\cosh(\alpha)}\cosh\left(\dfrac{\alpha R_m}{R}\right)}$$

Parameter values, detailed in Table 1, were selected based on literature values for normal brain and tumor tissue. The third column lists the animal species the value was measured in, as described in the reference listed in the right column. Compared to the normal brain, the tumor has a higher interstitial pressure, increased hydraulic permeability across the endothelial wall and lower hydraulic conductivity through the interstitium.

These measured values can vary depending on tissue deformation, perfusion method, and measurement technique [22]. Though it is generally established that the U87 tumor has a higher hydraulic conductivity across the blood vessel wall, it remains unclear whether the tumor interstitial hydraulic conductivity should be higher or lower than normal tissue. The hydraulic conductivity depends on a number of factors including the extracellular space volume fraction, cell size and shape, makeup and organization of the extracellular matrix proteins, and the tortuosity of the interstitial space; all of these factors can be altered in a tumor tissue. Measurements comparing the interstitial hydraulic conductivity in multiple tumors and normal tissue have not consistently shown

the tumor hydraulic conductivity to be higher or lower than the normal tissue [23,24]. In

our case, we have selected values for the U87 tumor and normal brain primarily from

theory and measurements in mice.

Table 1.
Parameter values used in model predictions for R-CED

Parameter		Animal species		Ref
L_p	Hydraulic conductivity across bv wall, normal	Human brain	9.5×10^{-10} cm/mmHg-sec	[16]
	Hydraulic conductivity across bv wall, tumor	SCID mouse U87 tumor i.c.	1.11×10^{-7} cm/mmHg-sec	[25]
K	Hydraulic conductivity through interstitium, normal	Human brain (theory)	6.7×10^{-6} cm^2/mmHg-sec	[14]
	Hydraulic conductivity through interstitium, tumor	Athymic mouse U87 tumor s.c.	6.5×10^{-7} cm^2/mmHg-sec	[23]
S/V	Ratio of vessel surface area to volume, normal & tumor	SCID mouse	250 cm^{-1}	[26]
p_e	Interstitial pressure yielding zero net flux out of the vasculature, normal	Theory only	0 mm Hg	[12]
	Interstitial pressure yielding zero net flux out of the vasculature	SCID mouse U87 tumor s.c.	9.5 mm Hg	[27]
A	Catheter membrane area	Probe parameter	$\pi \times 10^{-2}$ cm^2	
R_m	Catheter radius, R-CED	Probe parameter	0.0325 cm	

b.v. blood vessel
i.c. intracranial
s.c. subcutaneous

IV.2.2. Multi-probe drug patterning

To predict multi-probe drug patterning, the simple best case scenario assumes the

brain as a homogeneous porous medium where radial bulk interstitial flow is driven by

the CED and R-CED probes in accordance with Darcy's law, as used in our model for

R-CED alone and described by Morrison et al [16]. To further simplify the model, we

assume no fluid exchanges across the endothelial wall, so that none of the CED infused

fluid is lost into the blood vessels or to lymphatic drainage. We will consider that the

only difference between R-CED and CED is the sign of the infusion flow rate; thus, all of the fluid removed by R-CED comes from the interstitial space, and none comes from the vasculature. Though this seems counterintuitive to the goal of R-CED, we selected this simplifying assumption to visualize the maximum interaction between the CED and R-CED driven fluid flow. These simplifying assumptions were applied to the equations described by Morrison et al [16] for a high flow microinfusion using the initial conditions he described:

　　　1. the pressure gradient far from the probe is zero

$$\left.\frac{\partial p}{\partial r}\right|_{r=\infty} = 0 \qquad\qquad\qquad \text{Eq. 5a}$$

　　　2. the bulk flow in the tissue is equal to the infusion rate q

$$q = 4\pi r^2 \phi u \qquad\qquad\qquad\qquad \text{Eq. 5b}$$
where
$\phi = \text{Extracellular space fraction}$

Thus, the velocity can be determined by rearranging Eq. 5b. In combination with Eq. 1b, the equation for pressure is also easily defined:

$$p = \frac{q}{4\pi\phi kr} \qquad\qquad\qquad\qquad \text{Eq. 6a}$$

$$u = \frac{q}{4\pi\phi r^2} \qquad\qquad\qquad\qquad \text{Eq. 6b}$$

For the model, it was assumed that the effect on pressure and subsequently fluid flow velocity caused by R-CED and CED are additive when calculating the cumulative effect.

　　　The complete set of parameter values are detailed in Table 2. Parameter values primarily remained the same as detailed in Table 1. Some variables, such as L_p, have different values because the simplifying assumptions are different. As in Table 1, the

third column lists the species the value was measured in, as described in the reference

listed in the right column.

Table 2.
Parameter values used in model predictions for multi-probe calculations

Parameter		Animal species		Ref
L_p	Hydraulic conductivity across b.v. wall	By assumption	0	[16]
K	Hydraulic conductivity through interstitium, normal	Human brain (theory)	6.7×10^{-6} cm^2/mmHg-sec	[14]
	Hydraulic conductivity through interstitium, tumor	Athymic mouse U87 tumor s.c.	6.5×10^{-7} cm^2/mmHg-sec	[23]
S/V	Ratio of vessel surface area to volume, normal and tumor	SCID mouse	250 cm^{-1}	[26]
ϕ	ECS fraction	Rat cerebellum	0.2	[28]
p_e	Interstitial pressure yielding zero net flux out of the vasculature, normal	Theory only	0 mm Hg	[12]
	Interstitial pressure yielding zero net flux out of the vasculature	SCID mouse U87 tumor s.c.	9.5 mm Hg	[27]
A	Catheter membrane area	Probe parameter	$\pi \times 10^{-2}$ cm^2	
R_m	Catheter radius, CED	Probe parameter	0.0025 cm	
R_m	Catheter radius, R-CED	Probe parameter	0.0325 cm	

b.v. blood vessel
s.c. subcutaneous

IV.3. Materials and methods

IV.3.1. Computer simulation

All calculations were done in Matlab v.6 Release 12, running on a Windows virtual

machine from a MacBook, using the code attached in Appendix A.

IV.3.2. R-CED procedure: *in vitro*

R-CED was completed following the protocol described by Huynh et al. [18].

Briefly, microdialysis probes (CMA/12, 8309562, CMA Microdialysis; North

Chelmsford, MA) employed a 20 kDa molecular weight cutoff polycarbonate membrane

with a 0.5 mm diameter and a nominal length of 2 mm. Probes were inserted into a 0.5%

agarose gel, prepared immediately before use, approximately 8 mm below the surface of

the agarose. An external syringe pump (Bioanalytical Systems Inc; West Lafayette, IN)

was used to drive the perfusate, a 10 mM 40kD dextran, through the microdialysis probe

to the external waste reservoir at 1 μl/min for one hour. The microdialysis outflow,

consisting of the fluid pumped through the R-CED probe and the fluid removed from the

agarose phantom, was collected and weighed to calculate the volume of fluid removed

from the agarose phantom. After one hour of R-CED, the probe was removed slowly

over 1 minute.

IV.3.3. CED procedure: *in vitro*

CED was completed as described for an acute stereotactic infusion [9,29,30]. Briefly, a

narrow cannula was prepared from fused silica tubing with an outer diameter of 0.16 mm

(Polymicro Technologies, Phoenix, AZ), extending 1-2 mm from the tip of a 24 gauge

needle used for support [31]. This cannula was inserted into the 0.5% agarose gel,

prepared immediately before use, approximately 8 mm below the surface of the gel. An

external syringe pump (Bioanalytical Systems Inc; West Lafayette, IN) was used to drive

the infusion at an increasing flow rate as follows: 0.1 μL /min for 5 min, 0.2 μL /min for

5 min, 0.5 μL /min for 5 min, and 0.8 μL /min for 30 min for a total volume of 28 μL

infused over 45 min. Following the infusion, the probe was removed slowly over 1

minute. In the case of simultaneous R-CED and CED, trypan blue was infused.

Photographs were taken using a Sony CyberShot DSC-P50. In the case of simultaneous

CED infusion, either albumin-Alexa Fluor 647 or Texas Red-dextran was infused.

Photographs were taken by slicing the agarose phantom and imaging on a Kodak Imagestation 4000. The Alexa Fluor 647 was visualized using the 625 nm excitation filter and the 700 nm emission filter. Texas Red was visualized using the 535 nm excitation filter and the 600 nm emission filter.

IV.4. Results

IV.4.1. R-CED alone

Using the parameter values in Table 1 with Eq. 1-3, we can predict the steady state interstitial pressure, interstitial velocity, and transendothelial velocity from the blood into the tissue following R-CED in normal and tumor brain. Figure 1A-C shows that the region where pressure is decreased due to R-CED is primarily within 0.5 mm of the probe. A cutoff pressure threshold of 3 mmHg was selected based on other studies correlating changes in vascular permeability with changes in tumor pressure as small as 3 mmHg [32]. Using this pressure cutoff, the affected region in the tumor compared to normal tissue is approximately 3.5 times larger in radius. For comparison, our *in vivo* data [18] shows that the increase in radius from normal to tumor brain for EB-albumin movement into the tissue is about 1.7 (1 mm radius, normal compared to 1.6 mm radius, tumor [17 mm^3 volume]). A possible reason why our *in vivo* data shows a smaller increase could be because it includes a higher background level caused by introduction of the probe into the tissue [33].
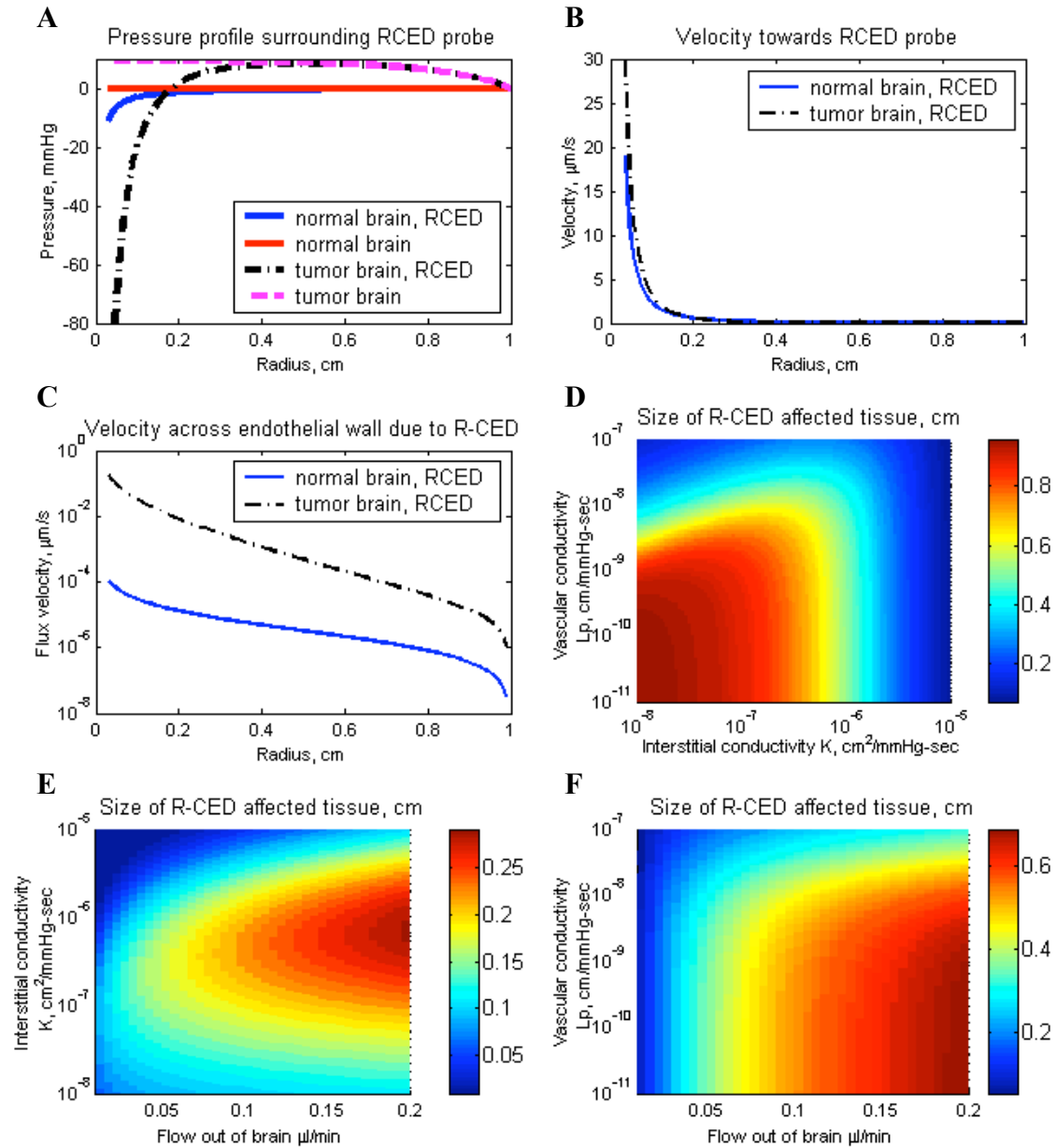
Figure 1. Computed distribution pattern of interstitial pressure, interstitial velocity, velocity across the endothelial wall, and the size of the R-CED effect. A-C. Using the parameters in Table 1 and 2, the pressure, interstitial velocity, and velocity across the endothelial wall in normal brain and tumor brain. D-F. The size of the R-CED affected tissue depends on the rate of fluid removal, interstitial (K) and vascular (L_p) hydraulic conductivity.

As shown in Figure 1A-C, R-CED induces a larger negative pressure and affects a larger tissue region in the tumor compared to normal brain. This is principally because the tumor has a lower interstitial hydraulic conductivity and a greater amount of fluid is removed from the tumor.

The main determining factors that contribute to the size of the affected region are the interstitial and vascular resistance to flow. These parameters may vary significantly among tissue types, pathological tissues, and are likely to be anisotropic and change with time. Measurements that can estimate accurately the correct order of magnitude of these parameters will substantially contribute to better model predictions of the drug distribution following R-CED.

Figure 1D-F shows how the size of the affected region depends on the rate of fluid removal from the brain, the hydraulic conductivity across the blood vessel wall L_p, and the hydraulic conductivity through the interstitium, K. As shown in Figure 1D, there is an optimal combination of the vascular hydraulic permeability and the interstitial hydraulic conductivity which maximizes the radius of the affected tissue region. At interstitial hydraulic conductivities typical of that seen in the U87 tumor tissue (~10^{-7} cm^2/mmHg-sec [25]), a vascular hydraulic permeability on the order of 10^{-9} cm/mmHg-sec increases the radius of the R-CED affected region to nearly 1 cm. At a given interstitial hydraulic conductivity, a very high vascular hydraulic permeability allows for all of the R-CED removed fluid to come from local vascular sources, limiting the influenced tissue region; conversely, a very low vascular hydraulic permeability forces all removed fluid to come from a large region of interstitial space, but the region having a pressure difference > 3 mmHg is decreased. These predictions indicate that R-CED may

be more useful in combination with therapies that can modulate the vascular and interstitial hydraulic conductivities, such as infusion of matrix degrading enzymes [34-36] or angiogenic modulators [37,38].

IV.4.2. Multi-probe drug patterning: simultaneous R-CED and CED

By combining R-CED and CED, it is possible to increase the fluid velocity between the probes if the fluid flow rate pumped in by CED and removed by R-CED are comparable (Figure 2). The probes must be sufficiently close to each other that they have a non-zero effect on the fluid velocity in the tissue space between the probes. Given that our current fluid removal rate by R-CED is 10 μl/hr (~0.17 μl/min) *in vitro*, it is necessary to compare this to a CED infusion rate of 0.2 μl/min.
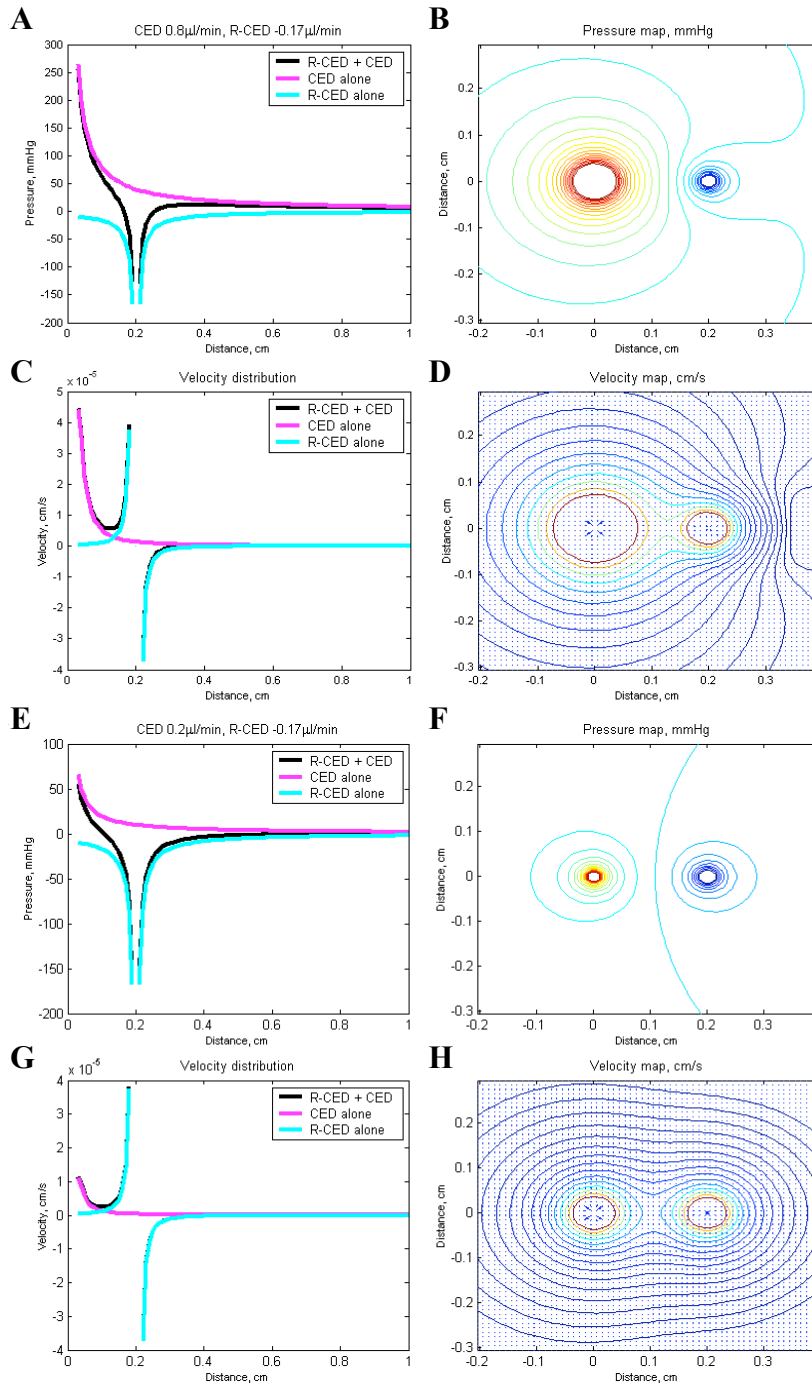
Figure 2. The steady state velocity and pressure distribution during combination CED and R-CED. The CED probe is centered at (0,0) and the R-CED probe at (0.3, 0). A-D. Velocity and pressure distribution following CED infusion at 0.2 μl/min and R-CED fluid removal at 0.17 μl/min. E-H. Velocity and pressure distribution following CED infusion at 0.8 μl/min and R-CED fluid removal at 0.17 μl/min. In D and H, the velocity map, the arrow size represents the relative magnitude of the velocity and the arrow points in the direction of the velocity vector. Curves represent decreasing speed from red to blue. In A, B, D, E, CED only (pink), R-CED only (blue) and combination R-CED and CED (black).
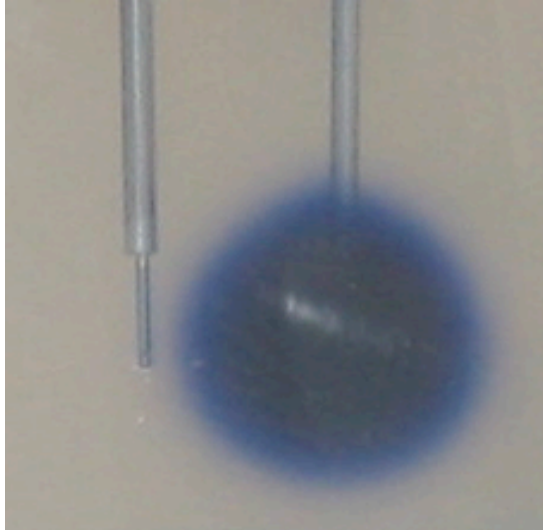
Figure 3. *In vitro* example of combination R-CED (left probe) and CED (right probe) during CED infusion of 0.4% trypan blue into a 0.5% agarose gel. Probes were situated 3 mm apart. After a 45 min step up infusion where the maximum CED infusion rate is 0.8 μl/min, the trypan blue has distributed approximately spherically from the CED probe.

We tested this hypothesis in a 0.5% agarose gel brain phantom, which Bankiewicz and colleagues [31] also used to visualize the CED fluid distribution. In this case, the probes are 3 mm apart, the closest that it was technically possible to position the probes accurately. Trypan blue is infused by CED at an increasing rate that stabilizes at 0.8 μl/min, a rate that ensures the CED probe will substantially influence the tissue pressure and fluid velocity in the region between the two probes. R-CED removed interstitial fluid at a rate of 0.17 μl/min, a rate that has been tested previously in animal experiments. In our experimental case, the effect of the R-CED probe on the CED distribution profile is not easily visualized (Figure 3); it is apparent that the combination effect is small given the 3 mm separation distance.

The limited interaction between the two probes is partly caused by the slow rate of fluid withdrawal compared to the faster rate of infusion; as described before, higher fluid removal rates increase the R-CED affected region. Further, the hydraulic conductivity of the 0.5% agarose gel brain phantom, $\sim 9.8 \times 10^{-5}$ cm^2/mmHg-sec [39], is higher than that observed in normal or tumor tissue; in a system where the matrix water constitutes over 99% of the volume, a high matrix hydraulic conductivity does not favor

large negative pressures or large pressure gradients, further reducing the size of the region influenced by R-CED or CED. The effect in the overlapping region can be increased by maximizing the size of the region affected individually by R-CED and CED, using techniques described above.

IV.4.3. Multi-probe drug patterning: simultaneous CED infusion via two probes

Multi-probe CED has previously been described as a means to achieve a larger drug distribution within the brain [40]. To minimize the number of skull holes required, catheters have been designed whereby multiple CED probes could be deployed to various brain regions via a single central catheter [40].

Figure 4A-B shows the model prediction that multi-probe CED results in isolation of each infusion if the probes are positioned such that their predicted single probe radii of distribution overlap. This occurs because there is a point on the line directly connecting the two probes where the velocity from each probe is equal in magnitude but opposite in direction, resulting in zero net velocity. By this same reasoning, a surface exists between the two probes where the velocity towards the other probe cancels out, but a net velocity remains in the perpendicular direction. Thus, no convection mediated overlap exists between the infused material from the two probes (Figure 4A-B). This was confirmed in an agarose phantom, where the probes are situated 2 mm apart.

In Figure 4C-E,the left CED probe infuses albumin-Alexa Fluor 647 while the right CED probe infuses Texas Red-dextran. The close positioning of the two probes during the simultaneous CED results in a hemispherical distribution of each fluorophore (Figure 4C-D), as predicted by the model (Figure 4B). Further, the composite fluorescent
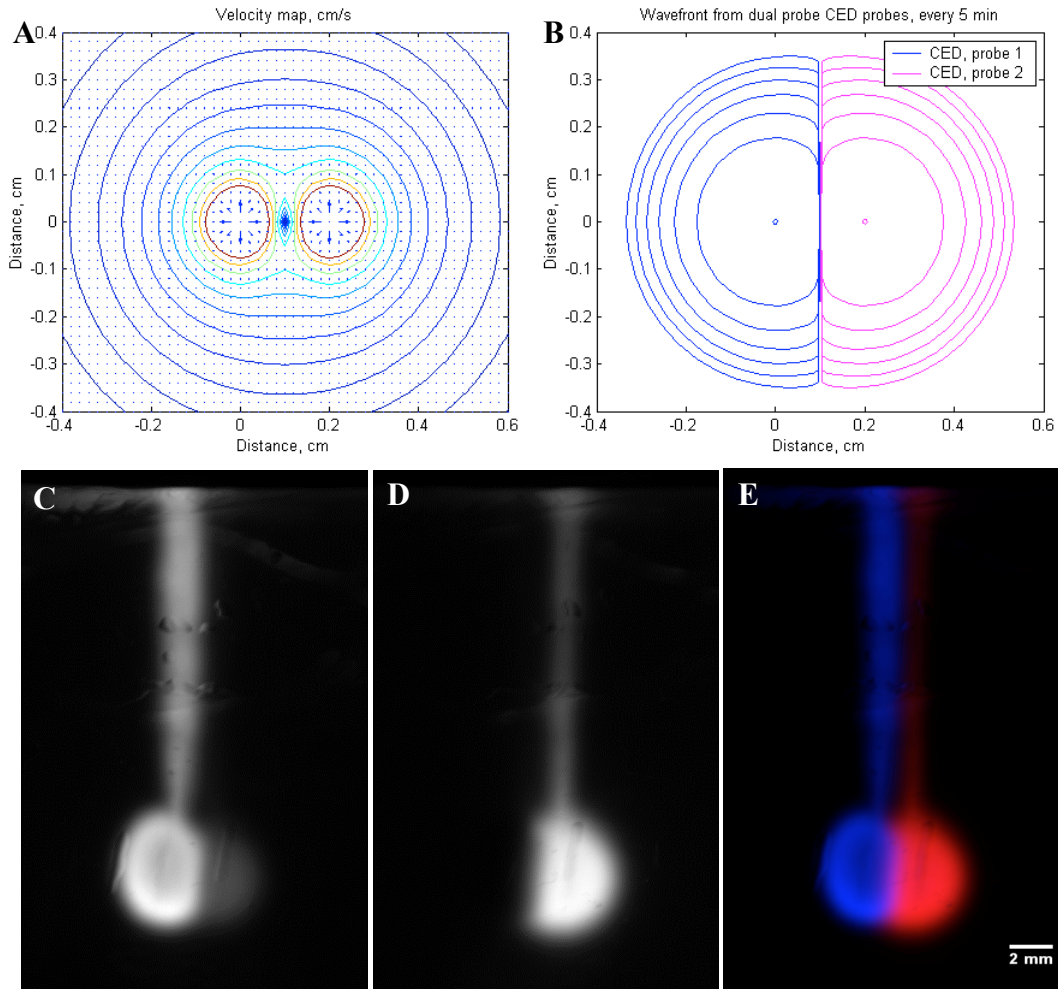
Figure 4. Dual probe CED, model and *in vitro* example. A-B. Fluid velocity and wavefront pattern. CED probe 1 is centered at (0,0) and CED probe 2 is centered at (0.2, 0). A. Velocity distribution following CED infusions at 0.8 μl/min. The arrow size represents the relative magnitude of the velocity and the arrow points in the direction of the velocity vector. Curves represent decreasing speed from red to blue. Note a point of zero velocity exists directly between the two probes at (0.1, 0). B. Wavefront of both CED infusions, probe 1 (blue) and probe 2 (pink), at 5 minute intervals.. Note that the infusions are spatially separated and no overlap of the two infusions occurs. C-E. *In vitro* dual probe CED into an 0.5% agarose gel brain phantom of albumin-Alexa Fluor 647 (left probe) and Texas Red-dextran (right probe). The close positioning of the two probes, 2 mm apart, results in the hemispherical distribution of each fluorophore. C. Albumin-Alexa Fluor 647 fluorescence. D. Texas Red-dextran fluorescence. E. Combined fluorescent image.

image (Figure 4E) shows that there is a small overlap between the two fluorophores at the surface separating the two infusions. This is likely a result of diffusion of the two fluorophores in combination with inhomogenities associated with probe construction such that the velocity at the surface between the probes is not exactly equal and opposite.

Multi-probe CED is particularly useful for drug patterning in the brain because the region of distribution is highly delineated by the presence of the other probes. Thus, the infusion distribution is no longer necessarily spherical but can be altered by infusion of physiological saline or other drugs by adjacent CED probes. Further, this type of drug patterning could be useful in a situation where drug should be distributed through an entire brain region while sparing critical tissues within that region. This could be done by infusing a non-toxic saline solution into the critical area while simultaneously infusing the drug into the larger regional space. In order to enable such combination therapy, it will be necessary to know the tissue properties in advance of patterning planning or to use real time imaging [41,42] such that the infusion flow rates could be altered based on the distribution of the ongoing infusion.

Lastly, the model also suggests a strategy whereby a rapidly eliminated BBB permeable drug could be administered systemically and a saline solution could be infused into the tumor. The pressure of the saline infusion would reduce the drug extravasation into the tumor but would have no effect on the drug extravasation into normal tissue. This could have many potential applications, including the infusion of known radiation protectants [43], whereby the neuroprotectant would accumulate in the normal tissue but the tumor would remain susceptible to radiation therapy.

IV.5. Summary

In considering the use of CED and R-CED, it is useful to have a simple model to predict the size of the affected region. We have shown that the size of the affected region is highly dependent on the hydraulic conductivity across the blood vessel wall, the hydraulic conductivity through the interstitium, and the rate of fluid removal from the brain. R-CED and CED will influence a larger tissue region in tissues where the combination of the interstitial and vascular resistance to flow are optimized to fall on the local maximum predicted by the model. To use R-CED to treat large tumors, a significantly larger tissue region can be influenced by reducing the vascular hydraulic permeability two orders of magnitude using anti-angiogenic agents such as VEGF. Alternatively, the interstitial hydraulic conductivity can be altered using enzymatic means to degrade or build up the extracellular resistance.

By increasing the affected tissue region individually for the R-CED and CED probes, it will become technically possible to place the probes farther apart (on the order of 1 cm) and achieve a substantial non-zero effect on the tissue pressure and fluid velocity in the space between the probes. This enables the development of combination CED and R-CED therapy, allowing for strict control of the interstitial bulk flow and delivery of particulates and macromolecules within the interstitial space. Further, multi-probe CED therapy enables the possibility of drug patterning within the tissue space and the potential for sparing of critical regions within an area of drug infusion. *In vivo* monitoring and detailed knowledge of the tissue properties will enable more accurate predictions of the drug distribution and the development of multiprobe CED/R-CED for controlled drug patterning within the brain.

IV.6. Acknowledgements

IV.7. References

[1]   D.R. Groothuis, M.W. Vavra, K.E. Schlageter, E.W. Kang, A.C. Itskovich, S. Hertzler, C.V. Allen and H.L. Lipton, Efflux of drugs and solutes from brain: the interactive roles of diffusional transcapillary transport, bulk flow and capillary transporters. *J Cereb Blood Flow Metab.* 27, **(**2007) 43-56.

[2]   M.Y. Chen, R.R. Lonser, P.F. Morrison, L.S. Governale and E.H. Oldfield, Variables affecting convection-enhanced delivery to the striatum: a systematic examination of rate of infusion, cannula size, infusate concentration, and tissue-cannula sealing time. *J Neurosurg.* 90, **(**1999) 315-320.

[3]   J.K. Tunggal, D.S. Cowan, H. Shaikh and I.F. Tannock, Penetration of anticancer drugs through solid tissue: a factor that limits the effectiveness of chemotherapy for solid tumors. *Clin Cancer Res.* 5, **(**1999) 1583-1586.

[4]   D.R. Groothuis, H. Benalcazar, C.V. Allen, R.M. Wise, C. Dills, C. Dobrescu, V. Rothholtz and R.M. Levy, Comparison of cytosine arabinoside delivery to rat brain by intravenous, intrathecal, intraventricular and intraparenchymal routes of administration. *Brain Res.* 856, **(**2000) 281-290.

[5]   G.H. Huynh, D.F. Deen and F.C. Szoka, Jr., Barriers to carrier mediated drug and gene delivery to brain tumors. *J Control Release.* 110, **(**2006) 236-259.

[6]   K.A. Lopez, A.E. Waziri, P.D. Canoll and J.N. Bruce, Convection-enhanced delivery in the treatment of malignant glioma. *Neurol Res.* 28, **(**2006) 542-548.

[7]   W.A. Hall, E. Rustamzadeh and A.L. Asher, Convection-enhanced delivery in clinical trials. *Neurosurg Focus.* 14, **(**2003) e2.

[8]   R. Raghavan, M.L. Brady, M.I. Rodriguez-Ponce, A. Hartlep, C. Pedain and J.H. Sampson, Convection-enhanced delivery of therapeutics for brain disease, and its optimization. *Neurosurg Focus.* 20, **(**2006) E12.

[9]   R.H. Bobo, D.W. Laske, A. Akbasak, P.F. Morrison, R.L. Dedrick and E.H. Oldfield, Convection-enhanced delivery of macromolecules in the brain. *Proc Natl Acad Sci U S A.* 91, **(**1994) 2076-2080.

[10]   M.T. Krauze, J. Forsayeth, J.W. Park and K.S. Bankiewicz, Real-time imaging and quantification of brain delivery of liposomes. *Pharm Res.* 23, **(**2006) 2493-2504.

[11]   J.A. MacKay, D.F. Deen and F.C. Szoka, Jr., Distribution in brain of liposomes after convection enhanced delivery; modulation by particle charge, particle diameter, and presence of steric coating. *Brain Res.* 1035, **(**2005) 139-153.

[12]   L.T. Baxter and R.K. Jain, Transport of fluid and macromolecules in tumors. I. Role of interstitial pressure and convection. *Microvasc Res.* 37, **(**1989) 77-104.

[13]   S. Kalyanasundaram, V.D. Calhoun and K.W. Leong, A finite element model for predicting the distribution of drugs delivered intracranially to the brain. *Am J Physiol.* 273, **(**1997) R1810-1821.

[14]   P.J. Basser, Interstitial pressure, volume, and flow during infusion into brain tissue. *Microvasc Res.* 44, **(**1992) 143-165.

[15]   V.A. Levin, C.S. Patlak and H.D. Landahl, Heuristic modeling of drug delivery to malignant brain tumors. *J Pharmacokinet Biopharm.* 8, **(**1980) 257-296.

[16]   P.F. Morrison, D.W. Laske, H. Bobo, E.H. Oldfield and R.L. Dedrick, High-flow microinfusion: tissue penetration and pharmacodynamics. *Am J Physiol.* 266, **(**1994) R292-305.

[17]   J.H. Smith and J.A. Humphrey, Interstitial transport and transvascular fluid exchange during infusion into brain and tumor tissue. *Microvasc Res.* 73, **(**2007) 58-73.

[18]   G.H. Huynh, T. Ozawa, D.F. Deen, T. Tihan and F.C. Szoka, Jr., Retro-convection enhanced delivery to increase blood to brain transfer of macromolecules. *Brain Res.* **(**2006).

[19]   G.R. DiResta, J. Lee, J.H. Healey, A. Levchenko, S.M. Larson and E. Arbit, "Artificial lymphatic system": a new approach to reduce interstitial hypertension and increase blood flow, pH and pO2 in solid tumors. *Ann Biomed Eng.* 28, **(**2000) 543-555.

[20]   G.R. DiResta, J. Lee, J.H. Healey, S.M. Larson and E. Arbit, Enhancing the uptake of chemotherapeutic drugs into tumors using an "artificial lymphatic system". *Ann Biomed Eng.* 28, **(**2000) 556-564.

[21]   L.T. Baxter and R.K. Jain, Transport of fluid and macromolecules in tumors. IV. A microscopic model of the perivascular distribution. *Microvasc Res.* 41, **(**1991) 252-272.

[22]   X.Y. Zhang, J. Luck, M.W. Dewhirst and F. Yuan, Interstitial hydraulic conductivity in a fibrosarcoma. *Am J Physiol Heart Circ Physiol.* 279, **(**2000) H2726-2734.

[23]   P.A. Netti, D.A. Berk, M.A. Swartz, A.J. Grodzinsky and R.K. Jain, Role of extracellular matrix assembly in interstitial transport in solid tumors. *Cancer Res.* 60, **(**2000) 2497-2503.

[24]   E.A. Swabb, J. Wei and P.M. Gullino, Diffusion and convection in normal and neoplastic tissues. *Cancer Res.* 34, **(**1974) 2814-2822.

[25]   F. Yuan, Y. Chen, M. Dellian, N. Safabakhsh, N. Ferrara and R.K. Jain, Time-dependent vascular regression and permeability changes in established human tumor xenografts induced by an anti-vascular endothelial growth factor/vascular permeability factor antibody. *Proc Natl Acad Sci U S A.* 93, **(**1996) 14765-14770.

[26]   R. Tong, Dynamics of vascular normalization during anti-angiogenic therapy: Implications for combination therapy. HST, Vol. PhD in Medical Engineering, MIT, Boston, MA, 2005, p. 103.

[27]   Y. Boucher, I. Lee and R.K. Jain, Lack of general correlation between interstitial fluid pressure and oxygen partial pressure in solid tumors. *Microvasc Res.* 50, **(**1995) 175-182.

[28]   C. Nicholson and J.M. Phillips, Ion diffusion modified by tortuosity and volume fraction in the extracellular microenvironment of the rat cerebellum. *J Physiol.* 321, **(**1981) 225-257.

[29]   R. Saito, J.R. Bringas, T.R. McKnight, M.F. Wendland, C. Mamot, D.C. Drummond, D.B. Kirpotin, J.W. Park, M.S. Berger and K.S. Bankiewicz, Distribution of liposomes into brain and rat brain tumor models by convection-enhanced delivery monitored with magnetic resonance imaging. *Cancer Res.* 64, **(**2004) 2572-2579.

[30] C. Mamot, J.B. Nguyen, M. Pourdehnad, P. Hadaczek, R. Saito, J.R. Bringas, D.C. Drummond, K. Hong, D.B. Kirpotin, T. McKnight, M.S. Berger, J.W. Park and K.S. Bankiewicz, Extensive distribution of liposomes in rodent brains and brain tumors following convection-enhanced delivery. *J Neurooncol.* 68, **(**2004) 1-9.

[31] M.T. Krauze, R. Saito, C. Noble, M. Tamas, J. Bringas, J.W. Park, M.S. Berger and K. Bankiewicz, Reflux-free cannula for convection-enhanced high-speed delivery of therapeutic agents. *J Neurosurg.* 103, **(**2005) 923-929.

[32] K. Rubin, M. Sjoquist, A.M. Gustafsson, B. Isaksson, G. Salvessen and R.K. Reed, Lowering of tumoral interstitial fluid pressure by prostaglandin E(1) is paralleled by an increased uptake of (51)Cr-EDTA. *Int J Cancer.* 86, **(**2000) 636-643.

[33] D.R. Groothuis, S. Ward, K.E. Schlageter, A.C. Itskovich, S.C. Schwerin, C.V. Allen, C. Dills and R.M. Levy, Changes in blood-brain barrier permeability associated with insertion of brain cannulas and microdialysis probes. *Brain Res.* 803, **(**1998) 218-230.

[34] L.H. Bookbinder, A. Hofer, M.F. Haller, M.L. Zepeda, G.A. Keller, J.E. Lim, T.S. Edgington, H.M. Shepard, J.S. Patton and G.I. Frost, A recombinant human enzyme for enhanced interstitial transport of therapeutics. *J Control Release.* 114, **(**2006) 230-241.

[35] T.C. Laurent and J.R. Fraser, Hyaluronan. *Faseb J.* 6, **(**1992) 2397-2404.

[36] A. Tona and A. Bignami, Effect of hyaluronidase on brain extracellular matrix in vivo and optic nerve regeneration. *J Neurosci Res.* 36, **(**1993) 191-199.

[37] M. Jansen, P.C. de Witt Hamer, A.N. Witmer, D. Troost and C.J. van Noorden, Current perspectives on antiangiogenesis strategies in the treatment of malignant gliomas. *Brain Res Brain Res Rev.* 45, **(**2004) 143-163.

[38] W.B. Pope, A. Lai, P. Nghiemphu, P. Mischel and T.F. Cloughesy, MRI in patients with high-grade gliomas treated with bevacizumab and chemotherapy. *Neurology.* 66, **(**2006) 1258-1260.

[39] E.M. Johnson, D.A. Berk, R.K. Jain and W.M. Deen, Hindered diffusion in agarose gels: test of effective medium model. *Biophys J.* 70, **(**1996) 1017-1023.

[40] E.A. Chiocca, W.C. Broaddus, G.T. Gillies, T. Visted and M.L. Lamfers, Neurosurgical delivery of chemotherapeutics, targeted toxins, genetic and viral therapies in neuro-oncology. *J Neurooncol.* 69, **(**2004) 101-117.

[41] J. Voges, R. Reszka, A. Gossmann, C. Dittmar, R. Richter, G. Garlip, L. Kracht, H.H. Coenen, V. Sturm, K. Wienhard, W.D. Heiss and A.H. Jacobs, Imaging-guided convection-enhanced delivery and gene therapy of glioblastoma. *Ann Neurol.* 54, **(**2003) 479-487.

[42] R. Saito, M.T. Krauze, J.R. Bringas, C. Noble, T.R. McKnight, P. Jackson, M.F. Wendland, C. Mamot, D.C. Drummond, D.B. Kirpotin, K. Hong, M.S. Berger, J.W. Park and K.S. Bankiewicz, Gadolinium-loaded liposomes allow for real-time magnetic resonance imaging of convection-enhanced delivery in the primate brain. *Exp Neurol.* 196, **(**2005) 381-389.

[43] M.S. Levi and M.A. Brimble, A review of neuroprotective agents. *Curr Med Chem.* 11, **(**2004) 2383-2397.

Appendix A: Multi-probe drug patterning: simultaneous CED infusion via two probes *in vivo*

A.1. Introduction

In Chapter IV, I have established the possibility of multi-probe drug patterning in the brain using a simple model prediction and an illustration of this concept in an agarose gel brain phantom. To further investigate the feasibility of multi-probe drug patterning, I completed a preliminary experiment in the normal rat brain. Because CED is already used in patients, I tested the simultaneous CED infusion via two probes spaced 2 mm apart, the closest it was technically feasible to position the probes. The prediction for the infusion distribution of both probes is illustrated in Figure 4A-B in Chapter IV, showing isolation of the two infusions. Our preliminary *in vivo* data show non-zero overlap between the infusions from the two probes, likely due to inhomogeneity in the tissue extracellular space between the two probes. The predicted hemispherical distribution is not easily visualized in the *in vivo* preliminary data. This example highlights the limitation of the model described in Chapter IV, which assumes the tissue to be a rigid homogenous porous medium with no vasculature and no cell uptake.

A.2. Results and Discussion

Simultaneous CED via two probes spaced 2 mm apart was performed in the normal rat brain. The probes were situated 3 mm to the right and $\pm$ 1 mm anterior and posterior of the bregma and inserted 5 mm below the top of the skull, with the intent to insert both probes into the caudate putamen. The anterior probe was loaded with 1 mg/ml Albumin-Alexa Fluor 647 in PBS; the posterior probe was loaded with 1 mg/ml FITC-

dextran in PBS. Both infusions were carried out using the step up flow protocol described by Bankiewicz and coworkers to reduce backflow along the probe track [4]. Following the infusion, animals were immediately euthanized.
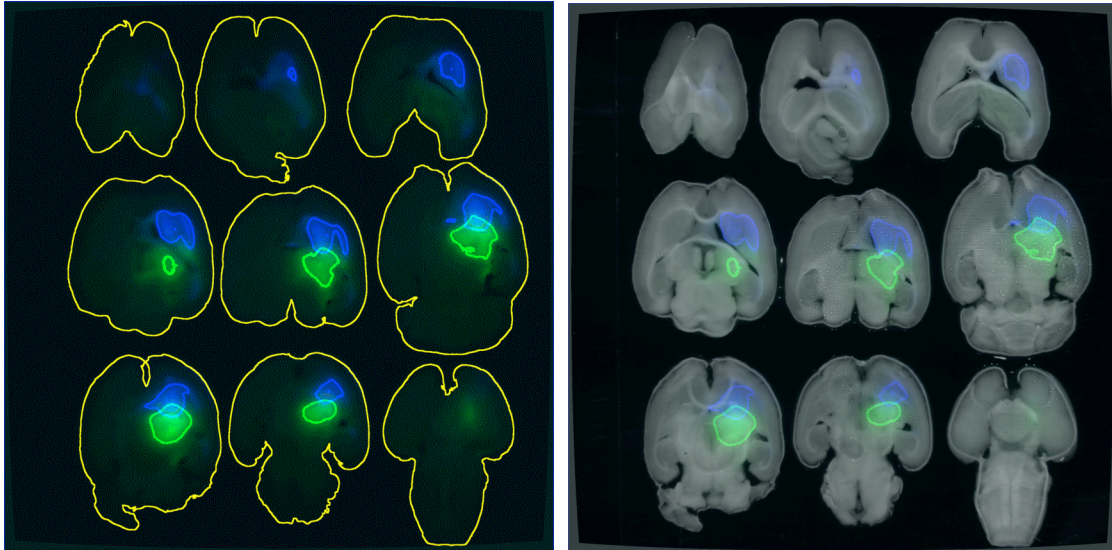
Figure 1. Axial sections of rat brain where FITC dextran (green) and Albumin-Alexa Fluor 647 (blue) have been infused by simultaneous CED via probes spaced 2 mm apart in the anterior-posterior direction. Axial sections, 1 mm thick, are positioned from superior to inferior of the brain as the slices go from left to right, top to bottom. Green and blue outlines delineate the region that has a five times greater fluorescence than background. Overlap between the green and blue regions is most apparent in the sixth and seventh slice from the top.

The fluorescence in 1 mm axial sections is shown in Figure 1. Inspection of this image shows that in practice, the posterior FITC-dextran infusion was primarily within the thalamus. Because this structure is intimately connected to the caudate putamen, an interface could be located where the Albumin-Alexa Fluor 647 and FITC-dextran infusions interacted (visualized in slice 6 and 7 from the top of the brain). Further, unlike the results of the model and the agarose phantom experiments, significant overlap is apparent between the two CED infusions, particularly in slice 6 and 7 from the top of the

brain. This result is counter to the model calculation, which predicts that because both CED infusions theoretically have the same velocity distribution, a surface exists between the two probes where the velocities cancel out, resulting in isolation of each infusion.

It is possible that the apparent overlap between the two infusions occurs because our images of the thick sections contain fluorescence from both the surface of the slice and from deeper within the slice. If the boundary between the two infusions is not perfectly perpendicular to the surface of the slice, the apparent position of the boundary varies with the depth in the slice. Thus, our image of the thick section would show a blurred boundary that would appear to be overlap between the two infusions. To determine if this is the case, slices were further imaged by confocal microscopy.

Confocal images of slice 7 from the top of the brain are shown Figure 2. It is clear that the overlap between the Albumin-Alexa Fluor 647 and the FITC-dextran is not simply an artifact of imaging thick sections. The region having five times greater fluorescence than the background is outlined, with the overlapping region ranging in width from 0 to 0.5 mm. This overlap is too large to be simply explained by diffusion of the fluorescent markers.

Figure 2. Confocal section of overlapping region in slice 7 of Figure 1. Outlines delineate the region which has five times greater fluorescence than background.
A. Albumin - Alexa647 fluorescence.
B. FITC- dextran fluorescence.
C. Overlay of Albumin-Alexa647 and FITC-dextran fluorescence. Note that there is substantial overlap of the green and blue fluorescence.

0.5 mm

This preliminary experiment does not clearly explain the reason why an overlap between the two simultaneous CED infusions was observed. However, there are a few major parameters which violate the assumptions of our model that are likely contributors to the observed distribution. Most importantly, the assumption that the two CED probes infuse into a homogenous porous medium is not satisfied in the brain infusion. Nicholson and colleagues have shown that the extracellular space may contain nearly 40% microdomains, such as dead end pores or lakes, which have inhomogenous physiological

characteristics and alter the ability for convectively driven flow to move through the tissue [2]. Further, because the rat caudate putamen is not very large, positioning the two probes 2 mm apart was still insufficient to insure that both probes were inserted into the same brain structure. In our case, the FITC-dextran CED probe was inserted into the thalamus, which has significant projections to the caudate putamen. Preferential directed flow along these projections could contribute to the apparent overlap in the distribution of the two infusions.

The confocal images also do not definitively elucidate the potential role of tracer movement through the brain via cell uptake or by active transport to the vasculature and back into the brain at different locations. As shown in Figure 2, the FITC-dextran appears to have a more punctate appearance compared to the Albumin-Alexa Fluor 647. This preliminary data does not clearly show which cells are taking up the FITC-dextran and if there is any preferential transport through cells which uptake the fluorescent tracer. It is less likely that the fluorophore distribution is highly affected by active transport to the vasculature and back into the brain. The albumin transporter, gp60, which actively transcytoses albumin across the endothelial wall in non-CNS tissues, is nearly completely absent at the blood brain barrier [7,9]. FITC-dextran is also generally not considered to be a substrate for active transcytosis across the blood brain barrier, as its movement across intact vasculature is primarily size and charge dependent.

Thus, these initial studies show that there is significant variability in the rat tissue physiological properties compared to the homogenous agarose brain phantom. In combination with the small size of the rat brain structures, the small infusion volumes and the technical challenges of placing the two CED probes very close together should be

considered to understand how the *in vivo* distribution will be different from our idealized model prediction. An *in vivo* demonstration of the simultaneous CED drug patterning effect may be more easily visualized in larger animals where brain structures are larger and close positioning of the probes would target a more homogenous tissue region.

A.3. Materials and Methods

A.3.1. CED procedure: *in vivo*

CED was completed as described for an acute stereotactic infusion [1,6,8]. Briefly, a narrow cannula was prepared from fused silica tubing with an outer diameter of 0.16 mm (Polymicro Technologies, Phoenix, AZ), extending 1-2 mm from the tip of a 24 gauge needle used for support [4]. A hole was drilled 3 mm to the right of the bregma and $\pm$ 1 mm anterior/posterior of the bregma. Either a lysine fixable FITC-dextran (MolecularProbes; Carlsbad, CA) or Albumin-Alexa Fluor 647 (Molecular Probes; Carlsbad, CA) was infused. Probes were implanted 5 mm below the top of the skull. An external syringe pump (Bioanalytical Systems Inc; West Lafayette, IN) was used to drive the infusion in both probes at an increasing flowrate as follows: 0.1 μL /min for 5 min, 0.2 μL /min for 5 min, 0.5 μL /min for 5 min, and 0.8 μL /min for 30 min for a total volume of 28 μL infused over 45 min. Following the infusion, the probe was removed slowly and the animal euthanized by perfusion fixation with 350 ml of phosphate-buffered saline (PBS: 100 mM phosphate, 150 mM NaCl, pH 7.4) and 350 ml of 4% paraformaldehyde in PBS. Brains were removed and fixed overnight in 4% paraformaldehyde at room temperature.

A.3.2. Macroscopic imaging and analysis

Macroscopic images were obtained using a Kodak Imagestation In Vivo FX (New Haven, CT). Albumin-Alexa Fluor 647 was acquired using excitation through a 625 nm filter and emission through a 700 nm filter. FITC-dextran was acquired using excitation through a 485 nm filter and emission through a 535 nm filter. White light images were acquired using no excitation or emission filters. A threshold was applied to visualize the volume where the intensity is five times greater than background to identify the wavefront of the CED infusion [3,5].

A.3.3. Confocal fluorescence microscopy and analysis

Confocal images were obtained to visualize the distribution of CED infused material. All images were taken using LaserSharp Software on a Biorad 1024 Confocal Scanning Laser Microscope (Hercules, CA) mounted on a Nikon Diaphot 200 microscope. Albumin-Alexa Fluor 647 was acquired in photomultiplier 3 with excitation from the 633 nm line of a helium-neon laser. FITC-dextran was acquired in photomultiplier 2 with excitation from the 488 nm line of a krypton-argon laser. One millimeter brain sections were imaged using a 4x objective lens at a resolution of 2.5 μm per pixel. A threshold was applied to visualize the volume where the intensity is five times greater than background to identify the wavefront of the CED infusion.

A.4. References

[1]   R.H. Bobo, D.W. Laske, A. Akbasak, P.F. Morrison, R.L. Dedrick and E.H. Oldfield, Convection-enhanced delivery of macromolecules in the brain. *Proc Natl Acad Sci U S A.* 91, **(**1994) 2076-2080.

[2]   S. Hrabetova and C. Nicholson, Contribution of dead-space microdomains to tortuosity of brain extracellular space. *Neurochem Int.* 45, **(**2004) 467-477.

[3]   G.H. Huynh, T. Ozawa, D.F. Deen, T. Tihan and F.C. Szoka, Jr., Retro-convection enhanced delivery to increase blood to brain transfer of macromolecules. *Brain Res.* **(**2006).

[4]   M.T. Krauze, R. Saito, C. Noble, M. Tamas, J. Bringas, J.W. Park, M.S. Berger and K. Bankiewicz, Reflux-free cannula for convection-enhanced high-speed delivery of therapeutic agents. *J Neurosurg.* 103, **(**2005) 923-929.

[5]   J.A. MacKay, D.F. Deen and F.C. Szoka, Jr., Distribution in brain of liposomes after convection enhanced delivery; modulation by particle charge, particle diameter, and presence of steric coating. *Brain Res.* 1035, **(**2005) 139-153.

[6]   C. Mamot, J.B. Nguyen, M. Pourdehnad, P. Hadaczek, R. Saito, J.R. Bringas, D.C. Drummond, K. Hong, D.B. Kirpotin, T. McKnight, M.S. Berger, J.W. Park and K.S. Bankiewicz, Extensive distribution of liposomes in rodent brains and brain tumors following convection-enhanced delivery. *J Neurooncol.* 68, **(**2004) 1-9.

[7]   W.M. Pardridge, J. Eisenberg and W.T. Cefalu, Absence of albumin receptor on brain capillaries in vivo or in vitro. *Am J Physiol.* 249, **(**1985) E264-267.

[8]   R. Saito, J.R. Bringas, T.R. McKnight, M.F. Wendland, C. Mamot, D.C. Drummond, D.B. Kirpotin, J.W. Park, M.S. Berger and K.S. Bankiewicz, Distribution of liposomes into brain and rat brain tumor models by convection-enhanced delivery monitored with magnetic resonance imaging. *Cancer Res.* 64, **(**2004) 2572-2579.

[9]   J.E. Schnitzer, gp60 is an albumin-binding glycoprotein expressed by continuous endothelium involved in albumin transcytosis. *Am J Physiol.* 262, **(**1992) H246-254.

Appendix B: Model code to implement equations in Chapter IV

B.1. Introduction

All code was written in Matlab v.6 Release 12, running on a Windows virtual machine from a MacBook, using the following code. The code for figure 1 and 2 were saved as .m files and called from the main Matlab window.

B.2. Code
B.2.1. Code for Figure 1.

```
%Grace Huynh
%2.6.07
%Figure 1
%calculate the pressure profile, interstitial and transendothelial velocity profile
%using Equation 3
%for figure 1A-C


%initialize
clear all;
close all;

%Define the modeling space
R = 1;          %cm, total tissue radius from R-CED probe where model will be calculated
rinit = 0.03;
r = rinit:0.01:R;   %cm, increment within the modeling space

%Tissue definitions
SoverV = 250;     %cm-1 Ratio of blood vessel surface area to volume of tissue
BP = 120;         %mmHg, blood pressure

%Probe parameters
Rm = 0.065/2;          %cm catheter radius
rhat = Rm/R;          %no units, ratio of probe radius to total modeling space radius
A = 2*pi*Rm*0.2;      %cm2 membrane area




%NORMAL BRAIN

%tissue parameters specific to normal brain
Lp = 9.5e-10;              %cm/mmHg-sec, hydraulic conductivity across bv wall
K = 6.7e-6;                %cm2/mmHg-sec, hydraulic conductivity through ECS
alpha = R*sqrt(Lp*SoverV/K); %dimensionless measure of interstitial and vascular resistance to
flow, see Eq. 1
ptissue = 0;              %mmHg, pressure of normal surrounding tissue
pe = 0;                  %mmHg, pressure of normal nearby tissue

%fluid removal rate from normal brain
qm = 5.3/60;       %ul/min, volumetric flow rate of removing fluid
um = -qm*10^-3/A;   %cm/min, flow velocity at membrane
```

%Calculate c1 and c2 before calculating the pressure in Eq. 3
c2num = -(um*Rm*Rm/K) - R*(ptissue - pe)*(alpha*rhat*sinh(alpha*rhat) - cosh(alpha*rhat)) / cosh(alpha);
c2denom = alpha*rhat*cosh(alpha*rhat) - sinh(alpha*rhat) -
alpha*rhat*sinh(alpha*rhat)*sinh(alpha) / cosh(alpha) + cosh(alpha*rhat)*sinh(alpha)/cosh(alpha);
c2 = c2num/c2denom;
c1 = (R*(ptissue - pe) - c2*sinh(alpha))/cosh(alpha);
pnormalRCED = (c1*cosh(alpha.*r/R)) ./ r + (c2*sinh(alpha.*r/R)) ./ r + pe;

%Calculate pressure with zero flow using Eq. 3
qm = 0;   %ul/min, volumetric flow rate of removing fluid
um = qm*10^-3/A; %cm/min, flow velocity at membrane

%Calculate c1 and c2 to calculate the pressure with zero flow using Eq. 3
c2num = -(um*Rm*Rm/K) - R*(ptissue - pe)*(alpha*rhat*sinh(alpha*rhat) - cosh(alpha*rhat)) / cosh(alpha);
c2denom = alpha*rhat*cosh(alpha*rhat) - sinh(alpha*rhat) -
alpha*rhat*sinh(alpha*rhat)*sinh(alpha) / cosh(alpha) + cosh(alpha*rhat)*sinh(alpha)/cosh(alpha);
c2 = c2num/c2denom;
c1 = (R*(ptissue - pe) - c2*sinh(alpha))/cosh(alpha);
pnormal = (c1.*cosh(alpha.*r./R)) ./ r + (c2.*sinh(alpha.*r./R)) ./ r + pe;

%Determine the radius where we have reached pressure threshold (3 mmHg)
pdiff = pnormal-pnormalRCED;
if find(pdiff < 3) == isempty(find(pdiff < 3))
   counter = length(r);
else
   counter = min(find(pdiff < 3));
end
distancenormal = counter*0.01;

%Calculate flow velocity distribution profile
unormalRCED = -K*diff(pnormalRCED)/0.01; %0.01 radial step cm

%Calculate proportion of flow from blood, blood to tissue is positive, cm/sec
qbloodnormal = Lp*(BP-pnormal);
qbloodnormalRCED = Lp*(BP-pnormalRCED)-qbloodnormal;

%TUMOR

%tissue parameters specific to tumor brain
Lp = 1.11e-7;   %cm/mmHg-sec tumor conductivity across capillary wall
K = 6.5e-7;   %cm2/mmHg-sec conductivity through tumor ECS
alpha = R*sqrt(Lp*SoverV/K); %dimensionless measure of interstitial and vascular resistance to flow, see Eq. 1
ptissue = 0;   %mmHg pressure of normal tissue
pe = 9.5;   %mmHg pressure of U87 tumor

qm = 8.3/60;   %ul/min, volumetric flow rate of removing fluid
um = -qm*10^-3/A; %cm/min, flow velocity at membrane

```
%Calculate c1 and c2 before calculating the pressure in Eq. 3
c2num = -(um*Rm*Rm/K) - R*(ptissue - pe)*(alpha*rhat*sinh(alpha*rhat) - cosh(alpha*rhat)) /
cosh(alpha);
c2denom = alpha*rhat*cosh(alpha*rhat) - sinh(alpha*rhat) -
alpha*rhat*sinh(alpha*rhat)*sinh(alpha) / cosh(alpha) + cosh(alpha*rhat)*sinh(alpha)/cosh(alpha);
c2 = c2num/c2denom;
c1 = (R*(ptissue - pe) - c2*sinh(alpha))/cosh(alpha);
ptumorRCED = (c1*cosh(alpha.*r/R)) ./ r + (c2*sinh(alpha.*r/R)) ./ r + pe;

%draw the original tumor pressure profile before RCED
%Calculate pressure profile with zero flow using Eq. 3
qm = 0;          %ul/min, volumetric flow rate of removing fluid
um = qm*10^-3/A; %cm/min, flow velocity at membrane
c2num = -(um*Rm*Rm/K) - R*(ptissue - pe)*(alpha*rhat*sinh(alpha*rhat) - cosh(alpha*rhat)) /
cosh(alpha);
c2denom = alpha*rhat*cosh(alpha*rhat) - sinh(alpha*rhat) -
alpha*rhat*sinh(alpha*rhat)*sinh(alpha) / cosh(alpha) + cosh(alpha*rhat)*sinh(alpha)/cosh(alpha);
c2 = c2num/c2denom;
c1 = (R*(ptissue - pe) - c2*sinh(alpha))/cosh(alpha);
ptumor = (c1*cosh(alpha.*r/R)) ./ r + (c2*sinh(alpha.*r/R)) ./ r + pe;


%Determine the radius where we have reached pressure threshold (3 mmHg)
pdiff = ptumor-ptumorRCED;
if find(pdiff < 3) == isempty(find(pdiff < 3))
    counter = length(r);
else
    counter = min(find(pdiff < 3));
end
distancetumor = counter*0.01;

%Calculate flow velocity distribution profile
utumor = -K*diff(ptumor)/0.01; % subtract off the apparent velocity due to the initial condition of
the pressure profile
utumorRCED = -K*diff(ptumorRCED)/0.01 - utumor; %0.01 radial step, cm

%Calculate proportion from blood, from blood to tissue is positive, cm/sec
qbloodtumor = Lp*(BP-ptumor);
qbloodtumorRCED = Lp*(BP-ptumorRCED)-qbloodtumor;


%%%%%%
%%%%%%
%Draw the figures
set(0, 'defaultaxesfontsize', 10, 'defaultlineLineWidth', 2);

%Draw the pressure profiles for normal and tumor brain
close all; figure;
axes('position', [0.13 0.72 0.33 0.25]); plot(r,pnormalRCED, 'LineWidth', 3);
hold on; line2 = plot(r,pnormal,'r', 'LineWidth', 3);
hold on; plot(r,ptumorRCED, 'k-.', 'LineWidth', 3);
hold on; plot(r,ptumor,'m--', 'LineWidth', 3);
xlabel('Radius cm'); ylabel('Pressure mmHg'); title('Pressure profile surrounding RCED probe');
axis([0 1 -80 10]);
legend ('normal brain, RCED', 'normal brain', 'tumor brain, RCED', 'tumor brain', 4)
```

```
%Draw the flow velocity profiles for normal and tumor brain
ru = rinit+0.005:0.01:R; %radius position as average btwn the steps, cm
axes('position', [0.54 0.72 0.33 0.25]); plot(ru, unormalRCED*10*1000*-1);
hold on; plot(ru, utumorRCED*10*1000*-1, 'k-.');
title('Velocity towards RCED probe'); ylabel('Velocity, \mum/s'); xlabel('Radius, cm');
legend('normal brain, RCED', 'tumor brain, RCED', 1);

%Draw the flow velocity from the blood into the tissue
axes('position', [0.13 0.38 0.33 0.25]); semilogy(r, qbloodnormalRCED*10^4);
hold on; semilogy(r, qbloodtumorRCED*10^4, 'k-.');
title('Velocity across endothelial wall due to R-CED'); ylabel('Flux velocity, \mum/s');
xlabel('Radius, cm');
%axis([0 1 0 0.1]);
legend('normal brain, RCED', 'tumor brain, RCED', 1);




%%%%%
%for figure 1D
%Calculate the size of the R-CED affected region for varying
%Lp (vascular hydraulic conductivity) and K (interstitial hydraulic conductivity)
%using Equation 3


%initialize
clear all;

%Define the modeling space
R = 1;          %cm, total tissue radius from R-CED probe where model will be calculated
r = 0.05:0.01:R;   %cm, increment within the modeling space

%Tissue definitions
SoverV = 250;     %cm-1 Ratio of blood vessel surface area to volume of tissue
BP = 120;         %mmHg, blood pressure
ptissue = 0;      %mmHg pressure of normal tissue
pe = 9.5;         %mmHg pressure of tumor

%Probe parameters
Rm = 0.065/2;        %cm catheter radius
rhat = Rm/R;         %no units, ratio of probe radius to total modeling space radius
A = 2*pi*Rm*0.2;     %cm2 membrane area


%Calculate Equation 3 for varying qm and Lp
Lpcounter = 1;
for Lp = logspace(-11, -7, 100)  %defines the range of Lp
   Kcounter = 1;

   for K = logspace(-8, -5, 100);
                  alpha = R*sqrt(Lp*SoverV/K); %dimensionless measure of interstitial and
```

vascular resistance to flow, see Eq. 1

```
                %Calculate R-CED pressure distribution at given K and Lp
    qm = 8.3/60;      %ul/min, volumetric flow rate of removing fluid
    um = -qm*10^-3/A;   %cm/min, flow velocity at membrane

    %Calculate c1 and c2 before calculating the pressure in Eq. 3
                c2num = -(um*Rm*Rm/K) - R*(ptissue - pe)*(alpha*rhat*sinh(alpha*rhat) -
cosh(alpha*rhat)) / cosh(alpha);
    c2denom = alpha*rhat*cosh(alpha*rhat) - sinh(alpha*rhat) -
alpha*rhat*sinh(alpha*rhat)*sinh(alpha) / cosh(alpha) + cosh(alpha*rhat)*sinh(alpha)/cosh(alpha);
                c2 = c2num/c2denom;
                c1 = (R*(ptissue - pe) - c2*sinh(alpha))/cosh(alpha);
                pRCED = (c1*cosh(alpha.*r/R)) ./ r + (c2*sinh(alpha.*r/R)) ./ r + pe;


    %Calculate pressure with zero flow using Eq. 3
    qm = 0;         %ul/min, volumetric flow rate of removing fluid
    um = -qm*10^-3/A; %cm/min, flow velocity at membrane
                %Calculate c1 and c2 before calculating the pressure
                c2num = -(um*Rm*Rm/K) - R*(ptissue - pe)*(alpha*rhat*sinh(alpha*rhat) -
cosh(alpha*rhat)) / cosh(alpha);
    c2denom = alpha*rhat*cosh(alpha*rhat) - sinh(alpha*rhat) -
alpha*rhat*sinh(alpha*rhat)*sinh(alpha) / cosh(alpha) + cosh(alpha*rhat)*sinh(alpha)/cosh(alpha);
    c2 = c2num/c2denom;
    c1 = (R*(ptissue - pe) - c2*sinh(alpha))/cosh(alpha);
    ptumor = (c1*cosh(alpha.*r/R)) ./ r + (c2*sinh(alpha.*r/R)) ./ r + pe;

    %Determine the radius where we have reached pressure threshold (3 mmHg)
                pdiff = ptumor-pRCED;
    if find(pdiff < 3) == isempty(find(pdiff < 3))
       counter = length(r);
    else
       counter = min(find(pdiff < 3));
    end
    distance = counter*0.01;

    %Save the threshold distance in the matrix d
    d(Lpcounter, Kcounter)=distance;
    Kcounter = Kcounter + 1;
        end

Lpcounter = Lpcounter + 1;
end

%plot
axes('position', [0.56 0.39 0.31 0.25]);
[x,y] = meshgrid(logspace(-8, -5, 100), logspace(-11, -7, 100));
surf(x,y,d,'LineStyle', 'none');
axis tight; colorbar('vert')
view(0, 90);
title ({'  Size of R-CED affected tissue, cm'});
xlabel('Interst. cond. k, cm^2/mmHg-sec      ');
ylabel({'Vasc. cond. Lp, cm/mmHg-sec'});
zlabel('Radius of tissue with P < 3 mmHg, cm');
```

```
%%%%%
%for figure 1E
%Calculate the size of the R-CED affected region for varying
%K (interstitial hydraulic conductivity) and R-CED fluid removal rate
%using Equation 3


%initialize
clear all;

%Define the modeling space
R = 1;          %cm, total tissue radius from R-CED probe where model will be calculated
r = 0.05:0.01:R;   %cm, increment within the modeling space

%Tissue definitions
SoverV = 250;      %cm-1 Ratio of blood vessel surface area to volume of tissue
BP = 120;          %mmHg, blood pressure
ptissue = 0;       %mmHg pressure of normal tissue
pe = 9.5;          %mmHg pressure of tumor
Lp = 1.11e-7;      %vascular hydraulic permeability


%Probe parameters
Rm = 0.065/2;         %cm catheter radius
rhat = Rm/R;          %no units, ratio of probe radius to total modeling space radius
A = 2*pi*Rm*0.2;      %cm2 membrane area

%Calculate Equation 3 for varying qm and K
Kcounter = 1;
for K = logspace(-8, -5, 200) %defines the range of K
   alpha = R*sqrt(Lp*SoverV/K); %dimensionless measure of interstitial and vascular resistance
to flow, see Eq. 1

   %Calculate pressure with zero flow using Eq. 3
   %We will use this in combination with the pressure at a given flow to determine the radius
where we reach the pressure thereshold
      qm = 0;          %zero flux
      um = -qm*10^-3/A;  %cm/mincalculate flow velocity at membrane
   %Calculate c1 and c2 before calculating the pressure in Eq. 3
                c2num = -(um*Rm*Rm/K) - R*(ptissue - pe)*(alpha*rhat*sinh(alpha*rhat) -
cosh(alpha*rhat)) / cosh(alpha);
      c2denom = alpha*rhat*cosh(alpha*rhat) - sinh(alpha*rhat) -
alpha*rhat*sinh(alpha*rhat)*sinh(alpha) / cosh(alpha) + cosh(alpha*rhat)*sinh(alpha)/cosh(alpha);
      c2 = c2num/c2denom;
      c1 = (R*(ptissue - pe) - c2*sinh(alpha))/cosh(alpha);
      ptumor = (c1*cosh(alpha.*r/R)) ./ r + (c2*sinh(alpha.*r/R)) ./ r + pe;

   %Calculate pressure with increasing flow of removing fluid using Eq. 3
```

133

```matlab
    qmcounter = 1;
        for qm = 0.01:0.005:0.2; %ul/min, defines range of fluid removal
            um = -qm*10^-3/A;       %cm/min, flow velocity at membrane

            %Calculate c1 and c2 before calculating the pressure
            c2num = -(um*Rm*Rm/K) - R*(ptissue - pe)*(alpha*rhat*sinh(alpha*rhat) -
cosh(alpha*rhat)) / cosh(alpha);
        c2denom = alpha*rhat*cosh(alpha*rhat) - sinh(alpha*rhat) -
alpha*rhat*sinh(alpha*rhat)*sinh(alpha) / cosh(alpha) + cosh(alpha*rhat)*sinh(alpha)/cosh(alpha);
            c2 = c2num/c2denom;
            c1 = (R*(ptissue - pe) - c2*sinh(alpha))/cosh(alpha);
            pRCED = (c1*cosh(alpha.*r/R)) ./ r + (c2*sinh(alpha.*r/R)) ./ r + pe;

    %Determine the radius where we have reached pressure threshold (3 mmHg)
            pdiff = ptumor-pRCED;
    if find(pdiff < 3) == isempty(find(pdiff < 3))
        counter = length(r);
    else
        counter = min(find(pdiff < 3));
    end
    distance = counter*0.01;

    %Save the threshold distance in the matrix d
    d(Kcounter, qmcounter)=distance;
    qmcounter = qmcounter + 1;  %repeat
        end

Kcounter = Kcounter + 1;
end

%plot

[x,y] = meshgrid(0.01:0.005:0.2, logspace(-8, -5, 200));
axes('position', [0.13 0.05 0.31 0.24]);
surf(x,y,d, 'LineStyle', 'none');
axis tight; colorbar('vert')
view(0, 90);
title ('   Size of R-CED affected tissue, cm');
xlabel('Flow out of brain \mul/min');
ylabel('Interst. cond. k, cm^2/mmHg-sec');
zlabel('Radius of tissue with P < 3 mmHg, cm');
```

```matlab
%%%%%%%
%for figure 1F
%Calculate the size of the R-CED affected region for varying
%Lp (vascular hydraulic conductivity) and R-CED fluid removal rate
%using Equation 3
```

```
%intialize
clear all;


%Define the modeling space
R = 1;          %cm, total tissue radius from R-CED probe where model will be calculated
r = 0.05:0.01:R;   %cm, increment within the modeling space

%Tissue definitions
SoverV = 250;      %cm-1 Ratio of blood vessel surface area to volume of tissue
BP = 120;          %mmHg, blood pressure
ptissue = 0;       %mmHg pressure of normal tissue
pe = 9.5;          %mmHg pressure of tumor
K = 6.5e-7;        %cm2/mmHg-sec, hydraulic permeability

%Probe parameters
Rm = 0.065/2;        %cm catheter radius
rhat = Rm/R;         %no units, ratio of probe radius to total modeling space radius
A = 2*pi*Rm*0.2;     %cm2 membrane area


%Calculate Equation 3 for varying qm and Lp
Lpcounter = 1;
for Lp = logspace(-11, -7, 100)  %defines the range of Lp
   alpha = R*sqrt(Lp*SoverV/K); %dimensionless measure of interstitial and vascular resistance
to flow, see Eq. 1

   %Calculate pressure with zero flow using Eq. 3
   %We will use this in combination with the pressure at a given flow to determine the radius
where we reach the pressure threshold
      qm = 0;          %zero flux
      um = -qm*10^-3/A;  %cm/min calculate flow velocity at membrane
   %Calculate c1 and c2 before calculating the pressure in Eq. 3
              c2num = -(um*Rm*Rm/K) - R*(ptissue - pe)*(alpha*rhat*sinh(alpha*rhat) -
cosh(alpha*rhat)) / cosh(alpha);
      c2denom = alpha*rhat*cosh(alpha*rhat) - sinh(alpha*rhat) -
alpha*rhat*sinh(alpha*rhat)*sinh(alpha) / cosh(alpha) + cosh(alpha*rhat)*sinh(alpha)/cosh(alpha);
      c2 = c2num/c2denom;
      c1 = (R*(ptissue - pe) - c2*sinh(alpha))/cosh(alpha);
      ptumor = (c1*cosh(alpha.*r/R)) ./ r + (c2*sinh(alpha.*r/R)) ./ r + pe;

   %Calculate pressure with increasing flow of removing fluid using Eq. 3
   qmcounter = 1;
         for qm = 0.01:0.005:0.2; %ul/min, defines range of fluid removal
              um = -qm*10^-3/A;     %cm/min, flow velocity at membrane

              %Calculate c1 and c2 before calculating the pressure
              c2num = -(um*Rm*Rm/K) - R*(ptissue - pe)*(alpha*rhat*sinh(alpha*rhat) -
cosh(alpha*rhat)) / cosh(alpha);
      c2denom = alpha*rhat*cosh(alpha*rhat) - sinh(alpha*rhat) -
alpha*rhat*sinh(alpha*rhat)*sinh(alpha) / cosh(alpha) + cosh(alpha*rhat)*sinh(alpha)/cosh(alpha);
              c2 = c2num/c2denom;
              c1 = (R*(ptissue - pe) - c2*sinh(alpha))/cosh(alpha);
              pRCED = (c1*cosh(alpha.*r/R)) ./ r + (c2*sinh(alpha.*r/R)) ./ r + pe;
```

```
        %Determine the radius where we have reached pressure threshold (3 mmHg)
                    pdiff = ptumor-pRCED;
        if find(pdiff < 3) == isempty(find(pdiff < 3))
           counter = length(r);
        else
           counter = min(find(pdiff < 3));
        end
        distance = counter*0.01;

        %Save the threshold distance in the matrix d
        d(Lpcounter, qmcounter)=distance;
        qmcounter = qmcounter + 1;  % repeat
           end

Lpcounter = Lpcounter + 1;
end

%plot
axes('position', [0.56 0.05 0.31 0.25]);
[x,y] = meshgrid(0.01:0.005:0.2, logspace(-11, -7, 100));
surf(x,y,d, 'LineStyle', 'none');
view(0, 90); axis tight; colorbar('vert')
title ('   Size of R-CED affected tissue, cm');
xlabel('Flow out of brain \mul/min');
ylabel('Vasc. cond. Lp, cm/mmHg-sec');
zlabel('Radius of tissue with P < 3 mmHg, cm');
```

B.2.2. Code for Figure 2 and 4

```
%Grace Huynh
%2.6.07
%RCED and CED flow diagram
%using the velocity equations given by Baxter and Jain
%for Figure 2 and 4
%send the function the CED infusion velocity and the R-CED fluid removal velocity in ul/min
%For figure 4, set [x,y] = meshgrid(-0.40:0.02:0.6, -0.40:0.02:0.4) on line 90
%For figure 2, set [x,y] = meshgrid(-0.205:0.01:0.4, -0.305:0.01:0.3) on line 90


%Tissue properties
%k = hydraulic permeability, cm2/mmHg-sec
%ECSfraction = extracellular volume fraction
%qCED = flow rate in by CED
%qRCED = flow rate out by R-CED
%radiusCED = radius of CED probe
%radiusRCED = radius of RCED probe

%

%EQUATIONS

%DARCY'S LAW
%By Darcy's law for axisymmetric flow through a porous medium
%velocity (u) is proportional to the change in pressure dp/dr
%by the proportionality constant, the hydraulic permeability
%u = -k * dp/dr

%DARCY'S LAW + CONTINUITY FOR FLUID
%As shown by Morrison et al., combination of Darcy's law with the fluid continuity gives the
following eqn:
%where the hydraulic conductivity across the blood vessel wall is not included
%p = pCSF + qCED/(4*pi*ECSfraction*k*r)
%or in cartesian coordinates
%p = pCSF + qCED/(4*pi*ECSfraction*k*(x^2+y^2)

%VELOCITY DEFINITION
%so combination of these 2 equations gives
%u = qCED/(4*pi*ECSfraction*r^2)
%or in cartesian coordinates
%ux = (qCED / 4*pi*ECS fraction) * x / (x^2 + y^2)^1.5
%uy = (qCED / 4*pi*ECS fraction) * y / (x^2 + y^2)^1.5

function [] = RCEDandCEDvelocity(qCEDulmin, qRCEDulmin)

%initialize

close all;
set(0, 'defaultlineLineWidth', 3);

%Tissue definitions
k = 6.7e-7;          %hydraulic permeability, cm2/mmHg-sec
```

```
ECSfraction = 0.2;   %Extracellular space fraction
pCSF = 0;          %mmHg

%CED probe properties
qCED = qCEDulmin/(60*1000);   %ml/sec, note 1ul/min = 1.7e-5 ml/sec flow in by CED
radiusCED = 0.0025;     %cm, radius of CED probe

%R-CED probe properties
qRCED = qRCEDulmin/(60*1000);% ml/sec note 1ul/min = 1.7e-5 ml/sec flow out by R-CED
radiusRCED = 0.065/2;       %cm, radius of R-CED probe

%Define modeling space
R = 1;            %cm, total tissue radius from CED probe where model will be calculated
r = 0.03:0.01:R;     %cm, increment within the modeling space
d = 0.2;            %cm, distance between RCED and CED probe

%Calculate pressure distribution
%Assume the CED and R-CED pressure distribution is additive
pCED = qCED./(4*pi*ECSfraction*k.*r);          %pressure distribution due to CED probe
pRCED = qRCED./(4*pi*ECSfraction*k.*(abs(r-d)));  %pressure distribution due to R-CED probe
p = pCSF + pCED + pRCED;                %Add CED and R-CED effect to background
(pCSF)
axes('position', [0.07 0.57 0.4 0.4]); axis tight; plot(r,p,'k', r,pCED,'m', r,pRCED,'c')        %plot
legend('R-CED + CED', 'CED alone', 'R-CED alone');
title(['CED ', num2str(qCEDulmin), '\mul/min, R-CED ', num2str(qRCEDulmin), '\mul/min']);
ylabel('Pressure, mmHg'); xlabel('Distance, cm');

%Calculate velocity distribution
%Assume the CED and R-CED velocity distribution is additive
uCED = -k*gradient(pCED);    %velocity due to CED
uRCED = -k*gradient(pRCED);  %velocity due to R-CED
u = uCED + uRCED;          %add to determine combined effect
axes('position', [0.07 0.07 0.4 0.4]); axis tight; plot(r,u,'k', r,uCED,'m', r,uRCED,'c')
legend('R-CED + CED', 'CED alone', 'R-CED alone');
title('Velocity distribution'); xlabel('Distance, cm'); ylabel('Velocity, cm/s');


%Calculate pressure and velocity distribution in cartesian coordinates
%This enables us to draw a 2D graph

%Calculate pressure distribution
[x,y] = meshgrid(-0.205:0.01:0.4, -0.305:0.01:0.3);          %define the modeling space
pCED2D = qCED./(4*pi*ECSfraction*k.*(sqrt(x.^2+y.^2)));       %pressure distribution due to
CED
pRCED2D = qRCED./(4*pi*ECSfraction*k.*(sqrt((x-d).^2+y.^2)));   %pressure distributio due to R-
CED
p2D = pCED2D + pRCED2D + pCSF;                    %Add CED and R-CED effect to
background (pCSF)
axes('position', [0.55 0.57 0.4 0.4]);
contourlines = linspace(-100,200,25);
contour(x,y,p2D,contourlines);
title('Pressure map, mmHg'); xlabel('Distance, cm'); ylabel('Distance, cm');

%Calculate velocity distribution, separate x and y velocities
%x velocity
uCED2Dx = (x .* qCED ./(4*pi*ECSfraction)) ./ (x.^2 + y.^2).^1.5;
```

```
uRCED2Dx = ((x-d) .* qRCED ./(4*pi*ECSfraction)) ./ ((x-d).^2 + y.^2).^1.5;
u2Dx = uCED2Dx + uRCED2Dx;
%y velocity
uCED2Dy = (y .* qCED ./(4*pi*ECSfraction)) ./ (x.^2 + y.^2).^1.5;
uRCED2Dy = (y .* qRCED ./(4*pi*ECSfraction)) ./ ((x-d).^2 + y.^2).^1.5;
u2Dy = uCED2Dy + uRCED2Dy;
%Total velocity (combine x and y direction
u2D = sqrt(u2Dx.^2 + u2Dy.^2);

%get rid of the very large values caused by dividing by nearly 0
[maxx,maxy] = find(abs(u2Dx) > 0.3);
u2Dx(maxx, maxy) = 0;
clear maxx maxy;
[maxx,maxy] = find(abs(u2Dy) > 0.3);
u2Dy(maxx,maxy) = 0;


%plot the velocity map with contours and arrows
axes('position', [0.55 0.07 0.4 0.4]);
set(0, 'defaultlineLineWidth', 1)
contourlines = logspace(-5, -3, 15);
contour(x,y, u2D, contourlines); hold on;
quiver(x, y, u2Dx, u2Dy);
title('Velocity map, cm/s'); xlabel('Distance, cm'); ylabel('Distance, cm')

%Pressure surface map
%figure; surf(x,y,p2D, 'LineStyle', 'none')
%view(0, 90); caxis([-100 100]); colorbar('vert')
%title('Pressure'); xlabel('Distance, cm'); ylabel('Distance, cm'); zlabel('Pressure, mmHg')



if qCEDulmin > 0 & qRCEDulmin > 0

%plot the velocity map with contours and arrows
figure;
axes('position', [0.07 0.12 0.4 0.8]);
set(0, 'defaultlineLineWidth', 1)
contourlines = logspace(-5, -3, 15);
contour(x,y, u2D, contourlines); hold on;
quiver(x, y, u2Dx, u2Dy);
title('Velocity map, cm/s'); xlabel('Distance, cm'); ylabel('Distance, cm')

%%%
%Display the wavefront in the case of two positive pressure infusions
%define the concentration with time
%march along the wavefront with each timestep to see how the equivolumetric
%line moves in each direction

%start with the wave profile at time 0, which is the radius of the probe
%Define the probe radius circle of points by parametric method
t = 0:pi/15:2*pi;
position = [0.005*cos(t); 0.005*sin(t); 0.005*cos(t)+d; 0.005*sin(t)];
%in this position matrix, the rows represent as follows:
%1st row: x values CED infusion
%2nd row, y values CED infusion
```

%3rd row: x values probe 2 (RCED) infusion
%4th row, y values, probe 2 infusion

%plot the initial probe radius
axes('position', [0.55 0.12 0.4 0.8]); plot(position(1,:), position(2,:));
hold on; plot(position(3,:), position(4,:), 'm'); %2nd probe in pink
legend('CED, probe 1', 'CED, probe 2'); title('Wavefront from dual probe CED probes, every 5 min'); xlabel('Distance, cm'); ylabel('Distance, cm');

%Solve for the velocity in cartesian coordinates
%We have already solved the velocity map in 2D for equally spaced points
%The velocity matrix will hold the information for the velocity at the wavefront - these coordinates are described by the position matrix
%The velocity at a particlar point is the sum of the velocity caused by CED (probe 1) and the velocity caused by R-CED (probe 2)
velocity(1,:) = (position(1,:) .* qCED ./(4*pi*ECSfraction)) ./ (position(1,:).^2 + position(2,:).^2).^1.5 + ((position(1,:)-d) .* qRCED ./(4*pi*ECSfraction)) ./ ((position(1,:)-d).^2 + position(2,:).^2).^1.5;
velocity(2,:) = (position(2,:) .* qCED ./(4*pi*ECSfraction)) ./ (position(1,:).^2 + position(2,:).^2).^1.5 + (position(2,:) .* qRCED ./(4*pi*ECSfraction)) ./ ((position(1,:)-d).^2 + position(2,:).^2).^1.5;
velocity(3,:) = (position(3,:) .* qCED ./(4*pi*ECSfraction)) ./ (position(3,:).^2 + position(4,:).^2).^1.5 + ((position(3,:)-d) .* qRCED ./(4*pi*ECSfraction)) ./ ((position(3,:)-d).^2 + position(4,:).^2).^1.5;
velocity(4,:) = (position(4,:) .* qCED ./(4*pi*ECSfraction)) ./ (position(3,:).^2 + position(4,:).^2).^1.5 + (position(4,:) .* qRCED ./(4*pi*ECSfraction)) ./ ((position(3,:)-d).^2 + position(4,:).^2).^1.5;

%Now that we have the velocity at the wavefront, we can move each point in the wavefront forwards with time
%Then recalculate the velocity, and continue to move the wavefront forwards with each timestep.
timestep = 0.05;
for time = timestep:timestep:3000; %count to 3000s = 50 min

    %move the wavefront forwards
    position = position + velocity * timestep;

    %calculate the velocity at the wavefront
    velocity(1,:) = (position(1,:) .* qCED ./(4*pi*ECSfraction)) ./ (position(1,:).^2 + position(2,:).^2).^1.5 + ((position(1,:)-d) .* qRCED ./(4*pi*ECSfraction)) ./ ((position(1,:)-d).^2 + position(2,:).^2).^1.5;
    velocity(2,:) = (position(2,:) .* qCED ./(4*pi*ECSfraction)) ./ (position(1,:).^2 + position(2,:).^2).^1.5 + (position(2,:) .* qRCED ./(4*pi*ECSfraction)) ./ ((position(1,:)-d).^2 + position(2,:).^2).^1.5;
    velocity(3,:) = (position(3,:) .* qCED ./(4*pi*ECSfraction)) ./ (position(3,:).^2 + position(4,:).^2).^1.5 + ((position(3,:)-d) .* qRCED ./(4*pi*ECSfraction)) ./ ((position(3,:)-d).^2 + position(4,:).^2).^1.5;
    velocity(4,:) = (position(4,:) .* qCED ./(4*pi*ECSfraction)) ./ (position(3,:).^2 + position(4,:).^2).^1.5 + (position(4,:) .* qRCED ./(4*pi*ECSfraction)) ./ ((position(3,:)-d).^2 + position(4,:).^2).^1.5;

    %plot the wavefront every 5 minutes (300 seconds)
    if rem(time,300) == 0
        hold on;
        plot(position(1,:), position(2,:));
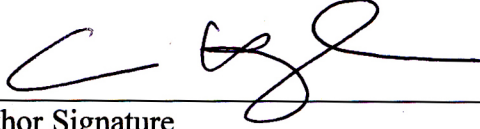   plot(position(3,:), position(4,:), 'm');
    end
  end
end

Publishing Agreement

It is the policy of the University to encourage the distribution of all theses and dissertations. Copies of all UCSF theses and dissertations will be routed to the library via the Graduate Division. The library will make all theses and dissertations accessible to the public and will preserve these to the best of their abilities, in perpetuity.

I hereby grant permission to the Graduate Division of the University of California, San Francisco to release copies of my thesis or dissertation to the Campus Library to provide access and preservation, in whole or in part, in perpetuity.

_____   3.12.07
Author Signature   Date